Thulium doped tellurium oxide amplifiers and lasers integrated on silicon and silicon nitride photonic platforms

THULIUM DOPED TELLURIUM OXIDE AMPLIFIERS AND LASERS INTEGRATED ON SILICON AND SILICON NITRIDE PHOTONIC PLATFORMS

By KHADIJEH MIARABBAS KIANI, M. Eng

A thesis submitted to the School of Graduate Studies in partial fulfillment of the requirements for the degree Ph. D.

McMaster University February 28, 2022

McMaster University

Ph.D. (2022)

Hamilton, Ontario (Department of Engineering Physics)

TITLE: Thulium doped tellurium oxide amplifiers and lasers integrated on silicon and silicon nitride photonic platforms

AUTHOR: Khadijeh Miarabbas Kiani (McMaster University)

SUPERVISORS: Dr. Jonathan D. B. Bradley and Dr. Andrew P. Knights

NUMBER OF PAGES: xxv, 200

Abstract

Silicon photonics (SiP) has evolved into a mature platform for cost-effective low power compact integrated photonic microsystems for many applications. There is a looming capacity crunch for telecommunications infrastructure to overcome the data-hungry future, driven by streaming and the exponential increase in data traffic from consumer-driven products. To increase data capacity, researchers are now looking at the wavelength window of the thulium-doped fiber amplifier (TDFA), centered near 2 μm as an attractive new transmission window for optical communications, motivated by the demonstrations of low-loss, low nonlinearity, and high bandwidth transmission. Large-scale implementation of SiP telecommunication infrastructure will require light sources (lasers) and amplifiers to generate signals and boost transmitted and/or received signals, respectively. Silicon (Si) and silicon nitride (Si_3N_4) have become the leading photonic integrated circuit (PIC) material platforms, due to their low-cost and wafer-scale production of high-performance circuits. Silicon does however have a number of limitations as a photonic material, including that it is not an ideal light-emitting/amplifying material. This proposed research pertains to the fabrication of on-chip silicon and silicon nitride lasers and amplifiers to be used in a newly accessible optical communications window of the TDFA band, which is a significant step towards compact PICs for the telecommunication networks. Tellurium oxide (TeO_2) is an interesting host material due to its large linear and non-linear refractive indices, low material losses and large rare-earth dopant solubility showing good performance for compact low-loss waveguides and on-chip light sources and amplifiers.

Chapter 1 provides an overview of silicon photonics in the context of particularly rare earth lasers and amplifiers, operating at extended wavelengths enabled by the Thulium doped fiber amplifier. Chapter 2 presents a theoretical performance of waveguides and microresonators as the efficient structure for laser and amplifiers applications designed for optimized use in Erbium and Thulium doped fiber amplifier wavelength bands. Then spectroscopic study thulium (Tm^{3+}) has been studied as the rare earth element for Thulium doped fiber amplifier wavelength bands. Chapter 3 presents an experimental study of TeO_2:Tm^{3+} coated Si_3N_4 waveguide amplifiers with internal net gains of up to 15 dB total in a 5-cm long spiral waveguide. Chapter 4 provides a study of TeO_2:Tm^{3+}-coated Si_3N_4 waveguide lasers with up to 16 mW double-sided on-chip output power. Chapter 5 presents an experimental study of low loss and high-quality factor silicon microring resonators coated with TeO_2 for active, passive, and nonlinear applications. Chapter 6 represents the first demonstration of an integrated rare-earth silicon laser, with high performance, including single-mode emission, a lasing threshold of 4 mW, and bidirectional on-chip output powers of around 1 mW. Further results with a different design are presented showing lasers with more than 2 mW of double-sided on-chip output power, threshold pump powers of < 1 mW and lasing at wavelengths over a range of > 100 nm. Importantly, a simple, low-cost design was used which is compatible with silicon photonics foundry processes and enables wafer scale integration of such lasers in SiP PICs using robust materials. Chapter 7 summarizes the thesis and provides paths for future work.

To my parents, my brothers, and my sisters

Acknowledgments

I would first like to thank my supervisors, Dr. Jonathan D. B. Bradley, and Dr. Andrew P. Knights, for their support and encouragement in my academic research. I would also like to thank Dr. Nabil Bassim for reviewing my thesis and serving on my Ph.D. defense committee. A big thanks to Dr. James Wilkinson as an external examiner for reading the work and for his comments.

At McMaster University, I had the honor of taking courses with outstanding professors who deserve my sincere appreciation. I would like to thank Shahram Tavakoli, Zhilin Peng. David Haugan and Jeremy Miller for their support.

Finally, from bottom of my heart, I would like to thank my dear parents, sisters, and brothers for all their love, sacrifice, guidance, and encouragement. My family's love, kindness, wisdom, and support were the brightest light of this journey.

Table of Contents

List of Figures

List of Tables

List of Acronyms

AFM	Atomic Force Microscopy
BOX	Buried-Oxide
BW	BandWidth
CEDT	Center for Emerging Device Technologies
CMOS	Complementary Metal-Oxide-Semiconductor
CR	Cross Relaxation
CVD	Chemical Vapor Deposition
EDFA	Erbium Doped Fiber Amplifier
ER	Extinction Ratio
ESA	Excited State Absorption
ETU	Energy Transfer Upconversion
EYDFA	Erbium-Ytterbium Doped Fiber Amplifier
FDTD	Finite-Difference Time-Domain
FIB	Focused-Ion-Beam
FSR	Free Spectral Range
FWHM	Full-Width at Half-Maximum
FWM	Four Wave Mixing
GSA	Ground State Absorption
ICP	Inductively Coupled Plasma
IL	Insertion Loss

$LiNbO_3$	Lithium Niobate
LPCVD	Low Pressure Chemical Vapor Deposition
MIR	Mid-Infrared
MPW	Multi-Project Wafer
MRR	Micro-Ring Resonator
OSA	Optical Spectrum Analyzer
PD	Photodiode
PIC	Photonic Integrated Circuit
PVD	Physical Vapor Deposition
RBS	Rutherford Backscattering Spectrometry
RF	Radio Frequency
SEM	Scanning-Electron Microscopy
SiEPIC	Silicon Electronic Photonic Integrated Circuits
SiO_2	Silicon Dioxide
SM	Single Mode
SOI	Silicon-On-Insulator
TDFA	Thulium Doped Fiber Amplifier
TE	Transverse Electric
TEC	Thermo-Electric Cooler
TIR	Total Internal Reflection
TM	Transverse Magnetic
TPA	Two-Photon Absorption

WDM	Wavelength-Division Multiplexing

Declaration of Authorship

I, Khadijeh Miarabbas Kiani, declare that this thesis titled, “Thulium doped tellurium oxide amplifiers and lasers integrated on silicon and silicon nitride photonic circuit platforms”, and the work presented in it was written and was led by myself. I confirm that:

Collaboration with co-authors included:

- Chapter 3, a paper published in *Optics Letters*: K.M.K. developed and optimized the low-loss tellurium oxide and thulium-doped tellurium oxide fabrication processes. K.M.K. performed the experimental characterization and analysis. K.M.K. gathered and analyzed the data. K.M.K. improved the results with optimization of fabrication and characterization process. Waveguide design and layouts were done with H.C.F.’s contribution. K.M.K. wrote the manuscript with editing from A.P.K. and J.D.B.B.
- Chapter 4, a paper published in *Optical Materials Express*: K.M.K. developed and optimized the low-loss tellurium oxide and thulium-doped tellurium oxide fabrication processes. K.M.K. performed the experimental characterization and analysis. K.M.K. gathered and analyzed the data. Waveguide design and layouts were done with H.C.F.’s contribution. K.M.K. wrote the manuscript with editing from A.P.K. and J.D.B.B.
- Chapter 5, a paper published in *Applied Sciences*: K.M.K. designed the device. K.M.K. and D.B.B. laid out the silicon chips. K.M.K. developed and optimized the low-loss tellurium oxide films on the silicon chips. K.M.K. performed the experimental

characterization and analysis. K.M.K. wrote the manuscript. A.P.K. and J.D.B.B. edited the text.

- Chapter 6, a paper published in *Lasers and Photonics Reviews*: K.M.K. designed the device. H.C.F., C.M.N. and D.B.B. laid out the silicon chips. K.M.K developed and optimized the low-loss tellurium oxide and thulium-doped tellurium oxide fabrication processes deposited the tellurium oxide and thulium doped tellurium oxide films on silicon chips and performed the experimental characterization and analysis. K.M.K. gathered and analyzed the data. K.M.K. and J.D.B.B. wrote the manuscript, with input from A.P.K. K.M.K. optimized the designs, experiments and characterization processes and improved the results.

Chapter 1

Introduction

1.1 The TDFA Window

There is a looming capacity crunch for telecommunications infrastructure to overcome a data-hungry future. This is a result of the exponential increase in data traffic demanded by consumer-driven products, such as smartphones; and platforms such as Netflix, and Facebook. As a consequence, this demand for increased bandwidth is presenting a significant technological challenge.

Encoded data is transmitted via optical signals from the data center to consumers through low-loss optical fibers across many kilometers of distance. Photonics and electronic engineers are doing research to develop techniques to deal with the looming “capacity crunch” as data transmission rates grow into the ‘Zettabyte Era’ [1]. To address earlier growing bandwidth demands in the 1990’s, the industry turned to higher wavelength windows. Using a similar approach, telecommunication infrastructure is now being developed around the wavelength of 2 μm, an attractive transmission window for optical communications, due to the demonstrations of low-loss, low nonlinearity high bandwidth transmission, and high-capacity optical communications with low latency that minimize impairments. For instance, hollow-core bandgap fibres or antiresonant hollow-core fibers, supporting optical signals at 1.9–2.1 μm wavelengths aim to reduce nonlinearities while improving latency with low-optical loss [2-4], experimentally measured as 2 dB/km for 2 μm in a 4-km-long hollow-core photonic bandgap fibre [3].

Light sources (lasers) and amplifiers are required to generate signals and to compensate inherent signal loss due to absorption and scattering and boost transmitted and /or received signals, especially for ultra-long-haul applications. Thulium-doped fiber amplifiers (TDFAs) are conveniently centered near 1900 nm [5]. The TDFA has a demonstrated gain bandwidth of over 240 nm (approximately three times larger than the erbium-doped fiber amplifier (EDFA)) [5].

In addition to telecommunication, this extended wavelength range is suitable for other applications. The wavelength range around 2 μm is “eye safe”. As such, the TDFA window offers advantages for free space applications which include light detection and ranging (LIDAR) [6], medical diagnostics and therapeutics [6], and environmental sensing [7].

1.2 Integrated Silicon and Silicon Nitride Photonics

Silicon photonics (SiP) is revolutionizing telecommunications by delivering cost-effective, scalable solutions for high bandwidth optical communications, with low power consumption and integration with low power consumption and integration with electronics [8,9] using mature Complementary-Metal-Oxide-Semiconductor (CMOS) manufacturing technology. Silicon photonics foundries now provide standard process design kits including many of the building blocks for high-performance optical circuits, containing passive devices such as optical waveguides, (de) multiplexers and filters as well as active optoelectronic devices such as high-speed modulators, photodetectors, and switches [10–12]. Silicon-On-Insulator (SOI) wafers composed of thin layers of silicon with typically 220 nm - 400 nm thickness on a buried-oxide (BOX) layer [13], confine light through the large refractive index contrast between silicon and silicon-dioxide (SiO_2). Both are transparent at wavelengths between 1100 – 2500 nm [14]. For applications requiring a small form factor, silicon has emerged as an ideal platform for compact, low-loss, and high-speed 2-μm integrated photonic devices and systems [15].

Integrated optics implies the integration of various optical devices, on the same platform, which in the case of silicon photonics, can be repeated multiple times across the SOI wafer [16]. Significant progress has been made in the five decades since the concept of integrated optics was introduced [17]. Silicon was suggested as an integrated photonics platform in the mid 1980's and silicon photonics has since received significant attention [18] and been applied to an array of applications such as communications, biological sensors, quantum computing, and LIDAR [19-23].

Most of the passive monolithic components, including splitters, couplers, and resonators as well as active devices including detectors and modulators have already been demonstrated in silicon photonics [15,24]. However, on-chip optical amplifiers and light sources as essential active on-chip functionalities, are still a considerable challenge for foundry offerings due to the required provision for flexible high-yield.

The need for additional functionalities in silicon-based integrated optics has led to the exploration of other silicon-compatible materials. Silicon nitride (Si_3N_4) waveguides have been of interest since the late 1970s with several prominent results reported, including ultralow loss planar waveguides as a platform on a silicon substrate, and as a material for use at wavelengths where silicon is absorbing [25]. Its low propagation loss ($\leq$ 0.1 dB/cm) and wide transparency window (~400 nm to 2.35 μm), relatively high refractive index, nanoscale feature resolution, and mature fabrication methods have made it a versatile complementary silicon-compatible platform for a wide variety of applications [25–28].

Si_3N_4 is a silicon-foundry-compatible material widely applied in passive devices such as filters, multiplexers, and switching and routing components for communications systems [25,29]. Recently, it has been developed as a high-performance medium for nonlinear optical devices [27,28,30], monolithic and hybrid on-chip lasers and amplifiers [26,31–33], and sensing and spectroscopic circuits [34,35]. Additionally, various active devices have evolved on silicon nitride platforms based on hybrid integration methods, including bonding of III-V semiconductor materials [36] and monolithic deposition of rare-earth-doped aluminum oxide thin films [33].

The exploration of both silicon and silicon nitride integrated optical circuits is made in this work.

1.3 Laser Integration in Silicon and Silicon Nitride Photonics

Townes, in the 1950s, performed pioneering work that resulted in the first demonstration of a MASER (“microwave amplification by stimulated emission of radiation”) [37]. Several years later, in 1960, Maiman demonstrated the first LASER (“light amplification by stimulated emission of radiation”), in the visible wavelength region, based on a flashlamp-pumped ruby ($Al_2O_3:Cr^{3+}$) crystal [38]. Since the demonstration of the first laser, researchers have explored many types of lasers including solid state lasers based on many different active species in various host materials [39].

The integration of lasers in silicon-based photonic systems presents one of the greatest challenges. Silicon is an indirect bandgap semiconductor, thus the probability for radiative recombination is low in silicon. Furthermore, due to silicon’s 1.1 eV bandgap, light emission is also limited to wavelengths < 1.1 µm. Various methods have been explored including a silicon Raman laser [40], directly grown or heterogeneously bonded III-V semiconductors [41], germanium-tin alloys [42], and silicon-organic hybrid devices [43]. Many outstanding results have been reported, particularly for electrically-pumped III-V heterogeneously- and hybrid-integrated devices, even leading to commercial devices and systems [44,45]. III-V semiconductor-based gain materials, deliver high gain over short distances in term of large stimulated emission cross-sections of the excited carriers, which by considering heterogeneous integration techniques, make them appropriate for on-chip devices. They can be electrically pumped, allowing for direct electrical excitation and fast modulation of gain and lasing. However, they suffer from drawbacks such as less efficient stimulated-emission cross sections, short carrier lifetimes, temporal, and spatial gain patterning effects, and large nonlinear optical response at extended near- and mid-infrared wavelengths [39]. Furthermore, the heterogeneous integration method is relatively expensive and brings additional complexity to the fabrication processes [39].

1.4 Rare Earth Optical Amplifiers and Lasers

The first rare-earth-doped laser was demonstrated using neodymium-doped glass in 1961 [46]. Soon after, the first rare-earth-doped fiber amplifier was fabricated in 1964 with the gain observed in a 1-m long neodymium-doped fiber [47]. Since then, the fiber amplifier has become the heart of optical communication, enabling efficient in-line amplification without electrical repeaters, but miniaturization and integration of optical devices are anticipated to change our daily life in the decades to come [39]. Compared to fiber, integrated waveguide amplifiers and lasers are compact, low cost, and use straightforward fabrication methods, enabling wafer-scale processing and integration with other photonic devices for high-performance microsystems [32,48]. Therefore, one of the requirements of the current amplifier and laser development is the demand for miniaturization, on-chip integration, and mass fabrication. Consequently, the performance and capabilities of rare-earth-doped dielectric waveguide amplifiers and lasers have steadily improved over the past few decades [39].

Rare-earth-doped optical gain materials are low-cost and can be deposited monolithically on silicon photonics platforms allowing wafer-scale fabrication. Rare-earth-doped optical gain materials enable straightforward versatile design, with high thermal stability, and offer broadband optical gain and lasing in near-infrared bands [39]. Importantly, these devices can generate less heat on the microchip, and operate with better stability and higher amplification bit rate or narrower intrinsic laser linewidth than their III-V semiconductor counterparts [39]. Lastly, one fixed-wavelength off-chip pump diode source, in a package with the PIC and with one pump-chip interface, can effectively power many rare-earth-based amplifiers or lasers with versatile design and operation on the chip, allowing for a compact form factor [39].

The development of on-chip rare-earth amplifiers and lasers integrated directly with silicon remains challenging, because the stimulated-emission cross-section values of rare-earth-doped gain materials are usually four to five orders of magnitude smaller than III-V semiconductor-based gain materials [39]. This leads to significantly lower gain per unit length and makes it challenging to overcome the loss to achieve net amplification. Even with higher mode overlap with the active layer (in comparison with III-V semiconductors-based gain materials), this disadvantage cannot be compensated, resulting in a less efficient gain material and requiring larger interaction lengths and specialized low loss silicon waveguide structures not available in foundries for comparable total gain. Quenching and up-conversion effects of active ions in rare-earth gain materials at higher concentration levels are other limitations for rare earth gain materials [39]. Rare-earth-doped materials have relatively long excited-state lifetimes (0.1–10 ms) and low refractive index change which are useful for thermally and spatially stable gain [26,49,50].

Rare-earth-doped amplifiers and lasers have been demonstrated in fibers, bulk glasses and crystals, integrated channel waveguides, and recently on Si and Si_3N_4 platforms [39,51]. Several rare earth ions have been used in amplifiers and lasers including Tm^{3+}, Ho^{3+}, Er^{3+}, Yb^{3+}, Pr^{3+}, and Nd^{3+} with different emission wavelengths ranging from 0.48 to 2.9 µm.

In recent years, Tm^{3+} doped materials have been of significant interest, particularly because of thulium's broad wavelength emission band from 1600 to over 2000 nm that enables wavelength tunability and design flexibility in the 'eye safe' wavelength domain [52–54]. It can also be used for amplification and emission in other wavelength bands, including the 1460-1520 nm communication window [55] and in the 2200-2460 nm region [54]. The laser emission of Thulium around 2.0 µm results from the $_3F^4$ to $_3H^6$ transition. In 1965, the first Tm:YAG flashlamp-pumped laser at 2 µm, which operated at 77K, was demonstrated [56]. In 1975, a Cr,Tm:YAG laser operating at room temperature was demonstrated by Caird et al [57]. Until now thulium lasers were demonstrated in various host materials and there are some available commercial thulium-based laser systems (Active fiber system (AFS); IPG Photonics Corp; LISA laser products OHG) [58,59]. For example, Tm:YAG lasers emitting at 2.0 µm wavelength are commercially available at LIZA laser products OHG with 120 W output power [58,59].

With the broadest gain spectrum of all rare-earth doped amplifiers and lasers, high peak gain, and low noise figure performance, thulium-doped amplifiers and lasers are of significant interest [5,60,61]. Thus, on-chip Tm-doped waveguides are an interesting option for high-performance amplifiers and lasers on silicon photonics platforms. As an example, integrated thulium-doped channel waveguide lasers on tungstate were reported with high output powers (1.6 W) and slope efficiencies (80%) [62, 63]. A thulium-doped microcavity laser was reported with sub-milliwatt threshold power and multi-mode operation using $Al_2O_3:Tm^{3+}$ thin film as a gain medium [64]. However, so far work on thulium-doped high-power amplifiers and lasers on a CMOS-compatible platform has been absent.

1.5 Rare-Earth Doped Tellurite Glasses for Optical Applications

This thesis focuses on amorphous tellurite glass, or TeO_2, as the host material for waveguide amplifiers and lasers. Tellurite glass was introduced as a new candidate for fiber devices by J. S. Wang [65] in 1994. TeO_2 has a wide transition region of 0.35 to 5 µm with good glass stability and corrosion resistance [65]. Its low maximum phonon energy of (~700–800 cm^{-1}), high quantum efficiency, high refractive index, and high nonlinear refractive index measured to be 1.3×10^{-18} m^2/W at 1900 nm [66] make it a suitable candidate for nonlinear and laser applications. The linear refractive index of TeO_2 is 2.08 at a 1550 nm wavelength [67], which is lower than that for silicon (3.47 at 1550 nm) [68], but larger than for silicon nitride (1.99 at 1550 nm) [69]. This allows for highly confined TeO_2 cladded silicon and silicon nitride straight and curved waveguides.

Tellurite is an excellent host material for rare earth dopants in term of its wide emission bandwidths, high rare earth solubility, and large emission cross-sections [70] in comparison with other glass materials. Its low two photon absorption (TPA) of 3×10^{-12} m/W [71], high

Raman gain coefficient of 1.7×10^{-10} m/W [71], and high acousto-optic figure of merit of 24×10^{-18} s^3/g) [72], make TeO_2 a great candidate for a variety of integrated photonics applications. Its low temperature and straightforward wafer-scale deposition via sputtering also makes TeO_2 a versatile and inexpensive material for hybrid integration on silicon and silicon nitride platforms [73]. Tellurite glass has been broadly studied in fiber-optic platforms [70,71,74], but it is still relatively immature as an integrated optical material. Integrated tellurite glass waveguides, amplifiers and lasers have been fabricated in bulk glass as well as thin films [73-75].

Recently there have been several promising demonstrations of thulium-doped tellurite amplifiers and lasers in fiber, bulk glass, and on-chip platforms. Two-color CW lasing simultaneously near 1.9 μm and 2.3 μm and ultrabroadband amplification in a Tm^{3+}-doped tellurite fiber was demonstrated experimentally. It presents a high-quality tellurite fiber can be an attractive option for developing lasers in the 2.3 μm window for applications in eye-safe laser radars, gas sensing, remote sensing, breath analysis, and trace gas detection [76]. A thulium-doped tellurite fiber amplifier was demonstrated with a net gain of almost 20 dB in the S-band using dual pump and bidirectional pumping schemes [55]. Thulium-doped TZNG bulk glass laser pumped at 1211 nm was demonstrated with a measured slope efficiency of 22.4% with the tuning range of 115 nm ranging from 1850 nm to 2040 nm [77]. Thulium-doped tellurite glass microsphere lasers were observed with emission wavelengths near 1975 nm [78]. A Tm^{3+}–Ho^{3+} co-doped tellurite glass microsphere laser was also demonstrated in the 1.47 μm wavelength region using an 802 nm laser diode as a pump source [79]. Despite the wide range of research on amplifiers and lasers, $TeO_2:Tm^{3+}$

amplifiers and lasers have not been yet explored on silicon and silicon nitride PIC platforms that are promising for TDFA band applications in these platforms.

1.6 Thesis Objectives

This thesis describes the design, fabrication, and characterization of thulium-doped tellurite glass waveguide amplifiers and lasers on silicon platforms. It describes gain and lasing in thulium hybrid structures directly on silicon as well as high gain thulium-doped waveguide amplifiers and lasers on a silicon nitride platform for applications in the emerging TDFA-band. The investigated photonic structures include straight waveguides, curved waveguides (including S-bends, paperclips, and spirals), microrings, and microdisks, and devices for active and passive applications. An optimized fabrication process to deposit low-loss thulium-doped tellurium oxide thin films for silicon and silicon nitride amplifiers and lasers is demonstrated using radio frequency reactive co-sputtering deposition, as well as the design of photonic chips fabricated at external foundries. The thesis also describes a probe station developed to characterize optical amplifiers and lasers on silicon and silicon nitride. The work aims to make a significant step toward the realization of novel, high quality, low cost, and high performance TDFA-band integrated lasers and amplifiers in silicon and silicon nitride for use in future short-haul and long-haul telecommunications infrastructure to accommodate ever-growing data bandwidth requirements.

1.7 Statement of Thesis Work

This thesis consists of seven chapters. In Chapter 2, the background and theory of the devices presented in this thesis are discussed to investigate the principles of light propagation and confinement in optical waveguides and resonators. Then, the science behind thulium amplifiers and lasers is given based on the spectroscopy of rare-earth ions. Chapter 3 discusses the characterization of $TeO_2:Tm^{3+}$ waveguides amplifiers on a silicon nitride platform followed by the optimized high gain amplifier fabrication and characterization. Significant progress in developing cost-effective, higher gain, more compact, and more efficient integrated $TeO_2:Tm^{3+}$ waveguide amplifiers with lower background loss on a silicon nitride platform is presented in this chapter. In chapter 4 the thesis shows the design, fabrication, characterization, and optimization of compact, monolithically integrated thulium-doped tellurium oxide ($TeO_2:Tm^{3+}$) microring lasers on a low-loss silicon nitride platform. More studies are presented in this chapter on $TeO_2:Tm^{3+}$-Si_3N_4 microring lasers with different thulium concentrations. Chapter 5 presents high *Q* factor TeO_2 coated silicon microring resonators. The simulated and experimentally measured optical properties of the TeO_2 coated, SiO_2 coated and uncoated silicon microring resonators are discussed. TeO_2-coatings on devices as received from the foundry were found to have higher *Q* factor corresponding to lower waveguide propagation losses in comparison with SiO_2 cladded and uncladded microring resonators. Chapter 6 presents the first demonstration of a thulium laser on a silicon-on-insulator platform. The design, fabrication, and characterization of optical gain and lasing in an on-chip, ultra-compact hybrid $TeO_2:Tm^{3+}$-silicon microdisk resonator are demonstrated in this chapter. The straightforward design and compatibility with the fabrication steps and device dimensions available in all-silicon photonics foundries and low-temperature single-step thin film deposition process are presented in this chapter in detail to fabricate the hybrid silicon microdisk laser. The work demonstrates a low threshold, single-mode, efficient, and highly compact hybrid $TeO_2:Tm^{3+}$ silicon microdisk laser by optimizing the design, background loss, active material concentration, and thickness, and pump wavelength in the TDFA band. Furthermore, sub-milliwatt threshold hybrid silicon lasers with lasing over a wide range of wavelengths of > 100 nm in the TDFA band are described in detail. Chapter 7 summarizes the major milestones achieved in this thesis and provides a guide on potential future research directions related to this work. Key achievements are:

- Low loss thulium-doped tellurium oxide ($TeO_2:Tm^{3+}$) thin-film have been developed to fabricate on-chip lasers and amplifiers for silicon (Si) and silicon nitride (Si_3N_4) based photonic platforms.
- An efficient, high gain, low loss, and compact $TeO_2:Tm^{3+}$ amplifier is presented on a silicon nitride waveguide in TDFA band with 15 dB internal net gain at 1870 nm.
- An optimized, monolithic $TeO_2:Tm^{3+}$ laser with excellent performance, including single-mode and multimode emissions and bidirectional on-chip output power up to 16 mW was designed, fabricated, and characterized on silicon nitride.
- Low-loss hybrid TeO_2-Si microring resonators were investigated with internal Q factors of up to 1.5×10^6, corresponding to a propagation loss of 0.42 dB/cm at wavelengths around 1550 nm.
- Lasing from a silicon microdisk is presented and is the first demonstration of the integration of a rare-earth laser directly on silicon using robust materials and simple low-temperature processing.

- The hybrid thulium-silicon laser design was refined to show low-threshold (sub-milliwatt pump power) lasing, up to 2.6 mW total on-chip output power and lasing at wavelengths spanning over 100 nm (1825–1937 nm) in the emerging TDFA band of interest.
- Gain was demonstrated in a 3-mm-long $TeO_2:Tm^{3+}$-silicon hybrid waveguide for a launched pump power of 32.4 mW showing up to 1.8 dB signal enhancement corresponding to 0.4 dB internal net gain.
- The design and fabrication approaches presented in this thesis open significant new possibilities for integrated rare-earth lasers and amplifiers on silicon and silicon nitride platforms.

1.8 Publications

The following is a list of journal articles by the author that have contributed to the results presented in this thesis:

- **K. Miarabbas Kiani**, H. C. Frankis, C. M. Naraine, D. B. Bonneville, A. P. Knights, and J. D. B. Bradley, "Lasing in a hybrid rare-earth silicon microdisk," *Laser Photon. Rev.* **16**, 210034 (2022).

- **K. Miarabbas Kiani**, D. B. Bonneville, A. P. Knights, and J. D. B. Bradley, "High-*Q* TeO_2–Si hybrid microring resonators," *Appl. Sci.* **12**, 1363 (2022).

- **K. Miarabbas Kiani**, H. C. Frankis, R. Mateman, A. Leinse, A. P. Knights, and J. D. B. Bradley, "Thulium-doped tellurium oxide microring lasers integrated on a low-loss silicon nitride platform," *Opt. Mater. Express* (Spotlight in Optica) **11**, 3656–3665 (2021).

- **K. Miarabbas Kiani**, H. C. Frankis, H. M. Mbonde, R. Mateman, A. Leinse, A. P. Knights, and J. D. B. Bradley, "Thulium-doped tellurium oxide waveguide amplifier with 7.6 dB net gain on a silicon nitride chip," *Opt. Lett.* **44**(23), 5788–5791 (2019).

The author has also contributed to the following published papers, conferences, presentations, and proceedings:

- **K. Miarabbas Kiani**, H. M. Mbonde, H. C. Frankis, R. Mateman, A. Leinse, A. P. Knights, and J. D. B. Bradley, "Four-wave mixing in high-*Q* tellurium-oxide-coated silicon nitride microring resonators," *OSA Continuum* **3**, 3497–3507 (2020).

- H. C. Frankis[1], **K. Miarabbas Kiani[1]**, D. B. Bonnevile, C. Zhang, S. Norris, R. Mateman, A. Leinse, N. D. Bassim, A. P. Knights, and J. D. B. Bradley, "Low-loss TeO_2-coated Si_3N_4 waveguides for application in photonic integrated circuits," *Opt. Express* **27**(9), 12529–12540 (2019).

- H. C. Frankis, **K. Miarabbas Kiani**, D. Su, R. Mateman, A. Leinse, and J. D. B. Bradley, "High-*Q* tellurium-oxide-coated silicon nitride microring resonators," *Opt. Lett.* **44**(1), 118–121 (2019).

---

[1] These authors contributed equally to this work.

- **K. Miarabbas Kiani**, D. B. Bonneville, A. P. Knights and J. D. B. Bradley, "High-Q-factor tellurium oxide clad silicon microring resonators," *2021 IEEE 17th International Conference on Group IV Photonics (GFP) (The best presentation award)*, FC3, 1-2 (2021).

- J. D.B. Bradley, **K. Miarabbas Kiani**, H. C Frankis, D. B Bonneville, H. Mbonde, C. M Naraine, B. S. Frare, and A. P Knights, "Recent progress in rare earth devices for silicon photonics," *Photonics West, Hybrid Integration, (International Society for Optics and Photonics, invited)* 12006–14 (2022).

- **K. Miarabbas Kiani**, H. C. Frankis, C. M. Naraine, D. B. Bonneville, A. P. Knights, and J. D. B. Bradley, "A Thulium-silicon hybrid microdisk laser," *OSA Advanced Photonics Congress (Postdeadline presentation)*, JTh3A.2 (2021).

- **K. Miarabbas Kiani**, H. C. Frankis, R. Mateman, A. Leinse, A. P. Knights, and J. D. B. Bradley, "High gain thulium-doped tellurium oxide waveguide amplifier for optical communication in the 2-µm window," *Photonics North (PN)*, 1-1 (2021).

- D. Bonneville, **K. Miarabbas Kiani**, H. Frankis, R. Arbi, M. Munir, M. Albert, K. Sask, A. Turak, A. Knights, and J. Bradley, "Hybrid Si-TeO_2 waveguide Bragg resonators coated in PMMA for biological sensing," *Photonics North (PN)*, Virtual, 1-1 (2021).

- **K. Miarabbas Kiani**, H. C. Frankis, R. Mateman, A. Leinse, A. P. Knights, and J. D. B. Bradley, "Thulium-doped tellurium oxide laser for optical communication at 2-µm window," *Conference on Lasers and Electro-Optics, CLEO, OSA Technical Digest*, SM1A.6. (2021).

- J. D. B. Bradley, H. C Frankis, **K. Miarabbas Kiani**, D. Bonneville, H. Mbonde, R. Wang, A. P Knights, R. Mateman, A. Leinse, N. Singh, E. P Ippen, and F. X Kärtner, "Progress on a hybrid tellurite glass and silicon nitride waveguide platform for passive, active, and nonlinear photonic integrated circuits," *Integrated Optics: Devices, Materials, and Technologies XXV, International Society for Optics and Photonics (invited)*, **11689**, (2021).

- **K. Miarabbas Kiani**, H. C. Frankis, H. M. Mbonde, R. Mateman, A. Leinse, A. P. Knights, and J. D. B. Bradley, "Four wave mixing in tellurium-oxide-coated silicon nitride microring resonators," *Photonics North (PN)*, 1-2 (2020).

- H. M. Mbonde, **K. Miarabbas** Kiani, H. C. Frankis, and J. D. B. Bradley "TeO_2-coated Si_3N_4 waveguides with engineered dispersion and enhanced nonlinearity," Conference on Lasers and Electro-Optics, *CLEO*, *OSA Technical Digest*, JTu2F.33 (2020).

- **K. Miarabbas Kiani**, H. C. Frankis, R. Mateman, A. Leinse, A. P. Knights, and J. D. B. Bradley, "Thulium-doped tellurium oxide amplifier for optical communication in the 2-µm window on a silicon nitride integrated optics platform," *41st Photonics & Electromagnetics Research Symposium (Progress in Electromagnetics Research Symposium, PIERS)*, University of Rome "La Sapienza", Rome, Italy, June (2019).

- **K. Miarabbas Kiani**, H. C. Frankis, R. Mateman, A. Leinse, A. P. Knights, and J. D. B. Bradley, "Thulium-doped tellurium oxide amplifier for optical communication in the 2-μm window," *21st Photonics North conference*, Quebec City convention center, Montreal, Canada, May (2019).
- J. D. B. Bradley, H. C. Frankis, **K. Miarabbas Kiani**, D. B. Bonneville, D. Su, R. Mateman, A. Leinse, and A. P. Knights, "Tellurite glass devices for silicon-based photonic integrated circuits," *41st PhotonIcs & Electromagnetics Research Symposium (Progress in Electromagnetics Research Symposium, PIERS*), University of Rome, La Sapienza, Rome, Italy, June (2019).
- H. Frankis, **K. Miarabbas Kiani**, D. Bonneville, C. Zhang, S. Norris, R. Mateman, A. Leinse, N. D. Bassim, A. P. Knights, and J. D. B. Bradley, "Low-loss TeO_2 waveguides integrated on a Si_3N_4 platform for active and nonlinear optical devices," *Conference on Laser and Electro-Optics, CLEO*, San Jose Convention Center, San Jose, California, USA, May (2019).
- H. Frankis, **K. Miarabbas Kiani**, D. Bonneville, C. Zhang, S. Norris, R. Mateman, A. Leinse, N. D. Bassim, A. P. Knights, and J. D. B. Bradley, "Low-loss TeO_2 waveguides integrated on a Si_3N_4 platform for active and nonlinear optical devices," *Conference on Laser and Electro-Optics, CLEO*, San Jose Convention Center, San Jose, California, USA, May (2019).

- **K. Miarabbas Kiani**, A. P. Knights, J. D. B. Bradley, S. Norris, and N. D. Bassim, "Improved fiber-chip coupling in waveguides by focused ion beam modification," *11th Annual FIB SEM Workshop*, McMaster University, Hamilton, ON, Canada, April (2018).

- J. D. B. Bradley, H. C. Frankis, **K. Miarabbas Kiani**, D. Su, R. Mateman, and A. Leinse, "High-Q tellurite glass microring resonators on a low-loss silicon-nitrideintegrated optics platform," *OPTO, Photonics West, Technical Abstract Summaries, Conference "Integrated Optics: Devices, Materials, and Technologies XXIII,"* Session 9, paper 10921-38San Francisco, California, (2019).

Bibliography

[1] Z. W. Xu, "Cloud-sea computing systems: Towards thousand-fold improvement in performance per watt for the coming zettabyte era," *J. Comput. Sci. Technol.* **29**(2), 177–181 (2014).

[2] D. J. Richardson, "Filling the light pipe," *Science* **330**, 327 (2010).

[3] R. Soref, "Enabling 2 μm communications," *Nat. Photonics* **9**, 358 (2015).

[4] F. C. Garcia Gunning, N. Kavanagh, E. Russell, R. Sheehan, J. O'Callaghan, and B. Corbett, "Key enabling technologies for optical communications at 2000 nm," *Appl. Opt.* **57**(22), E64 (2018).

[5] Z. Li, A. M. Heidt, N. Simakov, Y. Jung, J. M. O. Daniel, S. U. Alam, and D. J. Richardson, "Diode-pumped wideband thulium-doped fiber amplifiers for optical communications in the 1800 – 2050 nm window," *Opt. Express* **21**, 26450–26455 (2013).

[6] K. Scholle, S. Lamrini, P. Koopmann, and P. Fuhrberg, “2 μm laser sources and their possible applications,” *Frontiers in Guided Wave Optics and Optoelectronics* (InTech, 2010).

[7] Q. Wang, J. Geng, and S. Jiang, “2-μm fiber laser sources for sensing,” *Opt. Eng.* **53**, 061609 (2014).

[8] R. Rickman, “The commercialization of silicon photonics,” *Nat. Photonics* **8**, 579–582 (2014).

[9] X. Chen, M. M. Milosevic, S. Stankovic´, S. Reynolds, T. D. Bucio, K. Li, D. J. Thomson, F. Gardes, and G. T. Reed, “The emergence of silicon photonics as a flexible technology platform,” *Proc. IEEE* **106**, 2101–2116 (2018).

[10] A. E.-J. Lim, J. Song, Q. Fang, C. Li, X. Tu, N. Duan, K. K. Chen, R. P.-C. Tern, and T.-Y. Liow, “Review of silicon photonics foundry efforts,” *IEEE J. Sel. Top. Quantum Electron.* **20**, 8300112 (2014).

[11] V. Stojanović, R. J. Ram, M. Popović, S. Lin, S. Moazeni, M. Wade, C. Sun, L. Alloatti, A. Atabaki, F. Pavanello, N. Mehta, and P. Bhargava, “Monolithic silicon-photonic platforms in state-of-the-art CMOS SOI processes [Invited],” *Opt. Express* **26**, 13106–13121 (2018).

[12] A. Rahim, J. Goyvaerts, B. Szelag, J.-M. Fedeli, P. Absil, T. Aalto, M. Harjanne, C. Littlejohns, G. Reed, G. Winzer, S. Lischke, L. Zimmermann, D. Knoll, D. Geuzebroek, A. Leinse, M. Geiselmann, M. Zervas, H. Jans, A. Stassen, C. Dominguez, P. Munoz, D. Domenech, A. Lena Giesecke, M. C. Lemme, and R. Baets, “Open-access silicon photonics platforms in Europe,” *IEEE J. Sel. Top. Quantum Electron.* **25**, 8200818 (2019).

[13] Smart CutTM technology - Soitec. https://www.soitec.com/en/products/smart-cut.

[14] R. Soref, “Mid-infrared photonics in silicon and germanium,” *Nature Photonics* **4**(8), 495–497, (2010).

[15] W. Cao, D. Hagan, D. J. Thomson, M. Nedeljkovic, C. G. Littlejohns, A. Knights, S. Alam, J. Wang, F. Gardes, W. Zhang, S. Liu, K. Li, M. Said Rouifed, G. Xin, W. Wang, H. Wang, G. T. Reed, and G. Z. Mashanovich, “High-speed silicon modulators for the 2 μm wavelength band,” *Optica* **5**(9), 1055–1062 (2018).

[16] S. E. Miller, “Integrated optics: An introduction,” *Bell Syst. Tech. J.* **48**(7), 2059–2069 (1969).

[17] C. Gunn, “CMOS photonics for high-speed interconnects,” *IEEE Micro* **26**(2):58 – 66, (2006).

[18] R. Soref, “The past, present, and future of silicon photonics,” *IEEE J. Sel. Top. Quantum Electron.* **12**(6), 1678-1687 (2006).

[19] C. V. Poulton, M. J. Byrd, P. Russo, E. Timurdogan, M. Khandaker, D. Vermeulen, and M. R. Watts, “Long-range LiDAR and free-space data communication with high-performance optical phased arrays,” *IEEE J. Sel. Top. Quantum Electron.* **25**(5), 1–8 (2019).

[20] A. Fernández Gavela, D. Grajales García, J. C. Ramirez, and L. M. Lechuga, “Last advances in silicon-based optical biosensors,” *Sensors* **16**(3), 285 (2016).

[21] J. C. Adcock, J. Bao, Y. Chi, X. Chen, D. Bacco, Q. Gong, L. K. Oxenløwe, J. Wang, and Y. Ding, “Advances in silicon quantum photonics,” *IEEE J. Sel. Top. Quantum Electron.* **27**(2), 1–24 (2020).

[22] G. Serafino, C. Porzi, F. Falconi, S. Pinna, M. Puleri, A. D'Errico, A. Bogoni, and P. Ghelfi, "Photonics-assisted beamforming for 5G communications," *IEEE Photon. Technol. Lett.* **30**(21), 1826–1829 (2018).

[23] R. Sabella, "Silicon photonics for 5G and future networks," *IEEE J. Sel. Top. Quantum Electron.* **26**(2), 1–11 (2019).

[24] J. J. Ackert, D. J. Thomson, L. Shen, A. C. Peacock, P. E. Jessop, G. T. Reed, G. Z. Mashanovich, and A. P. Knights, "High-speed detection at two micrometres with monolithic silicon photodiodes," *Nat. Photonics* **9**(6), 393–396, (2015).

[25] D. J. Blumenthal, R. Heideman, D. Geuzebroek, A. Leinse, and C. Roeloffzen, "Silicon nitride in silicon photonics," *Proc. IEEE* **106**(12), 2209–2231 (2018).

[26] J. Mu, M. Dijkstra, J. Korterik, H. Offerhaus, and S. M. García-Blanco, "High-gain waveguide amplifiers in Si_3N_4 technology via double-layer monolithic integration," *Photonics Res.* **8**(10), 1634–1641 (2020).

[27] A. L. Gaeta, M. Lipson, and T. J. Kippenberg, "Photonic-chip-based frequency combs," *Nat. Photonics* **13**(3), 158–169 (2019).

[28] K. Miarabbas Kiani, H. M. Mbonde, H. C. Frankis, R. Mateman, A. Leinse, A. P. Knights, and J. D. B. Bradley, "Four-wave mixing in high-*Q* tellurium-oxide-coated silicon nitride microring resonators," *OSA Continuum* **3**(12), 3497–3507 (2020).

[29] T. Barwicz, M. Popović, P. Rakich, M. Watts, H. Haus, E. Ippen, and H. Smith, "Microring-resonator-based add-drop filters in SiN: fabrication and analysis," *Opt. Express* **12**(7), 1437–1442 (2004).

[30] K. Miarabbas Kiani, H. M. Mbonde, H. C. Frankis, R. Mateman, A. Leinse, A. P. Knights, and J. D. B. Bradley, “Four wave mixing in tellurium-oxide-coated silicon nitride ring resonator," *Photonics North (PN),* 1-2 (2020).

[31] K. Miarabbas Kiani, H. C. Frankis, H. M. Mbonde, R. Mateman, A. Leinse, A. P. Knights, and J. D. B. Bradley, “Thulium-doped tellurium oxide waveguide amplifier with 7.6 dB net gain on a silicon nitride chip,” *Opt. Lett.* **44**, 5788-5791 (2019).

[32] K. Miarabbas Kiani, H. C. Frankis, R. Mateman, A. Leinse, A. P. Knights, and J. D. B. Bradley, “Thulium-doped tellurium oxide microring lasers integrated on a low-loss silicon nitride platform,” *Opt. Mater. Express* **11**, 3656-3665 (2021).

[33] N. Li, D. Vermeulen, Z. Su, E. S. Magden, M. Xin, N. Singh, A. Ruocco, J. Notaros, C. V. Poulton, E. Timurdogan, C. Baiocco, and M. R. Watts, “Monolithically integrated erbium-doped tunable laser on a CMOS compatible silicon photonics platform,” *Opt. Express* **26**(13), 16200–16211 (2018).

[34] I. Goykhman, B. Desiatov, and U. Levy, “Ultrathin silicon nitride microring resonator for biophotonic applications at 970 nm wavelength,” *Appl. Phys. Lett.* **97**(8), 081108 (2010).

[35] R. Wang, A. Vasiliev, M. Muneeb, A. Malik, S. Sprengel, G. Boehm, M.-C. Amann, I. Šimonytė, A . Vizbaras, K. Vizbaras, R. Baets, G. Roelkens, “III–V-on-silicon photonic integrated circuits for spectroscopic sensing in the 2–4 μm wavelength range,” *Sensors*. **17**(8), (2017).

[36] Y. Fan, J. P. Epping, R. M. Oldenbeuving, C. G. H. Roeloffzen, M. Hoekman, R. Dekker, R. G. Heideman, P. J. M. van der Slot, and K.-J. Boller, "Optically integrated InP-Si_3N_4 hybrid laser," *IEEE Photonics J.* **8**(6), 1505111 (2016).

[37] J.P. Gordon, H.J. Zeiger, C.H. Townes, "The maser—new type of microwave amplifier, frequency standard, and spectrometer," *Phys. Rev.* **99**, 1264–1274 (1955).

[38] T.H. Maiman, "Stimulated optical radiation in ruby," *Nature* **187**, 493–494 (1960).

[39] M. Pollnau, "Rare-earth-doped waveguide amplifiers and lasers," Handbook on the Physics and Chemistry of Rare Earths **51**, 111-168 (2017).

[40] H. Rong, S. Xu, Y. Kuo, V. Sih, O. Cohen, O. Raday, and M. Paniccia, "Low-threshold continuous-wave Raman silicon laser," *Nat. Photonics* **1**, 232–237 (2007).

[41] M. J. R. Heck, J. F. Bauters, M. L. Davenport, J. K. Doylend, S. Jain, G. Kurczveil, S. Srinivasan´, Y. Tang, and J. E. Bowers, "Hybrid silicon photonic integrated circuit technology," *IEEE J. Sel. Top. Quantum Electron.* **19**, 6100117 (2013).

[42] A. Elbaz, D. Buca, N. Driesch, K. Pantzas, G. Patriarche, N. Zerounian, E. Herth, X. Checoury, S. Sauvage, I. Sagnes, A. Foti, R. Ossikovski, J.-M. Hartmann, F. Boeuf, Z. Ikonic, P. Boucaud, D. Grützmacher, and M. El Kurdi, "Ultra-low-threshold continuous-wave and pulsed lasing in tensile-strained GeSn alloys," *Nat. Photonics* **14**, 375–382 (2020).

[43] D. Korn, M. Lauermann, S. Koeber, P. Appel, L. Alloatti, R. Palmer, P. Dumon, W. Freude, J. Leuthold, and C. Koos, "Lasing in silicon-organic hybrid waveguides," N*at. Commun.* **7**, 10864 (2016).

[44] Z. Wang, A. Abbasi, U. Dave, A. De Groote, S. Kumari, B. Kunert, C. Merckling, M. Pantouvaki, Y. Shi, B. Tian, K. Van Gasse, J. Verbist, R. Wang, W. Xie, J. Zhang, Y. Zhu, J. Bauwelinck, X. Yin, Z. Hens, J. Van Campenhout, B. Kuyken, R. Baets, G. Morthier, D. Van Thourhout, G. Roelkens, "Novel light source integration approaches for silicon photonics," *Laser Photonics Rev.* **11**, 1700063 (2017).

[45] M. Tang, J.-S. Park, Z. Wang, S. Chen, P. Jurczak, A. Seeds, H. Liu, "Integration of III-V lasers on Si for Si photonics," *Prog. Quantum Electron.* **66**, 1-18 (2019).

[46] E. Snitzer, "Optical MASER action of Nd^{3+} in a barium crown glass," *Phys. Rev. Lett.* **7**, 444–446 (1961).

[47] C. J. Koester, E. Snitzer, "Amplification in a fiber laser," *Appl. Optics* **3**, 1182–1186 (1964).

[48] K. Miarabbas Kiani, H. C Frankis, C. M Naraine, D. B Bonneville, A. P Knights, J. D. B. Bradley, "Lasing in a hybrid rare-earth silicon microdisk," *Laser & Photonics Rev.* 2100348 (2021).

[49] R. Soulard, A. Zinoviev, J. L. Doualan, E. Ivakin, O. Antipov, and R. Moncorgé, "Detailed characterization of pump-induced refractive index changes observed in Nd:YVO_4, Nd:$GdVO_4$ and Nd:KGW," *Opt. Express* **18**, 1553–1568 (2010).

[50] J. D. B. Bradley, M. Costa de Silva, M. Gay, L. Bramerie, A. Driessen, K. Wörhoff, J.-C. Simon, and M. Pollnau, "170 Gbit/s transmission in an erbium-doped waveguide amplifier on silicon," *Opt. Express* **17**, 22201–22208 (2009).

[51] N. Li, "Rare-earth-doped lasers on silicon photonics platform," PhD dissertation, *Harvard* University Cambridge, Massachusetts (2018).

[52] Q. Nie, X. Li, S. Dai, T. Xu, Z. Jin, and X. Zhang, “Energy transfer and upconversion luminescence in Tm^{3+}/Yb^{3+} co-doped lanthanum-zinc-lead tellurite glasses,” *J. of Luminescence* **128**, 135-141 (2008).

[53] L. Xu, B. Song, S. Xiao, and J. LU, “Up-conversion luminescence of Tm^{3+} /Yb^{3+} co-doped oxy-fluoride glasses,” *J. of Rare Earths* **28**, 194-197 (2010).

[54] A. Godard, “Infrared 2-12 pm solid-state laser sources: a review,” *Comptes Rendus Physique* **8**, 1100-1128 (2007).

[55] E. R. M. Taylor, L. N. Ng, J. Nilsson, R. Caponi, A. Pagano, M. Potenza, and B. Sordo, “Thulium-doped tellurite fiber amplifier” *IEEE Photon. Technol. Lett.* **16**(3), 777–779 (2004).

[56] L. F. Johnson, J. E. Geusic, and L. G. V. Uitert, “Coherent oscillations from Tm^{3+}, Ho^{3+}, Yb^{3+} and Er^{3+} ions in yttrium aluminum garnet,” *Appl. Phys. Letters* **7** (5), 127 (1965).

[57] J. A. Caird, L. G. DeShazer, and J. Nella, “Characteristics of room-temperature 2.3 μm laser emission from Tm^{3+} in YAG and $YALO_3$,” *IEEE J. Quantum Electron.* **11**, 874–881 (1975).

[58] D. G. Lancaster, S. Gross, H. Ebendorff-Heidepriem, A. Fuerbach, M. J. Withford, and T. M. Monro, “2.1 μm waveguide laser fabricated by femtosecond laser direct-writing in Ho^{3+}, Tm^{3+}:ZBLAN glass,” *Opt. Lett.* **37**(6), 996–998 (2012).

[59] S. Rivier, X. Mateos, V. Petrov, U. Griebner, Y. E. Romanyuk, C. N. Borca, F. Gardillou, and M. Pollnau, “Tm:$KY(WO_4)_2$ waveguide laser,” *Opt. Express* **9**, 5885–5892 (2007).

[60] Z. Li, A. M. Heidt, J. M. O. Daniel, Y. Jung, S. U. Alam, and D. J. Richardson, “Thulium-doped fiber amplifier for optical communications at 2 μm,” *Opt. Express* **21**, 9289-9297 (2013).

[61] J. Wang, S. Liang, Q. Kang, Y. Jung, S. Alam, and D. J. Richardson, “Broadband silica-based thulium doped fiber amplifier employing multi-wavelength pumping,” *Opt. Express* **24**, 23001-23008 (2016).

[62] K. van Dalfsen, S. Aravazhi, C. Grivas, S. M. García-Blanco, and M. Pollnau, “Thulium channel waveguide laser in a monoclinic double tungstate with 70% slope efficiency,” *Opt. Lett.* **37**, 887-889 (2012).

[63] K. van Dalfsen, S. Aravazhi, C. Grivas, S. M. García-Blanco, and M. Pollnau, “Thulium channel waveguide laser with 1.6W of output power and 80% slope efficiency,” *Opt. Lett.* **39**, 4380-4383, (2014).

[64] Z. Su, N. Li, E. Salih Magden, M. Byrd, Purnawirman, T. N. Adam, G. Leake, D. Coolbaugh, J. D. B. Bradley, and M. R. Watts, “Ultra compact and low-threshold thulium microcavity laser monolithically integrated on silicon,” *Opt. Lett.* **41**, 5708-5711, (2016).

[65] J. S. Wang, E.M. Vogel, E. Snitzer, “Tellurite glass: a new candidate for fiber devices,” *Opt. Mater.* **3**, 187-203 (1994).

[66] S. H. Kim, T. Yoko, and S. Sakka, “Linear and nonlinear optical properties of TeO_2 glass,” *J. Am. Ceram. Soc.* **76**(10), 2486–2490 (1993).

[67] A. Jha, B. D. O Richards, G. Jose, T. T. Fernandez, C. J. Hill, J. Lousteau, and P. Joshi, “Review on structural, thermal, optical and spectroscopic properties of tellurium

oxide based glasses for fibre optic and waveguide applications," *Int. Mater. Rev.* **57**(6), 357–382 (2012).

[68] H. H. Li, "Refractive index of silicon and germanium and its wavelength and temperature derivatives," *J. Phys. Chem. Ref. Data* **9**(3), 561–658 (1993).

[69] K. Luke, Y. Okawachi, M. R. E. Lamont, A. L. Gaeta, and M. Lipson, "Broadband mid-infrared frequency comb generation in a Si_3N_4 microresonator," *Opt. Lett.* **40**(21) 4823–4826 (2015).

[70] A. Jha, B. Richards, G. Jose, T. Teddy-Fernandez, P. Joshi, X. Jiang, and J. Lousteau, "Rare-earth ion doped TeO_2 and GeO_2 glasses as laser materials," *Prog. Mater. Sci.* **57**(8), 1426–1491 (2012).

[71] R. Stegeman, L. Jankovic, H. Kim, C. Rivero, G. Stegeman, K. Richardson, P. Delfyett, Y. Guo, A. Schulte, and T. Cardinal, "Tellurite glasses with peak absolute Raman gain coefficients up to 30 times that of fused silica," *Opt. Lett.* **28**(13), 1126–1128 (2003).

[72] T. Yano, A. Fukumoto, and A. Watanabe, "Tellurite glass: A new acoustooptical material," *J. Appl. Phys.* **42**(13), 1126–1128 (2003).

[73] R. Nayak, V. Gupta, A. L. Dawar, and K. Sreenivas, "Optical waveguiding in amorphous tellurium oxide thin films," *Thin Solid Films* **445**(1), 118–126 (2003).

[74] G. Qin, A. Mori, and Y. Ohishi, "Brillouin lasing in a single-mode tellurite fiber," *Opt. Lett.* **32**(15), 2179–2181 (2007).

[75] S. M. Pietralunga, M. Lanata, M. Ferè, D. Piccinin, G. Cusmai, M. Torregiani, and M. Martinelli, "High-contrast waveguides in sputtered pure TeO_2 glass thin films," *Opt. Express* **16**(26), 21662–21670 (2008).

[76] S. V. Muravyev, E. A. Anashkina, A. V. Andrianov, V. V. Dorofeev, S. E. Motorin, M. Y. Koptev, and A. V. Kim, "Dual-band Tm^{3+}-doped tellurite fiber amplifier and laser at 1.9 μm and 2.3 μm," *Sci. Rep.* **8**, 16164 (2018).

[77] F. Fusari, S. Vetter, A.A. Lagatsky, B. Richards, S. Calvez, A. Jha, M.D. Dawson, W. Sibbett, C.T.A. Brown, "Tunable laser operation of a Tm^{3+}-doped tellurite glass laser near 2μm pumped by a 1211nm semiconductor disk laser," *Opt. Mater.* **32**(9), 1007-1010 (2010).

[78] F. Vanier, F. Côté, M. El Amraoui, Y. Messaddeq, Y. Peter, and M. Rochette, "Low-threshold lasing at 1975 nm in thulium-doped tellurite glass microspheres," *Opt. Lett.* **40**, 5227-5230 (2015).

[79] A. Li, W. Li, M. Zhang, Y. Zhang, S. Wang, A. Yang, Z. Yang, E. Lewis, G. Brambilla, and P. Wang, "Tm^{3+}-Ho^{3+} codoped tellurite glass microsphere laser in the 1.47 μm wavelength region," *Opt. Lett.* **44**, 511-513 (2019).

Chapter 2

Background and Theory

Preface

This chapter serves as a comprehensive background on the theory and properties of the straight waveguides, curved waveguides, microring resonators (MRRs), microdisk resonators (MDRs), and thulium-doped gain media relevant to the optical amplifiers and lasers for the thulium-doped fiber amplifier (TDFA)-band, centered near 1900 nm investigated in this thesis.

The basic building block of silicon photonic systems is the waveguide. In section 2.2, basic waveguide concepts including optical modes, the effective index, the single-mode cut-off width, and confinement factors are determined for 220 nm thick SOI and 200 nm thick silicon nitride (Si_3N_4) at 1550 and 2000 nm wavelengths and key results of waveguide theory are presented for a general understanding of the nature of light propagation in optical waveguides. Then, loss or attenuation that a light wave experiences as it goes through the guide and significantly impacts device performance is discussed. This loss is typically divided to three different mechanisms: scattering, absorption, and radiation which will be explained in section 2.2.

Optical traveling-wave resonators have demonstrated prominent potential for the realization of compact photonic functionalities. High-refractive-index contrast silicon and silicon nitride waveguides enable dense and large-scale integration of functionalized resonators for photonic integrated devices in a CMOS-compatible technology platform. Section 2.3 provides a description of the properties of the ring and disk resonators which pertain to much of the contents of this thesis.

It is essential to understand the spectroscopic properties of rare earth elements in order to design rare-earth-doped optical waveguide devices such as amplifiers and lasers. In section 2.4, the fundamental atomic properties of rare-earth ions and their behavior in glass host materials are reviewed. In section 2.5, the properties of the rare earth element of interest for this work, thulium, are described, including its energy transitions and spectroscopy as well as the amplifier and laser theory of thulium-doped waveguides. The science behind all-optical amplification and methods of modeling active rare-earth-based integrated optical devices are presented in section 2.5.

2.1 Introduction

Since 1960, when the first laser was developed as a stable source of coherent light, the processing and transmission of the signals carried by optical beams have been an interesting topic [1]. The concept of “integrated optics” emerged in the late 1960s, to replace the conventional electrical integrated circuits with miniaturized photonic integrated circuits (PICs). It attracted significant interest for its small sizes, thermal and mechanical stability, and various applications. The preliminary development of many basic integrated photonic components and their fundamental theory has been explored in the early 1970’s [2]. In the1990’s, silicon (Si) has been developed as a photonic material (silicon photonics) [3]. Then the development of PICs for high-speed interconnects and processing infrastructure came in the early 2000’s [4].

Silicon photonics provides the opportunity to photonic devices onto chips with significant advantages over bulk and fiber-based optical systems, including compact size, low cost, improved thermal and mechanical stability, and high volumes through wafer-scale processing techniques [3,5]. Currently, high-quality silicon photonics chips are fabricated in the process of transitioning into a ‘fabless’ industry. Thus, silicon integrated photonics is shifting mainly towards silicon-on-insulator (SOI) [5], and silicon nitride-on-insulator [6] based waveguides due to the CMOS infrastructure compatible processing.

2.2 Waveguides

A waveguide provides a pathway for an electromagnetic wave to travel through a medium. Waveguides are the basic components in the photonics toolbox, allowing for the confinement and guiding of light (i.e., electromagnetic waves) in fiber-optic systems and photonic integrated circuits. Generally, a waveguide is composed of a central core of a given refractive index n_1 surrounded by cladding material of refractive index n_2. Light can be confined and guided if $n_1 > n_2$ [7–9]. In this section, the key concept of optical modes in waveguiding structures and waveguide theory are presented to understand light propagation in an optical waveguide, as well as a brief explanation about two types of channel waveguides that have been used in this thesis.

2.2.1 Total Internal Reflection

Light is guided in a waveguide through a phenomenon called total internal reflection (TIR). In the ray-optic description, an electromagnetic wave that travels through a dielectric medium with a refractive index of n_1 (medium 1) reaches an interface between medium 1 and a dielectric medium with a refractive index of n_2 (medium 2) at an incident angle θ_i relative to the interface, as shown in figure 2.1. Part of the incident wave is transmitted (refracted) through the interface into medium 2, while the remainder is reflected back into medium 1 at a reflected angle of θ_r. Total internal reflection is the reflection of the total amount of incident light at the boundary between two media and implies that the energy dissipation caused by interaction at the interface confines the wave strictly to medium 1 [7–9]. When the incident angle is larger than the critical angle (θ_c), then total internal reflection occurs as described by equation 2.1:

$$\theta_i > \theta_c = \sin^{-1}({}^{n_2}/_{n_1}) \tag{2.1}$$

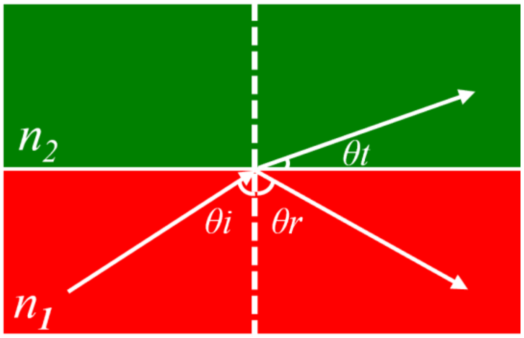

FIGURE 2.1: Ray-optic depiction of reflection and refraction of an electromagnetic wave at a dielectric interface.

2.2.2 Planar Waveguides

A planar waveguide is the simplest geometry of an optical waveguide, consisting of three layers including the substrate, core, and top cladding layer, with the refractive indices of n_1, n_2, and n_3, respectively, as has been illustrated in figure 2.2.

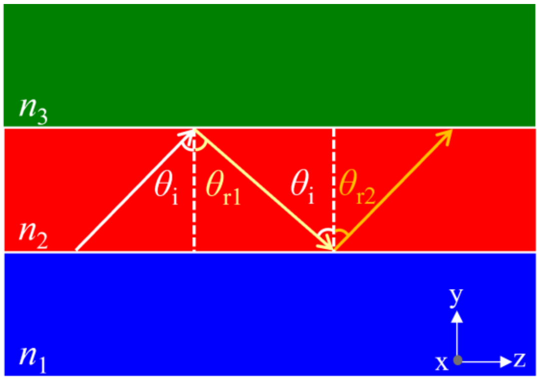

FIGURE 2.2: Total internal reflection in a dielectric planar waveguide.

Light is fully confined and guided into the core layer if $n_2 > n_1$ and $n_2 > n_3$ using the explanation of the total internal reflection and if the angles of the light incident on the cladding and substrate layers are greater than the following critical angles (θ_{c1}, θ_{c2}).

$$n_2 > n_1 \text{ and } n_2 > n_3 \tag{2.2}$$

$$\theta_{r1} \geq \theta_{c1} = \sin^{-1}({}^{n_3}/_{n_2}) \text{ and } \theta_{r2} \geq \theta_{c2} = \sin^{-1}({}^{n_1}/_{n_2}) \tag{2.3}$$

Based on the planar waveguide structure shown in figure 2.2, a guided wave confined to the core layer will propagate through the waveguide in the *z* direction. Then, a phase shift will occur every time the wave hits an interface. The direction of the propagation of the electromagnetic wave and the phase change of the electromagnetic wave per unit length in the waveguide are determined by wave vector of $k = 2\pi/\lambda$. It depends on the phase difference between the two counter-propagating waves, the field patterns will interfere constructively or destructively. If constructive interference happens, guided modes will occur in the *z* direction of the waveguide.

Assuming the electromagnetic field of a monochromatic wave is given from Maxwell's self-supporting wave equation [1], it can be written as:

$$E(r,t) = E(r)e^{i\omega t} \tag{2.4}$$

where $E(r, t)$ is the position- and time-dependent electric field vector and $\omega = 2\pi f$ is the radian frequency of the wave. The spatial dependence of the mode propagation can then be expanded to three dimensions. The mode profile represents the electric field distribution at various cross sections along with the waveguide structure. As the mode propagates along the *z*-axis, the electric field becomes $E(r) = E(x,y)e^{-i\beta z}$, where $E(x, y)$ represents the electric field profile at a given transverse cross section along the waveguide and $\beta = kn_{eff}$

is the propagation constant and a *z* component of the wave vector k. Assuming an infinite slab in the *x*-axis, Maxwell's wave equation reduces to:

$$\frac{\partial^2 E(x,y)}{\partial t^2} + [k^2 n^2 - \beta^2] E(x,y) = 0 \tag{2.5}$$

where n is the refractive index of the waveguiding material (here represents the refractive index of core layer of n_2) and n_{eff} is the effective index [10–13]. The propagation is only dependent on the $[k^2 n^2 - \beta^2]$ term to be exponential or sinusoidal. $E(x, y)$ and $\partial E(x, y)/\partial x$ must be continuous at the interface between layers.

To determine the appropriate geometry of waveguide, and phase matching condition under a standing wave configuration, the following equations are illustrated through the decomposition of the wave vector in the planar waveguide. The phase shift Φ_p that the wave encounters because of the propagation due to alternating wave interactions at the core-cladding interface (Φ_{23}) and the core-substrate interface (Φ_{21}) is written as:

$$\Phi_p = 2hk_0 n_2 cos\theta \tag{2.6}$$

where h is the thickness of the waveguide layer (core layer with refractive index of n_2), k_0 is the wavenumber in vacuum and λ_0 is the wavelength of light in the core layer (core layer). Because the wave is propagating through the waveguide layer (core layer), the wave vector is defined as $k = k_0 n_2$, where $k_0 = \frac{2\pi}{\lambda_0}$. The total phase change for a point on a wavefront that travels from the waveguide-cladding interface to the waveguide-substrate interface and back again must be a multiple of 2π to avoid the decay of optical energy due to the destructive interference of the traveling waves through the waveguide (core). Therefore, the phase-matching condition due to the constructive interference conditions is written as:

$$2\pi m = 2hk_0 n_2 cos\theta + 2\Phi_{21} + 2\Phi_{23} \tag{2.7}$$

where m is the mode number and a positive integer which satisfies the phase matching condition. The $2\Phi_{21}$ and $2\Phi_{23}$ terms are interpreted as penetrations of zig-zag rays of a certain depth into the confining layers before reflection occurs and expressions for these terms are given in [1].

The maximum waveguide (core) thickness that only supports the fundamental mode (single mode waveguides), is written as:

$$h = \frac{\lambda}{2n_2 cos\theta} \tag{2.8}$$

where λ is the wavelength of light. Assuming a silicon-on-insulator (SOI) material configuration with n_2 = 3.5 and n_1 = n_3 = 1.45, the calculated waveguide core thickness at critical angle is ~ 243 nm for 1550 nm and ~ 314 nm for 2000 nm wavelength light using numerical mode solver (RSoft).

2.2.3 Channel Waveguides

Channel waveguides are the basic rectangular waveguide structure consisting of a waveguide region of index n_w surrounded by a confining medium of lower index n_c of top cladding material and n_s as the substrate refractive index, as shown in figure 2.3, which are also called strip waveguides, or 3-dimensional waveguides.

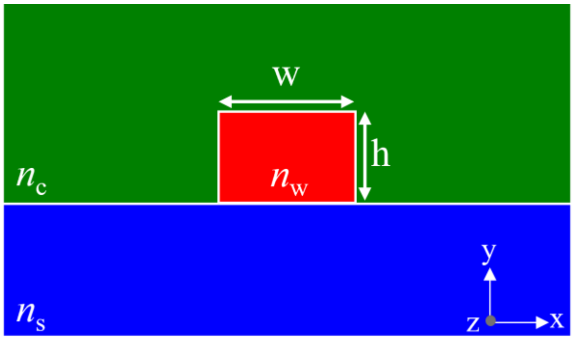

FIGURE 2.3: Channel waveguide structure with the waveguide refractive index n_w, width and thickness of w and h, respectively.

The channel waveguide has geometrical and modal restriction in the x and y axes and is surrounded on all other sides by the cladding material with refractive index n_c. While planar waveguides offer confinement in one dimension, channel waveguides are beneficial by confining light in two dimensions. In this section, both silicon-in-insulator (SOI) channel waveguide and silicon nitride channel waveguide are explained briefly in sections 2.2.4 and 2.2.5, respectively, and then mode calculations of SOI waveguides are performed in section 2.2.5 using Synopsis RSoft [14], a simulation software suite with tools that allow us to design and characterize various photonic devices.

2.2.4 Optical Mode and Effective Index

In silicon on isolator (SOI) platform, a large refractive index contrast between silicon as a core material and silicon dioxide (SiO_2) as a substrate or cladding layer provides the opportunity of micron-scale fabrication into a small footprint photonic circuit. Realization of extremely tight waveguide bends with negligible loss is another benefit of the large index contrast between the core and cladding layer. Figure 2.4 shows the SOI channel waveguides with tellurium oxide as the cladded material investigated in this thesis.

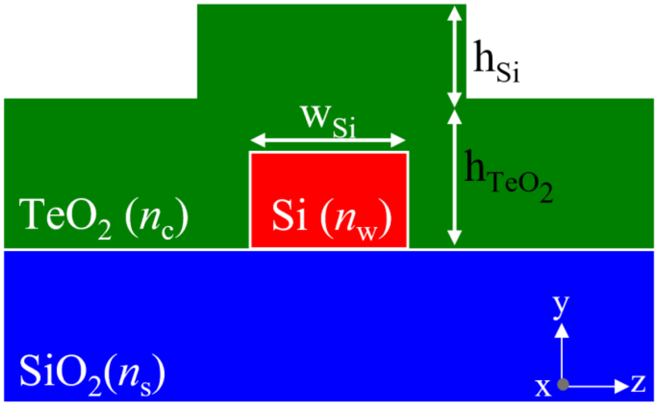

FIGURE 2.4: The cross-section view of tellurium oxide cladded SOI waveguide.

Optical modes are defined as the spatial distribution of optical energy in waveguides in one or more dimensions. Waveguides can support the propagation of light in discrete eigenmodes (referred to as “optical modes”) [1], with an associated propagation constant of β, given by:

$$\beta = k_0 n_{\text{eff}} \tag{2.9}$$

where n_{eff} is the effective index and k_0 is the wavenumber in the vacuum, related to the optical frequency and can be calculated by:

$$k_0 = {}^{\omega}/{}_{c} = 2\pi/\lambda \tag{2.10}$$

where $c = 1/\sqrt{\varepsilon_0\mu_0}$ is the speed of light in vacuum, with ε_0 and μ_0 representing the electric permittivity and magnetic permeability in a vacuum, respectively. Generally, the waveguide supports a mode if $n_c < n_{eff} < n_w$ [7–9]. The SOI waveguide may support TE (transverse electric) and TM (transverse magnetic) modes, and it can be single mode or multimode depending on the material refractive indices and waveguide dimensions. The waveguides discussed in this thesis only support the fundamental TE or TM mode, which is referred to as single-mode operation. The single-mode cut-off-width determines the maximum width of the waveguide core at which only the fundamental mode is supported. A waveguide wider than the single-mode cut-off will support higher-order modes as well. The appropriate width can be found numerically by simulating the effective index of a waveguide via finite element mode solver calculations in software such as RSOFT FemSIM. Figure 2.5 shows the simulated mode profiles of a 400 nm wide silicon waveguide cladding with 400 nm thick TeO_2 for 1550 nm and 2000 nm wavelengths.

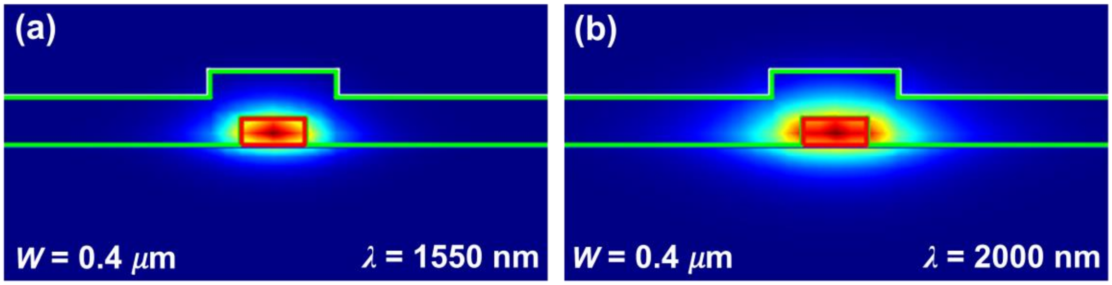

FIGURE 2.5: Sample simulated electric field profiles of the fundamental TE-polarized modes at 1550 and 2000 nm calculated for a silicon (Si) waveguide.

To begin, an SOI slab waveguide is considered, consisting of a silicon slab with the thickness of 220 nm sandwiched between the silicon oxide layer as the substrate and 400 nm- thick tellurium oxide as the cladding layer. The width of the silicon waveguide is considered 400 nm, resulting in a single-mode operation at wavelengths ranging from 1500 nm to 2000 nm. At the wavelength of 2000 nm, the single-mode cut-off is close to 550 nm. Figure 2.6a shows the simulated effective indices of a 220 nm thick strip waveguide with varying widths for 2000 nm wavelength. The fundamental TE_0 mode is supported for the entire range shown, while the fundamental TM_0 mode is only supported at widths > 860 nm. A polarization controller is be used to ensure that only TE or TM polarized light is coupled to the waveguide.

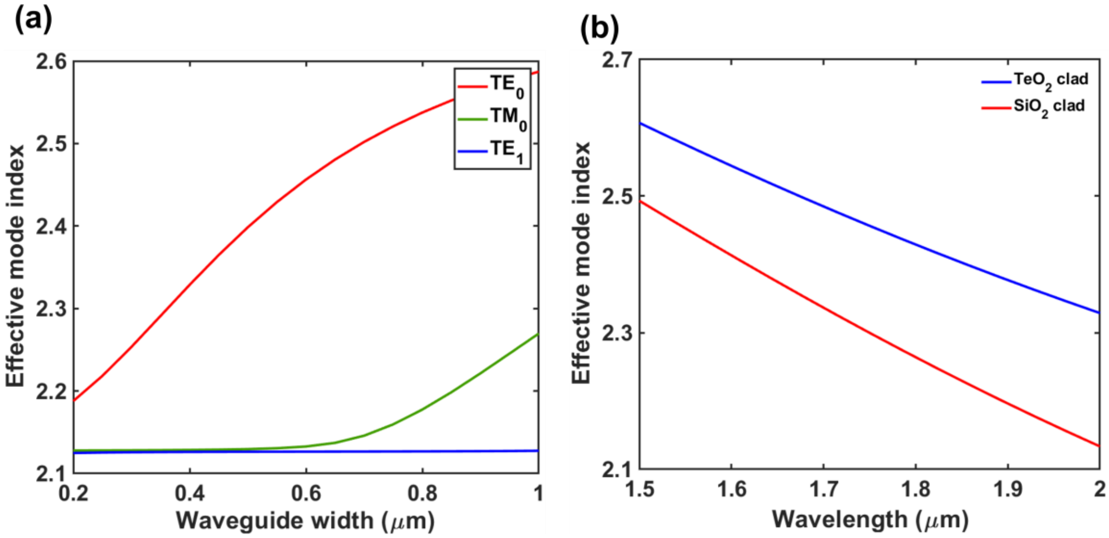

FIGURE 2.6: a) Simulated effective indices of the TE_0, TM_0 and TE_1 modes in SOI strip waveguides with varying width at 2000 nm wavelength. b) Calculated effective refractive index of the fundamental TE mode in a TeO_2-coated silicon waveguide.

Figure 2.6b shows the simulated effective refractive index versus wavelength for 400 nm thick TeO_2 and SiO_2 cladding. For thicker films the waveguide mode becomes more confined in the TeO_2 coating, causing the effective index to rise. The effective index decreases at longer wavelengths due to an expanded optical mode, which overlaps more with the lower refractive index SiO_2 and air as the substrate and top cladding layers, respectively.

2.2.5 Confinement

In silicon photonics lasers and amplifiers, it is important to maximize the overlap of the light with the cladding layer, which is considered an active area. The mode confinement will increase by increasing the cladding thickness and the width of the waveguide above the single-mode cut-off. Figure 2.7 shows the percentage of the optical mode power confined in the waveguide and cladding layer as a function of the wavelength.

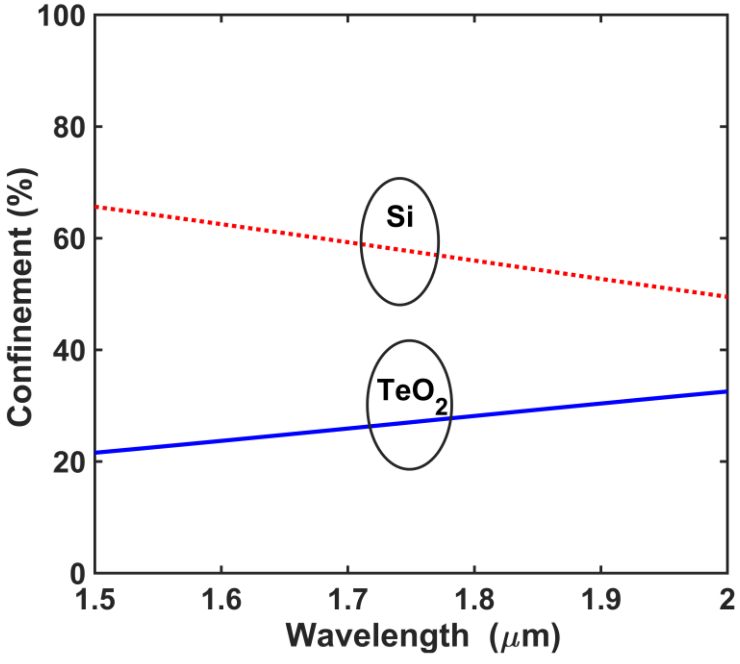

FIGURE 2.7: Optical intensity overlap with the silicon strip and TeO_2 cladding layer.

Large optical confinement in the cladding layer is beneficial to take advantage of its material properties such as amplification and light emission in rare-earth-doped films. The results show that for a 0.4-μm thick TeO_2 coating at a wavelength of 1.5 µm approximately 60% of mode power is confined in the coating, with < 20% confined to the silicon layer, and the rest of the optical power in the air and substrate materials. Thicker TeO_2 coatings can increase the optical confinement, however thicker tellurium oxide coatings in this waveguide structure can increase radiation loss in waveguide bends.

2.2.6 Tellurium Oxide Coated Silicon Nitride Waveguides

Silicon nitride coated with tellurium oxide is another channel waveguide platform that has been demonstrated in this thesis. Silicon nitride (Si_3N_4) is a platform for ultra-low losses throughout the visible and infrared, high performance, and compact photonic integrated circuits (PICs) with high refractive index contrast enabling compact waveguide bends [15–18] capable for volume chip production through standard wafer-scale fabrication steps with nanoscale feature resolution through mature processing techniques [19]. Tellurium oxide (TeO_2) is a promising material for integrated optical devices that is transparent throughout the visible into the mid-infrared with low dispersion. TeO_2 has a relatively high refractive index for a dielectric material (2.08) which is similar to that of Si_3N_4 (1.98), enabling highly compact waveguides and devices.

This new waveguide platform combines the advantages of wafer-scale technology, high-resolution and low-loss waveguides available with Si_3N_4 combined with linear, nonlinear, and active functionalities of tellurium oxide. The most commonly used Si_3N_4 waveguide geometry is the simple strip waveguide cladded with tellurium oxide as shown in this thesis is shown in figure 2.8a. The Si_3N_4 photonic chips were fabricated through the LioniX foundry in the Netherlands, as part of their TriPleX platform [19,20]. Si_3N_4 strip waveguide structures were patterned into a 0.2-µm-thick low-pressure chemical vapor deposition (LPCVD) to be thick enough to avoid Si_3N_4 film cracking due to stress and to achieve sufficient lateral waveguide effective index contrast and to maintain minimal scattering loss [20].

The hybrid silicon nitride waveguide investigated here consists of a silicon nitride (Si_3N_4) strip with the thickness of 200 nm sandwiched between the silicon oxide (SiO_2) layer as the substrate and 400 nm- thick tellurium oxide (TeO_2) as the cladding layer. The width of the silicon nitride waveguide is considered as 1.2 μm to result in single-mode operation at wavelengths of 1550 nm and 2000 nm as shown in figure 2.8b and c, respectively [21].

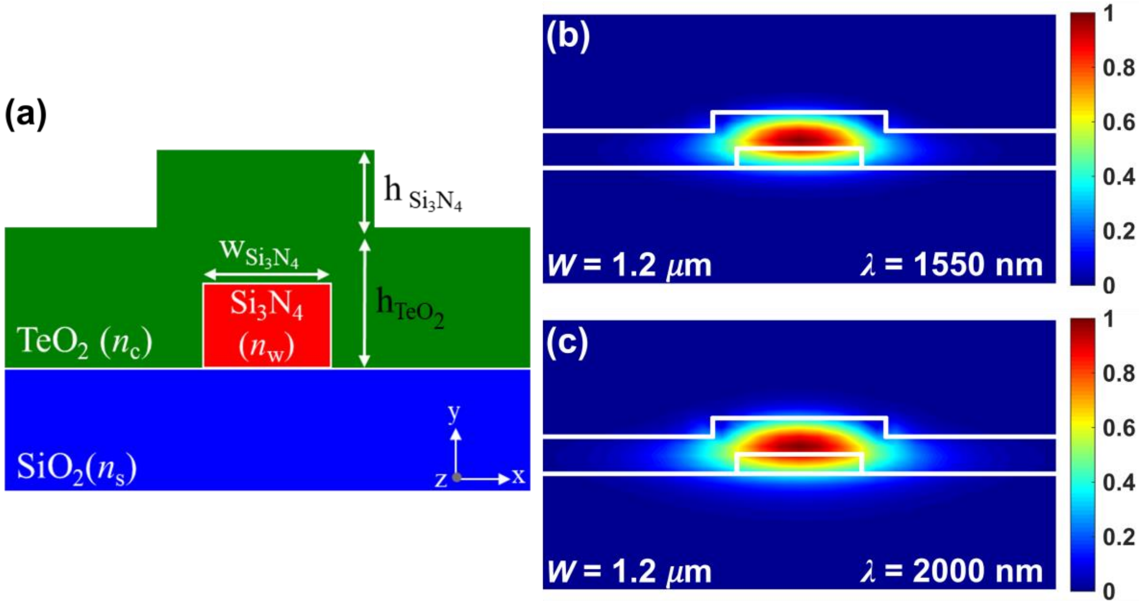

FIGURE 2.8: a) The cross-section view of tellurium oxide-coated Si_3N_4 waveguide. Simulated electric field profile of the fundamental TE-polarized mode calculated for b) 1550 nm wavelength and c) 2000 nm wavelength.

Approximately 70% of mode power is confined in the 0.4-μm thick TeO_2 coating layer with < 20% confined to the nitride layer at a wavelength of 1550 nm. At 2000 nm wavelength, 17% of mode power is confined in silicon nitride layer with 61% confinement in TeO_2 coating layer.

2.2.7 Waveguide Loss Mechanisms

When light wave travels through a medium, it experiences attenuation, or loss, due to scattering, absorption, and radiation, which is one of the most important characteristics of a waveguide. Scattering loss dominates in dielectric waveguides or glass, and absorption loss is more predominant in semiconductors and crystalline materials. When waveguides are bent across a curve, then radiation losses become important [1,10]. Absorption means annihilation of the energy of the photons to atoms or subatomic particles of the absorbing materials. However, scattering or radiation loss means that the photon's direction of travel will change but their identity will be maintained [1,10].

Volume scattering and surface scattering are two forms of scattering loss in an optical waveguide. In comparison with the volume scattering, surface scattering loss can be more significant due to the strong interaction of the propagated wave with the surfaces of the waveguide. Volume scattering is typically negligible compared to surface scattering loss in high optical quality materials and is caused by voids, contamination, imperfections, and defects in the volume of the waveguide. Scattering loss occurs when light interacts to the interface between two media of varying refractive index by a factor of $(n_1^2 - n_2^2)^2$ [22].

The second type of loss is absorption loss which is significant in semiconductors, due to interband and intraband absorptions. In direct bandgap semiconductors, photons with energy greater than the bandgap energy are absorbed to raise electrons from the valence band to the conduction band, causing high absorption.

Radiation losses are usually negligible for well-confined modes in straight waveguides in comparison with scattering loss and absorption loss. However, one of the most important losses for the curved waveguides is radiation loss. Radiation loss can be increased due to the distortions of the optical energy that happens when guided waves move through a bend in a channel waveguide and is no longer guided. Since bent waveguides are an important part of optical integrated circuits, the minimum bend radius is important to consider limiting the radiation loss of the bent waveguide. The radiation related pathways of loss can be effectively minimized in the device by appropriately designing the waveguide to limit bending leakage. The bending radiation losses were calculated for bent SOI waveguides coated with different TeO_2 film thicknesses and bending radii ranging from 40 μm down to 20 μm using the imaginary index of the bent waveguide through eigenmode simulations in Synopsys RSoft, with the results shown in figure 2.9a. The results are converted to the radiation limited quality factor (Q factor) of the microresonators as illustrated in figure 2.9b.

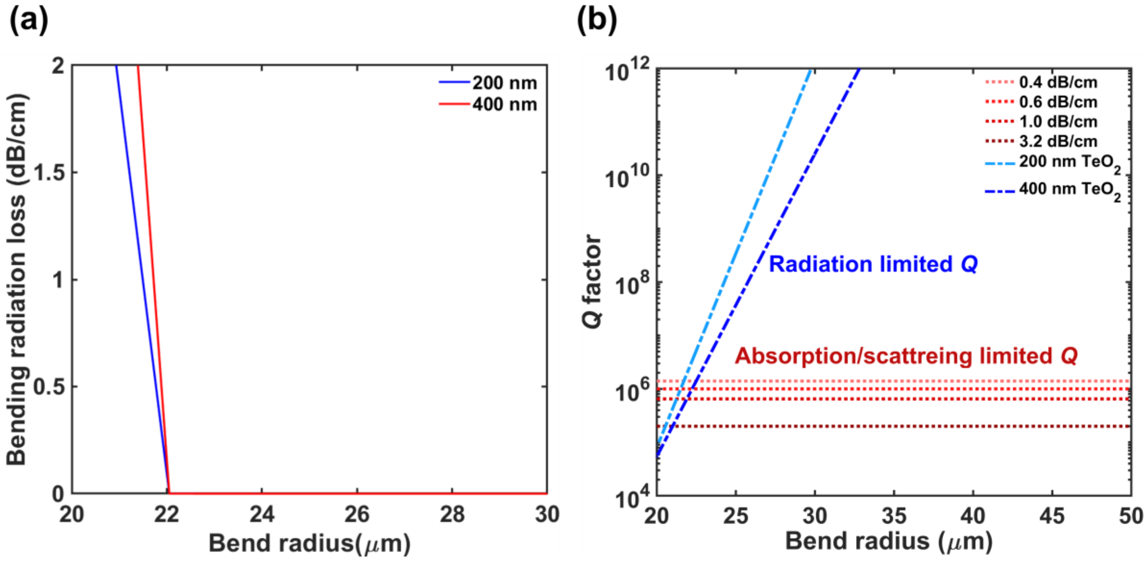

FIGURE 2.9: a) Minimum waveguide bend radius, defined as the radius below which radiation losses exceed 0.01 dB/cm for silicon bent waveguide coated with 200 nm and 400 nm tellurium oxide (TeO_2). b) Simulated radiation limited internal *Q* factors of microresonators coated in 200-, and 400-nm-thick TeO_2 considering the effects of bending radiation losses.

The results show the bending radiation loss of less than 0.01 dB/cm at bending radii > 22 μm. The results also indicate that thinner TeO_2 films can allow for lower bending (radiation) loss, but in general devices demonstrate the ability to be tightly bent on the scale necessary for densely integrated silicon photonic systems. A TeO_2 coating with a thickness of 200 nm is shown to maintain bending radiation limited intrinsic *Q* factors of > 10^{12} at bending radii of < 30 μm, while a 400-nm-thick coating is able to maintain high intrinsic *Q* factors at radii of 35 μm and above. The propagation loss of the waveguide (red dashed lines) is simulated using the quality factor of the SOI resonator.

The exponential attenuation coefficient of α is used to describe the magnitude of optical loss by giving the intensity (power per area) along the length of the waveguide as [1]:

$$I(z) = I_0 e^{-\alpha z} \tag{2.11}$$

where I_0 is the initial intensity (initial power per area) at $z = 0$. As indicated in equation 2.5, the loss is related to α, which is in dB/cm.

$$\text{loss}\left(\frac{\text{dB}}{\text{cm}}\right) = 4.3\alpha(\text{cm}^{-1}) \tag{2.12}$$

In this thesis, two methods have been used to characterize and measure the loss of the waveguides. One of the most accurate and the simplest method for waveguide loss measurement is measuring the transmitted total power for different lengths of the waveguides which is called a cut back measurement. The loss coefficient is measured from the slope of the transmission versus length curve by [1]:

$$\alpha = \frac{\ln(P_1/P_2)}{Z_2 - Z_1}\ for\ Z_2 > Z_1 \tag{2.13}$$

where P_1 and P_2 are the transmitted power for waveguides of two different lengths Z_1 and Z_2. In this method, the edge and face preparation of the waveguides are very important to be consistent for different lengths. Focused ion beam (FIB) has been heavily used in this thesis to polish the edge and face of the waveguide [1].

Another method that has been extensively used in this thesis, is the loss measurement of a resonator in terms of quality factor. To fabricate effective nonlinear and rare-earth-doped devices, it is essential to achieve low waveguide loss or, equivalently, high-quality (Q)

factor resonators. The radiation losses can be extracted by fitting the quality factor of a resonator which will be explained in section 2.3, where the theory of the microresonators will be discussed.

2.3 Microring and Microdisk Resonators

In this section, I describe the fundamental concepts of optical microring and microdisk resonators. A ring resonator consists of a looped waveguide where light can circulate either clockwise (CW) or counterclockwise (CCW). Ring resonators are typically evanescently coupled to a straight waveguide, also called bus waveguides, shown in figure 2.10, where r and k are the self and cross-coupling coefficients, respectively. The cross-coupling coefficient determines the fraction of light that is transferred from the bus waveguide to the ring or vice versa, while the self-coupling coefficient specifies the amount of light inside the bus waveguide or the ring [9,23].

The device is excited by the waveguide source mode with an amplitude I_{in} which is traveling in the left to the right (forward) direction. Two degenerate clockwise (CW) and counterclockwise (CCW) traveling modes are supported by resonator at resonance frequency ω_0. If losses in the coupling part can be neglected, then $|k|^2 + |r|^2 = 1$, where $|k|^2$ and $|r|^2$ are the power splitting ratios of the coupler. When the optical path length of the resonator is a whole number of wavelengths, then a resonance happens. It means when the round-trip phase shift is an integer multiple of 2π, the cavity is said to be on resonance and constructive interference occurs inside the cavity [9,23]. The figure 2.10 demonstrates a single bus waveguide coupling light to microring resonator and microdisk resonator.

When constructive interference accurses, resonators support multiple resonances, and the spectral response will show periodic peaks and dips. The resonance wavelength is provided by equation (2.14):

$$\lambda_{res} = \frac{n_{eff} L}{m} \tag{2.14}$$

where m is the resonance order and is an integer number, n_{eff} is the effective index and L is the circumference of the resonators, defined as L = 2πR, where R is the radius of the ring [9,23,24]. Also, a mode effective index (n_{eff}) is described for the traveling electromagnetic (EM) wave in the resonator as:

$$n_{\mathrm{eff}} = \frac{2\pi mc}{(L\omega_{res})} = \frac{m\lambda_{res}}{L} \tag{2.15}$$

where c is the speed of light, and ω_{res} and λ_{res} are the resonance frequency and wavelength, respectively. If β is the propagation constant of the travelling electromagnetic wave inside the resonator, the equation 2.15 can be written as:

$$n_{\mathrm{eff}} = \frac{\beta}{(\omega_0/c)} = \frac{\beta\lambda_0}{2\pi} \tag{2.16}$$

So, the interference or resonance can occur in resonators at a certain frequency and at the following condition [9,23,24]:

$$\beta L = 2\pi m \tag{2.17}$$

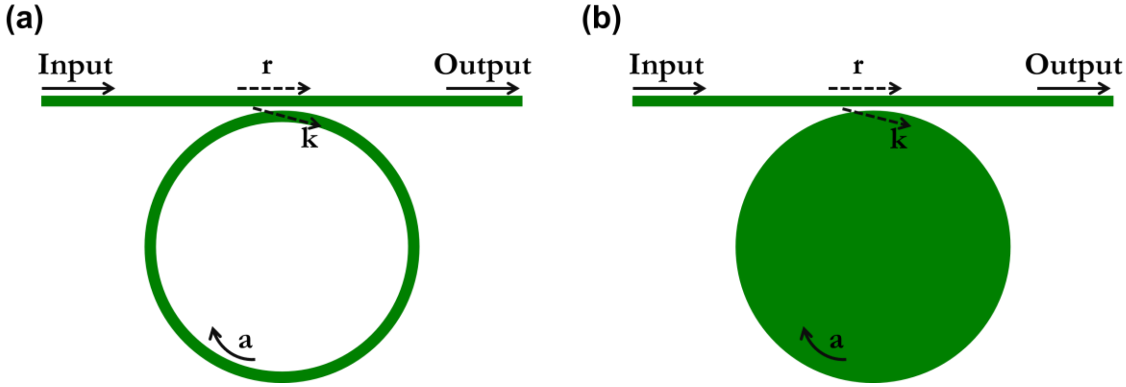

FIGURE 2.10: a) Schematic of waveguide-ring resonator coupling. b) Schematic of waveguide-disk resonator coupling.

The light couples into the resonator and travel around the cavity length of L, facing power attenuation or loss. The loss of the resonator happens due to the waveguide sidewall scattering and absorption which is defined with the loss coefficient of α. The intensity transmission of an all-pass ring resonator ($T = \frac{I_{out}}{I_{in}}$) can be described as [9,23,24]:

$$T = \frac{a^2 - 2racos\varphi + r^2}{1 - 2arcos\varphi + (ra)^2} \ and \ \varphi = \beta L \tag{2.18}$$

$$a = \exp(-\alpha L) \ cm^{-1} \tag{2.19}$$

Where L is the round-trip length, φ the single-pass phase shift, and β the propagation constant of the circulating mode. The parameter of a depends on the power attenuation coefficient of α and is defined as the single-pass amplitude transmission, consist of loss in the couplers and propagation loss in the ring [9,23,24].

2.3.1 Free Spectral Range (FSR)

As I mentioned in equation (2.14), multiple resonances will be supported by the resonators. For each m number there is an individual resonance, the distance between two adjacent peaks or dips is called the free-spectral-range or FSR. Therefore, by measuring the resonance spacing for two consecutive m numbers, the free-spectral range (FSR) of the resonator can calculated. This can be found as [9,23]:

$$FSR = \frac{2\pi v_g}{L} = \frac{\lambda^2}{n_g L} \tag{2.20}$$

v_g is the group velocity of the EM wave of $v_g = \frac{c}{n_g}$. From Equation (2.20) FSR is related to the mode volume of the resonator since a smaller mode volume means larger FSR. Many applications may require large FSR, which implies the use of small and compact resonators which is possible with high-contrast waveguides with strong confinement.

2.3.2 Quality Factor

Minimizing energy loss or leakage to have a long photon lifetime is a major goal in the design of resonators. However, due to resonators geometry and imperfections in the materials, the photon lifetime will be limited. The loss in resonators can be quantified by the cavity quality (Q) factor, which is typically limited to values on the order of 10^5 in standard 220-nm-high single-mode silicon microring resonators around 1550 nm. The physical meaning of the Q-factor is related to the ability of a ring resonator to store light energy as long as possible before losing it due to internal losses of the ring waveguide or due to the coupling to the bus waveguides. The quality factor (Q) of a resonator is defined as [23]:

$$Q = \frac{\pi n_g L\sqrt{ra}}{\lambda_{res}(1-ra)} = \frac{\lambda_{res}}{FWHM} \tag{2.21}$$

The full width at half maximum (FWHM) of the resonance spectrum for the all-pass configuration is provided by the following equation. This parameter indicates the distance between frequencies at which the transmission spectrum reaches half its maximum value.

$$FWHM = \frac{(1-ra)\lambda_{res}^2}{\pi n_g L\sqrt{ra}} \tag{2.22}$$

The propagation loss (α_{ring}) of the resonators is calculated by measuring the quality factor (Q) can be written as:

$$\alpha_{ring} = \frac{2\pi n_g}{Q\lambda_{res}} = \frac{\lambda_{res}}{QRFSR} \tag{2.23}$$

in this equation λ_{res} is the wavelength of light, FSR is the free spectral range, Q is the quality factor, n_g is the group index and R is the radius of the resonator.

2.3.3 Mode Volume

Mode volume is another important parameter of the resonators. The mode volume and the energy localization of the resonator depends on the radial and vertical confinements of a mode, and resonator traveling length. The thickness of the resonator affects the vertical mode confinement. However, the radial mode confinement is controlled by the resonator's radius. By decreasing the resonator's radius, the mode will be more localized in the radial direction and the mode will be pushed to the edge of the resonators. So, lower Q factor for smaller radius will be expected due to more energy leakage to the outside of the resonator as well as more sidewall interaction [23].

Different numbers of radial peaks can be supported by a microdisk resonator, whereas a microring is typically designed to support one radial mode order. Energy leakage happens to the outside of the microdisk structure, which reduce the Q factor of the resonator. Microdisks have more modes supported but tend to have lower loss due to less sidewall interaction. In contrast, microring resonators are designed to be single-mode waveguides and single-mode waveguide happens through the outer sidewalls of the ring. As shown in equation (2.15), the mode effective index depends on the radius. The mode effective index is not a constant quantity, because the radius depends on the traveling length of the modal field ($L(r) = 2\pi R$). As a result, the effective index is inversely related to the radius. By increasing the radius of the microdisk, the mode will be expanded further inside the microdisk and less outside. consequently, the effective index of the mode will be larger and closer to the refractive index of the disk core material (e.g., silicon) [23].

2.4 Rare Earth Ions

Rare earth elements are known as the Lanthanides and are categorized by a group of 15 elements. The rare earth elements are highly stable when they are in their triply ionized form. The trivalent (3+) ionization of rare earth elements removes 6s and 5d electrons, leaving an electronic structure identical to xenon plus a certain number (1-14) of 4f electrons, i.e. $1s^2$, $2s^2$, $2p^6$, $3s^2$, $3p^6$, $3d^{10}$, $4s^2$, $4p^6$, $4d^{10}$, $4f^N$, $5s^2$, $5p^6$ and $6s^0$, where N = 1,..., 14 [11,12]. Lanthanide elements in their triply ionized form are mentioned to as rare earth ions and are almost insensitive to the host material. The rare earth elements are highlighted in figure 2.11.

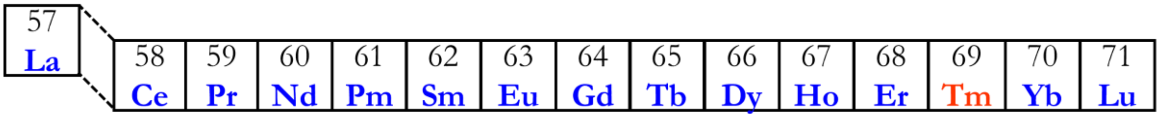

FIGURE 2.11. Lanthanide series of the elements.

The $4f^N$ structure of a rare earth ion is made of a number of electronic states enable to be excited to a higher lying orbital, such as 5g, or it can be excited within the $4f^N$ set of levels. By solving the time dependent Schrödinger equation, the spread of $4f^N$ energy levels can be found and their weak interactions with electrons from other ions allows a Hamiltonian equation for a particular rare earth ion [13].

Transitions between the energy level of rare earth elements are accrued as radiative and non-radiative transitions. Radiative transitions consist of the absorption and emission of photons that are defined as the quanta of electromagnetic radiation, while non-radiative transitions consist of the absorption and emission of phonons that are defined quanta of vibrational energy in the host material. Non-radiative decay will happen quickly and effectively when electronic states are close enough to be linked by emission or absorption of one or two phonons, which causes the thermalisation of energy manifolds.

2.5 Thulium (Tm^{3+})

Thulium has 12 electrons in its 4f shell and is the thirteenth lanthanide element. Figure 2.12 shows the energy level diagram of the Tm^{3+} ion. The first excited state of Tm^{3+} is $^3F_4$ manifold and the ground state is represented as $^3H_6$. The $^3F_4 \rightarrow {}^3H_6$ transition delivers very wide emission band spanning from 1.6 µm to 2.0 µm due to the strong coupling of the rare earth ion to the lattice [25]. The $^3F_4$ manifold can be excited through the decay of higher energy manifolds such as the $^3H_5$ and $^3H_4$ manifolds or can be pumped directly around 1580 to 1690 nm [26]. Due to the close energy spacing between the $^3H_5$ and $^3F_4$ manifolds, approximately most of the excited state ions in the $^3H_5$ manifold decay nonradiatively to the $^3F_4$ manifold. Thus, $^3F_4$ manifold can be pumped indirectly with efficient and fairly cheap light sources around 1060 nm. The third excited state of Tm^{3+} is defined as $^3H_4$ manifold. When ions are excited to the $^3H_4$ manifold they may relax to the next lowest energy state, the $^3H_5$ manifold, which may occur radiatively and nonradiatively with respect to the the host material and its lifetime. It may also directly emit to the ground state of $^3H_6$.

Recently, there has been a considerable interest to study Tm^{3+} doped materials, due to the attractive emissions in the visible and infrared regions [27, 28]. Thulium doped glass, in particular, exhibits a broad emission band from 1600 to over 2000 nm. This wide band emission attracts interests for broadband optical amplifiers for wavelength division multiplexed systems, tunable lasing in the ‘eye safe’ wavelength domain [29] and make them as a good candidate for infrared window applications including medical devices and biosensors [30].

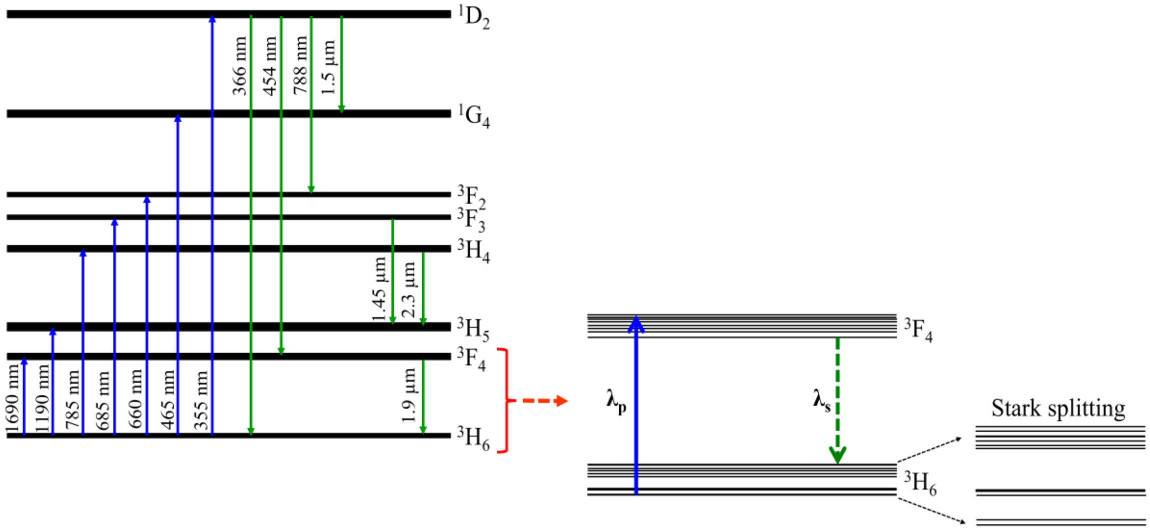

FIGURE 2.12: Simplified scheme of energy levels of Tm^{3+}

Thulium ions are embedded in glass hosts in a trivalent state which causes further splitting of the rare-earth energy levels in the 4f shell. This splitting occurs due to the ion-lattice interactions caused by the crystal field of the host. This additional splitting that the orbitals undergo is called Stark splitting and results in different Stark components of the parent manifolds. These sharp line shapes result in efficient emission that is useful for applications such as lasing [31,32]. Thulium-based optical amplifiers operate through the process of ion energy transitions within the 4f shell. The transitions are usually the result of ion interaction with an external stimulus, such as a photon. Several transitions relevant to thulium-doped amplifier and laser are shown in figure 2.12. In order to populate $^3F_4$ level, the pump light with the wavelength of 1580 to 1690 nm are typically used for the amplifiers and lasers operating at TDFA window based on $^3F_4 \rightarrow {}^3H_6$ transition.

Figure 2.13 depicts the three optical processes that can occur in a system with an excited and ground energy state of stimulated absorption, spontaneous emission, and stimulated emission. Although the energy states can be of many different forms, we limit our discussion here to the consideration of an electron of an atom transitioning between the two distinct electron configuration energy levels. The most general transitions that occur from this interaction are excitation of the ion to a higher energy state by absorbing the incident photon which is known as stimulated absorption or an already excited ion emitting a photon of equal phase and frequency to the incident photon known as stimulated emission. There is also the possibility that an excited ion will fall back down to the ground state and emit a photon of random phase and direction without external stimulus is known as spontaneous emission. These three transitions are depicted in figure 2.13. External stimuli are typically provided, or pumped, optically into the system using an external laser source with a specific wavelength to induce stimulated absorption and excite the relaxed ions. Once stimulated emission dominates, most of the excited energy states are filled with ions and ground states are filled with holes. This condition is known as population inversion and is essential for enabling gain within an amplifier.

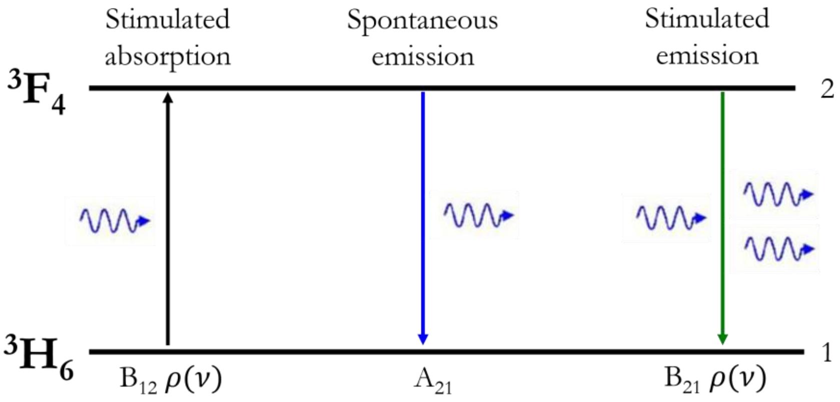

FIGURE 2.13: The simplified two-level energy diagram showing the processes and transition rates of stimulated absorption, spontaneous emission, and stimulated emission.

The amount of absorbed or emitted optical power is equal to the product of the associated cross section of the ion and the incident optical intensity:

$$P_{a/e}(\lambda) = \sigma_{(a/e)}(\lambda)\mathrm{I}(\lambda) \tag{2.24}$$

σ_a and σ_e are the absorption and emission cross sections that are the probabilities in which stimulated absorption or emission can occur between two energy states of an ion, respectively. $P_{a/e}(\lambda)$ is the absorbed or emitted optical power and $I(\lambda)$ is the optical intensity. The Einstein coefficients [33,34] describe the mathematical relationship between all three processes for an idealized, non-degenerate two-level energy system. The change in population of the first excited state in the two-level system due to absorption and emission processes is defined as:

$$(\frac{dN_2}{dt})_a = B_{12}\rho(\nu)N_1 \tag{2.25}$$

$$(\frac{dN_2}{dt})_e = -(A_{21} + B_{21}\rho(\nu))N_2 \tag{2.26}$$

N_1 and N_2 are lower and upper states populations, respectively, $\rho(\nu)$ is the photon flux density (number of photons per unit frequency bandwidth per unit volume) and B_{12}, A_{21} and B_{21} are the Einstein coefficients that describe the strength of the stimulated absorption, spontaneous emission, and stimulated emission transition rates, respectively. For the case of rare-earth ions, these two states are made up of a comb of Stark-split sub-levels that are populated to various extents based on the thermal distribution. The population characteristics can be affected by thermal situation. The gain parameter of an optical medium and engineering the host material for active laser devices can be calculated by knowing the absorption and emission cross-sections. In this case, the thermal Boltzmann distribution is considered in McCumber theory [35] for a more accurate description of the cross sections. Under the condition that thermal equilibrium is reached within a multistate manifold in a time shorter than the radiative lifetime of the manifold, the absorption and emission cross section can be related such that:

$$\sigma_e(\lambda) = \sigma_a(\lambda). \exp\left(\frac{\epsilon - h\nu}{kT}\right) \tag{2.27}$$

$\boldsymbol{\epsilon}$ is the mean transition energy between the manifolds, h is Planck's constant, ν is the frequency corresponding to the transition energy, k is Boltzmann's constant, and T is the temperature. When the states are degenerate (stark-split manifolds), and there are sub energy levels in the ground states and excited states, the relation between the emission and absorption cross sections are described as:

$$\sigma_e(\lambda) = \sigma_a(\lambda). \frac{Z_0}{Z_1} \exp\left(\frac{\epsilon - E(\lambda)}{kT}\right) \tag{2.28}$$

where $\boldsymbol{\sigma_a}$ and $\boldsymbol{\sigma_e}$ are the absorption and emission cross sections, respectively, and $\boldsymbol{\frac{Z_0}{Z_1}}$ is energy partition function in term of stark splitting and thermal distribution of the excited and ground states populations, *E(λ)* is the transition energy for the wavelength of *λ*. An electron in an excited state eventually experiences a decay event to the ground state, either through a radiative or non-radiative thermal process, that can be presented by the intensity of spontaneous emission from the excited state. The excited state lifetime (τ) refers to the average time in which a large collection of electrons experience decay after being excited. From the Einstein relations' description of a medium at thermal equilibrium the spontaneous radiative lifetime (τ_{Rad}), is related to the emission cross (σ_{e}) section through the Füchtbauer-Ladenburg equation [36], neglecting non-radiative decay mechanisms as follows;

$$\frac{1}{\tau_{Rad}} = 8\pi n^2 c \int \frac{\sigma_e(\lambda)}{\lambda^4} d\lambda \tag{2.29}$$

where n is the refractive index of the medium, c is the speed of light in a vacuum and λ is the wavelength of light, $\boldsymbol{\tau_{Rad}}$ is the radiative lifetime, $\boldsymbol{\sigma_e}$ is the emission cross section. The spontaneous emitted intensity is plotted versus time to achieve a luminescence decay curve. The luminescent lifetime is the sum of radiative decay results in the spontaneous emission of a photon, and non-radiative decay represents the energy that is transferred to phonons, vibration of crystal, or glass host materials. The Luminescence lifetime ($\boldsymbol{\tau}$) is written as:

$$\frac{1}{\tau} = \frac{1}{\tau_{Rad}} + \frac{1}{\tau_{nRad}} \tag{2.30}$$

where $\boldsymbol{\tau_{Rad}}$ is the radiative lifetime and $\boldsymbol{\tau_{nRad}}$ is the non-radiative lifetime. When the thulium (Tm^{3+}) ion concentration is relatively high, the average distance between neighboring ions is reduced to the point that it results in significant energy transfer between ions as shown in figure 2.14, via cross relaxation or energy transfer upconversion.

In cross relaxation, the energy from donor ion (excited state) is transferred to a near acceptor ion (ground state), supporting the acceptor ion to a higher energy state, although demoting the donor ion to a lower energy state. This process can result in loss and energy degeneracy at an impurity lead to a reduction in the efficiency of the transition which is the detrimental effect of cross relaxation. It is necessary that both donor and acceptor ions have two energy levels of almost the same energy gap or having equally spaced energy levels. Figure 2.14a shows the cross relaxation process where two excited ions interact, with energy from donor ions being transferred to the accepter, promoting the accepter to the higher energy state [37].

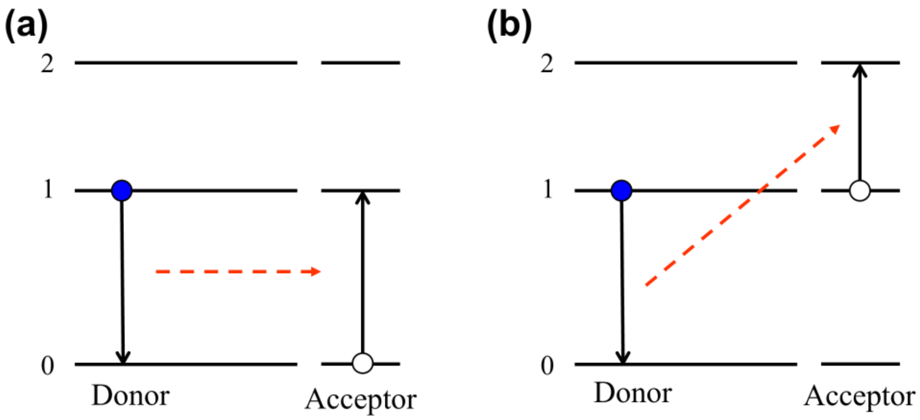

FIGURE 2.14: a) Cross relaxation process in Tm^{3+} between the $^3H_4$ and $^3H_6$ manifolds. b) energy transfer upconversion.

Figure 2.14b shows the energy transfer upconversion process (ETU) that is a process that both the donor and acceptor ions are in an excited state. A donor ion in an excited state may transfer its energy to a close acceptor ion, causing the acceptor ion to a higher energy state. Thus, the acceptor can relax radiatively or non-radiatively directly to the ground state or to lower levels which causes fluorescence emission at an energy greater than the incident light.

2.5.1 Gain in a Thulium-Based Energy System

Optical amplification is based on the rate equations of the electronic excitations considering the transition properties of the ions as they interact with various external stimuli and how the atomic population changes with respect to time.

The two-level energy system of Tm^{3+} is shown in figure 2.13. $^3H_6$ is considered as the ground state and $^3F_4$ as excited state. A one-dimensional case considered in which light propagates in the *z* direction along the length of the amplifier. The light field intensities are derived from the light field powers such that:

$$I(z) = \frac{P(z).\Gamma}{A_{eff}} \tag{2.31}$$

Γ is the normalized mode overlap factor of the active region, and A_{eff} is the effective cross-sectional area of the distribution of thulium ions. The pump and signal with intensities I_p and I_s, respectively, travel through the waveguide and interact with the ions. The rate equations of the thulium-doped waveguide amplifier at any point along the waveguide length when the $^3F_4$ energy level is directly excited are [38-40]:

$$\frac{dN_2(z,t)}{dt} = w_{p12}N_1 - w_{p21}N_2 - \frac{N_2}{\tau_{21}} - w_{s21}N_2 + w_{s12}N_1 \tag{2.32}$$

$$\frac{dN_1(z,t)}{dt} = -w_{p12}N_1 + w_{p21}N_2 + \frac{N_2}{\tau_2} + w_{s21}N_2 - w_{s12}N_1 = -\frac{dN_2(z,t)}{dt} \tag{2.33}$$

$$N_1 = N_T - N_2 \tag{2.34}$$

where τ_{21} is the spontaneous lifetime of $^3F_4$ level, N_1 and N_2 are the population densities of the active thulium ions for $^3H_6$ and $^3F_4$ levels respectively, N_T is the Tm^{3+} concentration that is constant. When w_{p12} is the pumping rate from $^3H_6$ to $^3F_4$ and w_{p21} represents the de-excitation rate of the $^3F_4$ level, w_{s21} is the stimulated emission rate from $^3F_4$ to $^3H_6$, and w_{s12} is the stimulated absorption rate from $^3H_6$ to $^3F_4$. The expressions of w_{p12}, w_{p21}, w_{s21} and w_{s12} are given as [40]:

$$w_{p12} = \frac{\lambda_p \Gamma_p}{hcA_{eff}} \sigma_a(\lambda_p)[P_p^+(z) + P_p^-(z)] \tag{2.35}$$

$$w_{p21} = \frac{\lambda_p \Gamma_p}{hcA_{eff}} \sigma_e(\lambda_p)[P_p^+(z) + P_p^-(z)] \tag{2.36}$$

$$w_{s12} = \frac{\lambda_s \Gamma_s}{hcA_{eff}} \sigma_a(\lambda_s)[p_s(z) + ASE_f(z) + ASE_b(z)] \tag{2.37}$$

$$w_{s21} = \frac{\lambda_s \Gamma_s}{hcA_{eff}} \sigma_e(\lambda_s)[p_s(z) + ASE_f(z) + ASE_b(z)] \tag{2.38}$$

where *h* is the Planck constant; c is the light speed in vacuum, λ_p and λ_s are the wavelengths of the pump and the signal in vacuum, respectively; Γ_p and Γ_s are the overlapping vector for the pump and the signal, respectively; A_{eff} is the effective cross-sectional area of the distribution of thulium ions. $\sigma_a(\lambda_p)$ and $\sigma_a(\lambda_s)$ are the absorption cross-sections of the pump and the signal, respectively; $\sigma_e(\lambda_p)$ and $\sigma_e(\lambda_s)$ are the emission cross-sections of the pump light and the signal light, respectively. $P_p^{\pm}(z)$ and $P_s(z)$ are the pump (corresponding to forward and backward) and the signal power at position *z*; $ASE_f(z)$ and $ASE_b(z)$ are the forward and backward amplified spontaneous emission power at position *z*. The distribution of the pump power and signal power along the waveguide length is expressed by [40]:

$$\frac{dP_p^{\pm}}{dz} = \pm p_p^{\pm}(z)[\Gamma_p\left(\sigma_e(\lambda_p)N_2(z) - \sigma_a(\lambda_p)N_1(z)\right) - \alpha_{p1}] \tag{2.39}$$

$$\frac{dp_s}{dz} = p_s(z)[\Gamma_s\left(\sigma_e(\lambda_s)N_2(z) - \sigma_a(\lambda_s)N_1(z)\right) - \alpha_s] \tag{2.40}$$

The *ASE* power along the waveguide length is expresses by [30]:

$$\frac{dASE_f}{dz} = ASE_f(z)\left[\Gamma_s\left(\sigma_e(\lambda_s)N_2(z) - \sigma_a(\lambda_s)N_1(z)\right) - \alpha_s\right] + 2\sigma_e(\lambda_s)N_2(z)\frac{hc^2}{\lambda_s^3}\Delta\lambda \tag{2.41}$$

$$\frac{dASE_b}{dz} = ASE_b(z)\big[\Gamma_s\big(\sigma_e(\lambda_s)N_2(z) - \sigma_a(\lambda_s)N_1(z)\big) - \alpha_s\big] + 2\sigma_e(\lambda_s)N_2(z)\frac{hc^2}{\lambda_s^3}\Delta\lambda \tag{2.42}$$

where α_{p1} and α_s are the intrinsic absorption at the 1620 nm pump and signal wavelength for the thulium-doped waveguide respectively, $\Delta\lambda$ is the bandwidth of the amplifier spontaneous emission (*ASE*) at around 2 μm. Under steady state conditions, the time derivatives are all equated to zero:

$$\frac{dN_1}{dt} = -\frac{dN_2}{dt} = 0 \tag{2.43}$$

A time-independent equation is derived that determines the upper state population at a given position along the amplifier:

$$N_2(z) = \frac{(\tau w_{p12} + \tau w_{s12})}{(1 + \tau w_{p12} + \tau w_{s12} + \tau w_{p21} + \tau w_{s21})} N_T \tag{2.44}$$

The propagation equations describe the change in light field intensity of a given source as the beam travels down the length of the amplifier. For this system, we evaluate the propagation equations as:

$$\frac{dI_{p/s}(z)}{dz} = (N_2\sigma_{p/s}^e - N_1\sigma_{p/s}^a)I_{p/s}(z) \tag{2.45}$$

Two conditions should be satisfied in order to achieve the positive gain form the signal propagation and the population inversion if $N_2 > N_1$ or $N_2/N_1 > 0.5$ which cause $\frac{dI_s}{dz} > 0$ and the pump intensity is greater than the threshold pump intensity. The threshold pump intensity is [40]:

$$I_p \geq I_{th,p} = \frac{h\nu_p}{\tau_{21}} \frac{1}{\sigma_p^a(\sigma_s^e/\sigma_s^a) - \sigma_p^e} \tag{2.46}$$

The absorption loss due to the thulium ions in the doped waveguide can be expressed as:

$$\alpha_{Tm}(\lambda) = \sigma^a(\lambda). N_T. \Gamma(\lambda). 10loge \tag{2.47}$$

$\Gamma(\lambda)$ is the calculated confinement factor of the active layer, and N_T is the ground state population density. After calculation of the above rate equations and propagation equations, the optical performance can be determined using the internal gain (dB):

$$g(\lambda) = 10\log_{10}[I(z = L)/I(z = 0)] \tag{2.48}$$

So, the total internal net gain is calculated by:

$$G(\lambda) = g(\lambda) - \alpha_{total}(\lambda) \tag{2.49}$$

The internal net gain per unit length (dB/cm):

$$\gamma(\lambda) = \frac{G(\lambda)}{L}, (dB/cm) \tag{2.50}$$

$z=0$ is the input and $z=L$ is the output of the waveguide facet and $\alpha_{total}(\lambda)$ is the total absorption coefficient or background loss and L is the amplifier length.

2.5.2 Quasi-Three-Level Lasing in a Thulium-Based Energy System

A simple two-level system with the lower energy state as the ground state ia a good absorber. Lasers are commonly classified into three-level or four-level lasers. Laser systems require a gain medium to be pumped to provide energy to a field that propagates through it. A common atomic-three-level structure is shown in figure 2.15, with the level of energy E_0 being the ground state.

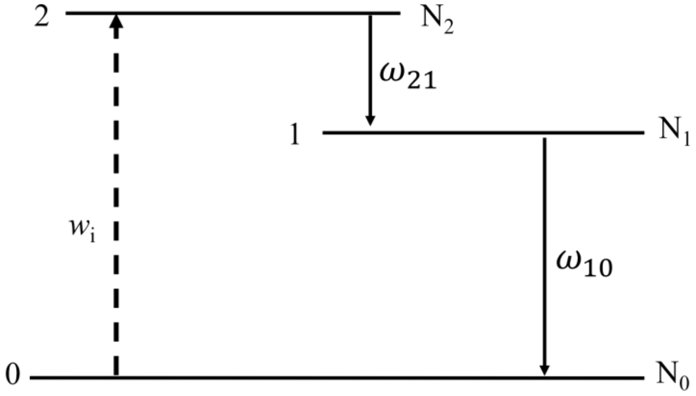

FIGURE 2.15: Three-level laser medium

The pump energy is presented to the system via the 0 to 2 transitions with the rate equations governing population densities as indicated [34,41]:

$$\frac{dN_2}{dt} = -\omega_{21}N_2 - w_i(N_2 - N_1) + R_2 \tag{2.51}$$

$$\frac{dN_1}{dt} = -\omega_{10}N_1 + \omega_{21}N_2 + w_i(N_2 - N_1) + R_1 \tag{2.52}$$

$$N_T = N_0 + N_1 + N_2 \tag{2.53}$$

where R_1 and R_2 are the pumping intensity, ω_{ij} is the decay rate per atom for level i to j, and w_i is the probability per unit time that an atom in level 2 will undergo an induced transition to level 1. Gain will occur with a population inversion ($N_2 > N_1$) exists in steady state. Net production of photons will happen when the stimulated emission exceed stimulated absorption. The laser oscillation starts when the upper laser level obtains by pumping, a population density equal to the threshold value N_t. Once the pumping is increased beyond the threshold point $N_2 – N_1 = N_t$, the laser will break into oscillation and emit power. At threshold, the population inversion is calculated as [34,41]:

$$N_t = N_2 - N_1 = \frac{R}{w_i + \omega_{21}}, R = R_2[1 - \frac{\omega_{21}}{\omega_{10}}(1 + \frac{R_1}{R_2})] \tag{2.54}$$

The total power generated by stimulated emission is:

$$P_e = (N_tV)w_ih\nu \tag{2.55}$$

where V is the volume of the oscillating mode. In an ideal laser system, $\tau_{spont} = \frac{1}{\omega_{21}}$, so the power going into spontaneous emission at threshold is [34,41]:

$$P_s = (N_t V)\omega_{21} hv \tag{2.56}$$

$$P_e = P_s(\frac{R}{R_t} - 1) \tag{2.57}$$

2.5.3 Conclusion

This chapter presented a comprehensive theoretical examination of the basic building blocks of photonics integrated circuits (PICs), including waveguides and resonators, as well as a description of their key performance characteristics. The spectroscopic properties of rare earth elements have been presented in order to gain an understanding of the behavior of rare-earth-doped waveguide amplifiers and lasers. The science behind thulium doped materials as a gain media for integrated optical devices have been demonstrated in this chapter.

Bibliography

[1] R. G. Hunsperger, “Integrated optics: theory and technology,” Sixth Edition, Springer Media, (2009).

[2] H. E. Kogelnik, “An introduction to integrated optics,” *IEEE Trans. Microw. Theory Techn.* **23**(1), 2–16 (1975).

[3] R. Soref, “The past, present, and future of silicon photonics,” *IEEE J. Sel. Top. Quantum Electron.* **12**(6), 1678–1687 (2006).

[4] D. Thomson D, A. Zilkie, J. E. Bowers, T. Komljenovic, G. T. Reed, L. Vivien, D. Marris-Morini, E. Cassan, L. Virot, J. M. Fédéli, J. M. Hartmann, J. H. Schmid, D. X. Xu, F. Boeuf, P. O’Brien, G. Z. Mashanovich, and M. Nedeljkovic, “Roadmap on silicon photonics,” *J. Opt.* **18**(7), 073003 (2016).

[5] M. Streshinsky, R. Ding, Y. Liu, A. Novack, C. Galland, A. J. Lim, P. G. Lo, T. Baehr-Jones, and M. Hochberg, “The road to affordable, large-scale silicon photonics,” *Opt. Photonics News* **24**(9), 32–39 (2013).

[6] D. J. Blumenthal, R. Heideman, D. Geuzebroek, A. Leinse, and C. Roeloffzen, “Silicon nitride in silicon photonics,” *Proc. IEEE* **106**(12), 2209–2231 (2018).

[7] E. A. J. Marcatili, “Dielectric rectangular waveguide and directional coupler for integrated optics,” *Bell Syst. Tech. J.* **48**, 2071—2102 (1969).

[8] C. Naraine “Fabrication, design and characterization of silicon-on-insulator waveguide amplifiers coated in erbium-doped tellurium oxide,” M.A.Sc. dissertation, McMaster University, Canada, (2020).

[9] D. Hagan “Performance considerations in high-speed TDFA-band silicon photonic micro-ring resonator modulators,” PhD dissertation McMaster University, Canada, (2019).

[10] N. K. Uzunoglu and J. G. Fikioris, “Scattering from an inhomogeneity inside a dielectric-slab waveguide,” *J. Opt. Soc. Am.* 72, 628-637 (1982).

[11] D. Allan Simpson, “Spectroscopy of the thulium doped silica glass,” PhD dissertation, BSc. (Hons) Victoria University, (2008).

[12] S. Sudo, “Optical fiber amplifiers: materials, devices, and applications,” Artech House, Inc., Boston, (1997).

[13] W. J. Miniscalco, “Optical and electronic properties of rare earth ions in glasses,” *Rare Earth Doped Fiber Lasers and Amplifiers*, 2nd Edition (2001).

[14] Synopsis RSoft Photonic Device Tools: https://www.synopsys.com/photonic-solutions/rsoft-photonic-device-tools.html

[15] A. Gondarenko, J. S. Levy, and M. Lipson, “High confinement micron-scale silicon nitride high Q ring resonator,” *Opt. Express* **17**(14), 11366–11370 (2009).

[16] E. S. Hosseini, S. Yegnanarayanan, A. H. Atabaki, M. Soltani, and A. Adibi, “High quality planar silicon nitride microdisk resonators for integrated photonics in the visible wavelength range,” *Opt. Express* **17**(17), 14543–14551 (2009).

[17] J. F. Bauters, M. J. R. Heck, D. John, D. Dai, M.-C. Tien, J. S. Barton, A. Leinse, R. G. Heideman, D. J. Blumenthal, and J. E. Bowers, “Ultra-low-loss high-aspect-ratio Si_3N_4 waveguides,” *Opt. Express* **19**(4), 3163– 3174 (2011).

[18] J. F. Bauters, M. J. R. Heck, D. D. John, J. S. Barton, C. M. Bruinink, A. Leinse, R. G. Heideman, D. J. Blumenthal, and J. E. Bowers, “Planar waveguides with less than 0.1

dB/m propagation loss fabricated with wafer bonding," *Opt. Express* **19**(24), 24090–24101 (2011).

[19] C. G. H. Roeloffzen, M. Hoekman, E. J. Klein, L. S. Wevers, R. Bernardus Timens, D. Marchenko, D. Geskus, R. Dekker, A. Alippi, R. Grootjans, A. van Rees, R. M. Oldenbeuving, J. P. Epping, R. G. Heideman, K. Wörhoff, A. Leinse, D. Geuzebroek, E. Schreuder, P. W. L. van Dijk, I. Visscher, C. Taddei, Y. Fan, C. Taballione, Y. Liu, D. Marpaung, L. Zhuang, M. Benelajla, and K.-J. Boller, "Low-loss Si_3N_4TriPleX optical waveguides: Technology and applications overview," *IEEE J. Sel. Top. Quantum Electron.* **24**(4), 4400321 (2018).

[20] K. Wörhoff, R. G. Heideman, A. Leinse, and M. Hoekman, "TriPleX: A versatile dielectric photonic platform," *Adv. Opt. Technol.* **4**(2), 189–207 (2015).

[21] H. C. Frankis, K. Miarabbas Kiani, D. B. Bonneville, C. Zhang, S. Norris, R. Mateman, A. Leinse, N. D. Bassim, A. P. Knights, and J. D. B. Bradley, "Low-loss TeO_2-coated Si_3N_4 waveguides for application in photonic integrated circuits," *Opt. Express* **27**, 12529-12540 (2019).

[22] J. H. Schmid, A. Delâge, B. Lamontagne, J. Lapointe, S. Janz, P. Cheben, A. Densmore, P. Waldron, D.-X. Xu, and K. P. Yap, "Interference effect in scattering loss of high-index- contrast planar waveguides caused by boundary reflections," *Opt. Lett.* **33**(13), 1479-–1481 (2008).

[23] M. Soltani, “Novel integrated silicon nanophotonic structures using ultra-high *Q* resonators,” PhD dissertation, Electrical and Computer Engineering, Georgia Institute of Technology (2009).

[24] W. Bogaerts, P. De Heyn, T. Van Vaerenbergh, K. DeVos, S. Kumar Selvaraja, T. Claes, P. Dumon, P. Bienstman, D. Van Thourhout, and R. Baets, “Silicon microring resonators,” *Laser Photonics Rev.* **6**(1), 47–73 (2012).

[25] A. Tropper, R. Smart, I. Perry, D. Hanna, J. Lincoln, and B. Brocklesby “Thulium-doped silica fiber lasers,” *SPIE Fibre Laser Sources and Amplifiers* **1373**, 152 (1990).

[26] G. Frith, D. G. Lancaster, and S. D. Jackson “85 W Tm^{3+}-doped silica fibre laser,” *Electron. Lett.* **41**(12), 687 (2005).

[27] Q. Nie, X. Li, S. Dai, T. Xu, Z. Jin, and X. Zhang, “Energy transfer and upconversion luminescence in Tm^{3+}/Yb^{3+} co-doped lanthanum-zinc-lead tellurite glasses,” *J. of Luminescence* **128**, 135-141, (2008).

[28] L. Xu, B. Song, S. Xiao, and J. LU, “Up-conversion luminescence of Tm^{3+} /Yb^{3+} co-doped oxy-fluoride glasses,” *J. of Rare Earths* **28**, 194-197, (2010).

[29] A. Godard, “Infrared 2-12 pm solid-state laser sources: a review,” *Comptes Rendus Physique* **8**, 1100-1128, (2007).

[30] W. E. K. Gibbs, D. J. Booth, and V. K. Bogdanov, “Population dynamics of the $^3F_4$ and $^3H_4$ levels in highly-doped Tm^{3+}: ZBLAN glasses,” *J. of Non-Crystalline Solids* **353**, 1-5, (2007).

[31] M. J. F. Digonnet, “Rare-earth-doped fiber lasers and amplifiers,” Second edition, Marcel Dekker Inc., (2001).

[32] H. Steinkemper, S. Fischer, M. Hermle, and J. C. Goldschmidt, “Stark level analysis of the spectral line shape of electronic transitions in rare earth ions embedded in host crystals,” *New J. Phys.* **15** (2013).

[33] R. C. Hilborn, “Einstein coefficients, cross sections, f values, dipole moments, and all that,” *Am. J. Phys.* **50**(11), 982–986 (1982).

[34] A. Yariv and P. Yeh, “Optical electronics in modern communications” (Oxford University, 2006).

[35] D. E. McCumber, “Einstein relations connecting broadband emission and absorption spectra,” *Physical Review* **136**, A954, (1964).

[36] P W. Milonni and J. H. Eberly, “Lasers” *Wiley*, (1998).

[37] M. A. Taher, “Spectroscopy, modeling and investigation of thulium doped tellurite glass,” PhD dissertation, Swansea University (2011).

[38] S. D. Jackson and T. A. King, “Theoretical modeling of Tm-doped silica fiber lasers,” *J. of Lightwave Technology* **17**(5), 948-956 (1999).

[39] M. Gorjan, T. North, and M. Rochette, “Model of the amplified spontaneous emission generation in thulium-doped silica fibers,” *J. Opt. Soc. Am. B.* **29**(10) 2886-2890 (2012).

[40] M. A. Khamis and K. Ennser, "Theoretical model of a thulium-doped fiber amplifier pumped at 1570 nm and 793 nm in the presence of cross relaxation," *J. of Lightwave Technology* **34**(24) 5675-5681 (2016).

[41] F. L Pedrotti, L. M. Pedrotti, L. S. Pedrotti, "Introduction to optics" *Springer*, (2006).

Chapter 3

Thulium-Doped Tellurium Oxide Waveguide Amplifiers on Silicon Nitride Chips

Preface

The following chapter presents the design, fabrication, and characterization of thulium-doped tellurium oxide ($TeO_2:Tm^{3+}$) silicon nitride (Si_3N_4) waveguide amplifiers. Efficient amplifiers are the key components in silicon photonics (SiP) telecommunication infrastructure to boost transmitted and/or received signals. Tm-doped amplifiers enable the broadest gain spectrum of all rare-Earth doped amplifiers, high gain, low noise figure performance, and faster transmission speed. Integrated on-chip Tm-doped amplifiers can be fabricated using low-cost and high-volume methods combine with different functionalities on a single chip. The on-chip amplifiers presented here are based on thulium-doped tellurite-glass-coated silicon nitride waveguides as a gain medium.

Tellurium oxide (TeO_2) is a highly promising material for active monolithically integrated optical devices due to its high rare earth solubilities, low quenching, large emission bandwidth as well as high gain. The wide transparency window and low propagation loss of Si_3N_4, make it a significant complementary silicon-compatible platform for on-chip amplifiers. The thulium-doped tellurium oxide (TeO_2:Tm^{3+}) is deposited onto foundry-fabricated Si_3N_4 chips via reactive radio frequency (RF) co-sputtering, which is a room-temperature, straightforward and monolithic approach, in the Centre for Emerging Device Technologies (CEDT) at McMaster University. The passive transmission properties and amplifiers properties were characterized on 1.0-µm-wide TeO_2:Tm^{3+} Si_3N_4 waveguides with lengths of 2.2 and 6.7 cm with thulium concentration of 2×10^{20} cm^{-3}. These results show that TeO_2:Tm^{3+}-coated Si_3N_4 waveguides are highly promising for compact and high gain optical amplifiers on silicon photonic platforms.

An introduction and motivation for on-chip integrated thulium amplifiers on the silicon nitride platform are given in section 3.1. Section 3.2 describes the waveguide amplifiers' design, structure, and fabrication. The optical properties of the amplifiers structures have been investigated using a finite element bent eigenmode solver. In section 3.3, the passive and active optical transmission properties of TeO_2:Tm^{3+}-Si_3N_4 waveguides and devices are characterized, including their propagation losses and gain, using a fiber-chip coupling setup. Gain measurements were carried out in straight and s-bend waveguides with lengths of 2.2 and 6.7 cm, respectively, on a 2.2-cm-long chip, showing internal net gain up to 7.8 dB at 1870 nm corresponding to 1.1 dB/cm. In section 3.4, lower $TeO_2:Tm^{3+}$ film propagation loss, increased thulium concentration, and optimized pump wavelength, enabled us to achieve a compact amplifier with 15 dB internal net gain in a 5-cm-long $TeO_2:Tm^{3+}$-Si_3N_4 spiral waveguide. The optimized thulium concentration was achieved with 4.2×10^{20} cm^{-3} of thulium ions and more amplifiers result in different lengths were provided in this section. These amplifier results showing higher gain on chips with different $TeO_2:Tm^{3+}$ film properties provide a guide for future work on optimization of integrated thulium amplifiers. The main results are summarized, and conclusions are given in section 3.5.

Thulium-doped tellurium oxide waveguide amplifier with 7.6 dB net gain on a silicon nitride chip

Khadijeh Miarabbas Kiani[1], Henry C. Frankis[1], Richard Mateman[2], Arne Leinse[2],
Andrew P. Knights[1], and Jonathan D. B. Bradley[1]
[1]McMaster University, 1280 Main Street West, Hamilton, ON, Canada
[2]LioniX International BV, PO Box 456, Enschede, 7500 AL, The Netherlands

This paper was published in Optics Letters in November 2019.
DOI: 10.1364/OL.44.005788

Section 3.4 on the high gain in compact spiral amplifiers was added in the following thesis chapter and will form the basis of a future submission for publication as a journal article. Minor modifications have also been made to the title, abstract, introduction, and conclusions based on these additional results.

Abstract

We report on thulium-doped waveguide amplifiers integrated on a low-loss silicon nitride platform. The amplifier structure consists of a thulium-doped tellurium oxide thin film coated on a silicon nitride strip waveguide on silicon. We determine a waveguide background loss of 0.7 dB/cm at 1479 nm based on the quality factor measured in microring resonators. Gain measurements were carried out in straight and 6.7-cm-long s-bend waveguides realized on a 2.2-cm-long chip. We measure internal net gain over the wavelength range 1860–2000 nm under 1620 nm pumping and up to 7.6 dB total gain at 1870 nm, corresponding to 1.1 dB/cm. Recently, I demonstrated a compact, high gain thulium-doped tellurium oxide waveguide amplifier with the net internal gain of 15.0 dB at 1870 nm, corresponding to 3.0 dB/cm. Gain measurements were carried out in a 5-cm spiral waveguide on a 1.6 mm chip with 200 µm bend radius. These results are promising for the realization of highly compact thulium-doped amplifiers in the emerging 2-µm band for silicon-based photonic microsystems.

3.1 Introduction

The 2-µm band has recently attracted interest for relieving a bandwidth bottleneck in data communications systems due to the development of low-loss, low nonlinearity, and low latency hollow-core photonic band-gap fibers, broadband thulium fiber amplifiers, and semiconductor optoelectronic devices including lasers, modulators and photodetectors [1–

3]. The 2-µm region is also of interest for photonic applications including free space communications, gas sensing, LIDAR, biomedicine, and nonlinear mid-infrared generation [4–6]. Silicon-based photonics offers a route towards compact photonic integrated circuits (PICs) for this emerging wavelength region of interest [7,8]. Silicon and silicon nitride (Si_3N_4) PICs have been developed with passive and active functionalities for applications including optical communications, nonlinear optics, and spectroscopic sensing [9–13].

One of the key components for 2-µm systems is an optical amplifier. Silicon-based amplifiers have been demonstrated using InP-based active regions directly bonded to a silicon substrate and monolithically grown ternary SiGeSn alloys [14,15]. Thulium-doped fiber amplifiers are key motivators for 2-µm systems on account of their broadest gain spectrum of all rare-earth-doped fiber amplifiers, significant enhancement of transmission bandwidths, high gain, low noise figure performance, and ultra-low nonlinearity as compared to semiconductor optical amplifiers [16–19]. Therefore, on-chip thulium-doped waveguides are an attractive option for high-performance amplifiers on silicon, with the added advantage that they can be fabricated using low-cost and high-volume methods. Integrated rare-earth-doped waveguide amplifiers on silicon have been demonstrated but have primarily focused on erbium for gain in the C and L bands [20] as opposed to thulium.

Recently we showed tellurium oxide (TeO_2) waveguides on a low loss silicon nitride platform [21,22]. TeO_2 is a promising host material for rare-earth ions due to high rare earth solubilities, low quenching, large emission bandwidth, high gain, and low phonon energies (~700–800 cm^{-1}) [23–25]. A high gain erbium-doped TeO_2 waveguide amplifier was recently shown with up to 2.8 dB/cm internal net gain [26]. Thulium-doped tellurium oxide (TeO_2:Tm^{3+}) amplifiers have been demonstrated in various platforms, including fibers, glass, channel waveguides and other integrated hosts materials such as $LiNbO_3$ [27–31] but not on a silicon or Si_3N_4 platform. Silicon nitride waveguides and cavities have recently been shown to be a path to high-performance monolithic light sources [32,33], including ultra-compact thulium microlasers [34] and high-power thulium waveguide lasers [35] using an aluminum oxide rare-earth host medium. Therefore, silicon nitride waveguides are also a promising route to on-chip amplifiers.

Here, we demonstrate a TeO_2:Tm^{3+} waveguide amplifier on a low-loss Si_3N_4 chip. We describe the film and waveguide fabrication, design, and characterization of the waveguide amplifier showing up to 7.6 dB peak internal net gain at 1870 nm wavelength. I subsequently show a high gain TeO_2:Tm^{3+} waveguide amplifier on a low-loss Si_3N_4 chip pumped at 1607 nm showing up to 15 dB internal net gain at 1870 nm and 2.5 dB internal net gain over the entire range of the wavelength from 1870 to 2000 nm. The gain measurements were carried out in 5-cm-long spiral waveguide realized on a 1.6-mm-long chip with an experimentally optimized thulium concentration of 4.2×10^{20} cm^{-3}. Ultimately, the results presented in this work show significant progress in developing a cost-effective, high gain, compact, and efficient integrated TeO_2:Tm^{3+} waveguide amplifier on a silicon nitride platform. Such integrated thulium-doped amplifiers are promising as gain elements for emerging photonic microsystems operating around 2 µm.

3.2 Design and Fabrication

We fabricated the thulium-doped waveguide amplifiers on a silicon nitride platform using a monolithic, reactive co-sputtering deposition processing step compatible with silicon photonic circuits outlined in [22]. We deposited a 0.2-µm-thick Si_3N_4 film on a 100-mm silicon wafer with 8-µm-thick thermal oxide layer using low-pressure chemical vapor deposition (LPCVD). Stepper lithography and reactive ion etching were applied to pattern 1.0-µm-wide straight and s-bend strip waveguides with lengths of 2.2 and 6.7 cm, respectively, on one chip and another chip containing microring resonators. The bend radius for the s-bend structures is 1390 µm to ensure minimal radiation loss [21]. A high temperature > 1100 °C annealing step in N_2 for several hours was applied to remove hydrogen from the Si_3N_4 layer and reduce absorption around 1.5 µm wavelength. The silicon nitride wafer was then diced into chips which were shipped from the foundry for additive processing steps to realize the Tm amplifiers.

We deposited a 0.29-µm-thick $TeO_2:Tm^{3+}$ coating layer onto the passive silicon nitride chips using a radio frequency (RF) reactive co-sputtering process. Three-inch metallic tellurium and thulium targets with 99.999 and 99.9% purity, respectively, were sputtered in an argon/oxygen atmosphere at ambient temperature. We set the Te and Tm RF sputtering powers to 145 W and 65 W, respectively, and the Ar and O_2 flow rates to 12 sccm and 6.8 sccm, respectively. The deposition rate for the $TeO_2:Tm^{3+}$ film was measured to be 19 nm/min, with a refractive index of 2.10 at 638 nm and 2.04 at 1550 nm wavelengths measured by spectroscopic ellipsometry for the films deposited on silicon. Thin film propagation loss of ≤ 0.2 dB/cm at 1510 nm determined using the prism coupling method. We measured a thulium ion dopant concentration of 2×10^{20} cm^{-3} using Rutherford backscattering spectrometry (RBS). We prepared smooth waveguide end facets using focused-ion-beam (FIB) milling [22]. A 1-µm-thick fluoropolymer top cladding was spun onto the chips (Cytop, with refractive index equal to 1.33 at 1550 nm).

Figures 3.1(a) and 3.1(b) show a 3D drawing and cross section diagram of the TeO_2:Tm^{3+}-coated Si_3N_4 waveguide structure, respectively. The calculated electric field profiles of the transverse-electric- (TE-) polarized fundamental modes for pump and signal wavelengths using a finite-element method mode solver are displayed in figures 3.1(c) and 1(d). The waveguides were designed to achieve single mode waveguide conditions at 1.62 µm and 2 µm wavelengths. Due to the asymmetry of the waveguide structure simulations show that the waveguide structure only supports the TE-polarized mode at both wavelengths. According to simulation results approximately 52 % of the optical power at 1.62 µm is confined in the TeO_2:Tm^{3+} coating, with 22 % confined to the nitride layer, and the rest of the optical power in the upper and lower cladding. At the signal wavelength, 45% of the optical power is in the TeO_2:Tm^{3+} coating, with 19% confined to the nitride layer, and the rest of the optical power in the upper and lower cladding. The optical confinement can be increased up to almost 85% in the coating by thicker TeO_2Tm^{3+} coatings [22]. The calculated mode area is 1.7 µm^2 which is ~8% of the mode area of a standard 9/125 single mode fiber (30 µm^2). The pump-signal mode overlap factor is calculated to be 97%.

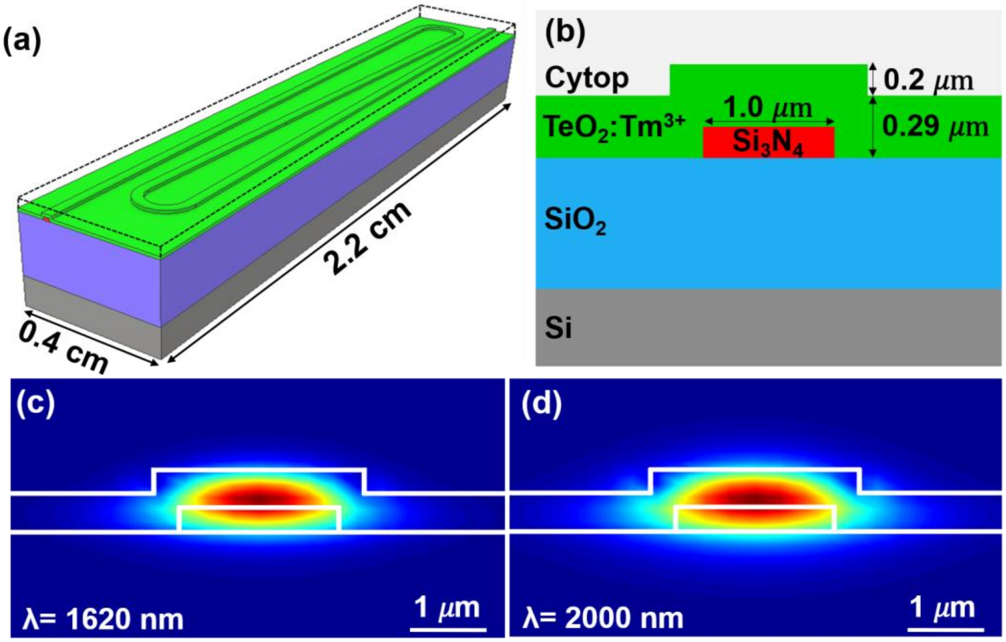

FIGURE 3.1: a) 3D drawing of the s-bend amplifier. b) Cross-section profile of the $TeO_2:Tm^{3+}$-coated Si_3N_4 waveguide structure. c) and d) Calculated electric field profile of the fundamental TE-polarized mode for a silicon nitride strip width and height of 1.0 and 0.2 µm, respectively, and $TeO_2:Tm^{3+}$ film height of 0.29 µm at 1.62-µm and 2-µm wavelengths, respectively.

3.3 Results

We characterized the transmission and optical gain in the waveguides using the fiber edge-coupling setup shown in figure 3.2. Pump light from a tunable 1550-nm laser set at 1620 nm and high-power L-band erbium-ytterbium-co-doped fiber amplifier (L-band EYDFA) and signal light from a 1860–2000 nm tunable laser were coupled to the chip via polarization controllers, a 1600/1900 nm wavelength division multiplexer (WDM) and 2-µm spot size tapered fiber at 1550-nm wavelength mounted on an xyz stage. A lensed fiber with a 3±0.5 µm spot size at 2 µm wavelength and xyz stage were used to couple light from the chip where it was coupled through a fiber WDM and free-space filter with minimum in-band-transmission of 70 % and more than 99.9 % reflection to filter residual pump light.

During measurements the polarization paddles and xyz stages were adjusted to select TE polarization and maximize the transmitted signal intensity.

To characterize the background waveguide propagation loss, we used $TeO_2:Tm^{3+}$-coated silicon nitride ring resonator. Transmission measurements were carried out using the tunable 1550-nm pump laser on a ring with a 1.0-µm-wide Si_3N_4 waveguide, 0.29-µm-thick $TeO_2:Tm^{3+}$ coating, 300-µm radius, and a 1.6-µm bus waveguide-ring gap to determine waveguide loss. We assumed to have negligible thulium absorption loss over the wavelength range 1470 to 1525 nm, and measurements represent the passive waveguide loss of the structure.

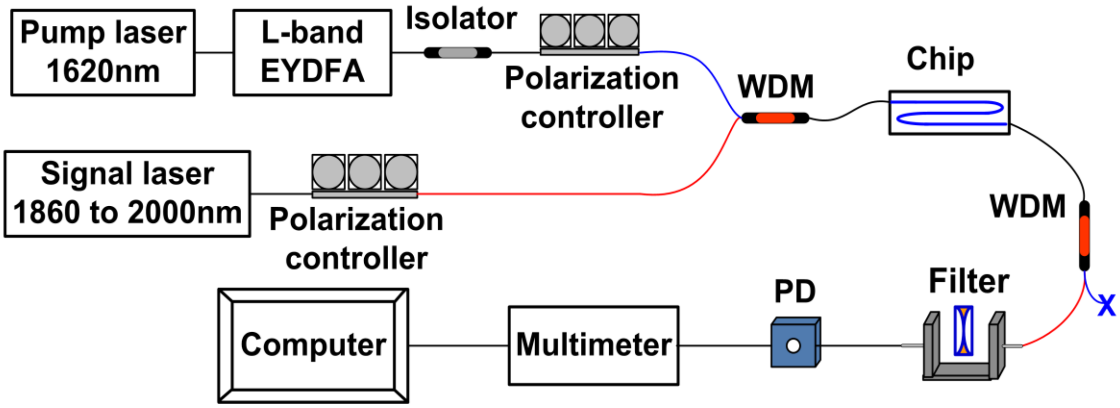

FIGURE 3.2: a) Experimental setup for measuring the transmission and gain in the thulium-doped waveguide amplifiers. (WDM: wavelength division multiplexer, PD: photodetector).

As shown in figure 3.3(a), an internal quality factor of 4.9×10^5 was fit to the resonance spectrum obtained in an under-coupled ring resonator corresponding to 0.7 dB/cm waveguide propagation loss at 1479 nm wavelength [21], which is outside the Tm absorption range and can be taken as the pump background loss. Based on cut-back loss measurements at 1550 nm and 2000 nm in undoped TeO_2-coated Si_3N_4 waveguides we expect similar or better background propagation loss at the 1860–2000 nm signal wavelengths. Here we confirmed similar background signal loss of ~0.7 dB/cm in the Tm-doped waveguide via transmission measurements around 2000 nm and accounting for the fiber-chip coupling loss of 6 dB per facet [22].

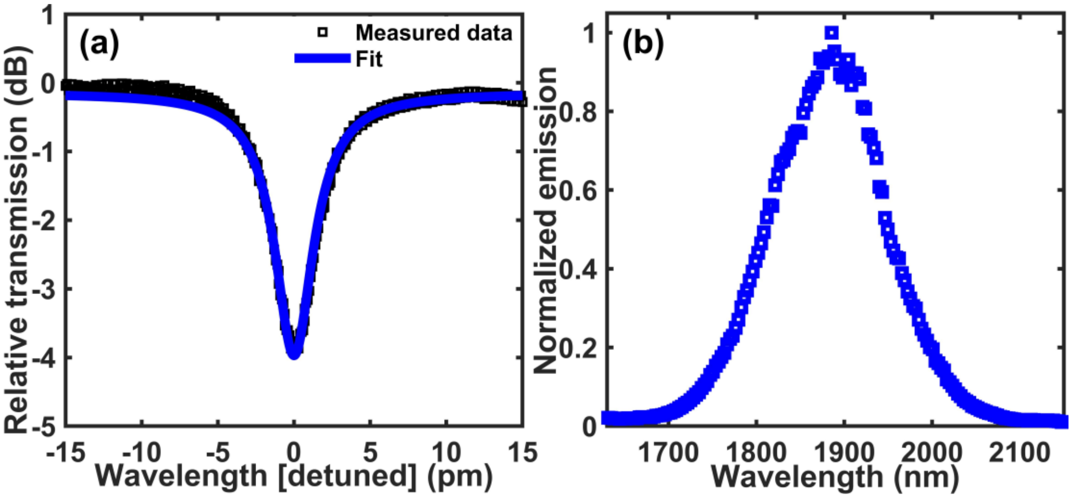

FIGURE 3.3: a) Measured and fitted resonance at 1479 nm for a 1.0-µm-wide Si_3N_4 ring waveguide with a 0.29 µm thick TeO_2:Tm^{3+} coating, 300-µm radius, and 1.6-µm gap to determine the waveguide background loss. b) Amplified spontaneous emission spectrum measured in TeO_2:Tm^{3+}-coated Si_3N_4 waveguide.

Figure 3.3(b) shows the normalized amplified spontaneous emission (ASE) spectrum measured in the straight thulium-doped tellurium oxide on silicon nitride waveguide. The emission spectrum was recorded using a pump wavelength of 1620 nm and by collecting the back ASE from the input WDM using a near infrared spectrometer. The emission spectrum extends from 1.7 to 2.1 µm with the peak at 1870 nm.

Gain measurements were carried out using the setup shown in figure 3.2. The output signal was measured at the detector with the pump on and off to determine the signal enhancement. The measured signal enhancement must be greater than both the thulium absorption loss and the background waveguide loss, to achieve positive internal net gain. The total propagation loss in the waveguide was determined by multiplying the background loss obtained of 0.7 dB/cm by the waveguide length and adding the thulium absorption versus wavelength measured in the unpumped waveguide. The total loss was subtracted from the signal enhancement to determine the internal net gain of the waveguide. The output power of the signal laser from 1860 to 2000 nm was maintained at −10 dBm resulting in an approximate signal power launched into the chip of −19 dBm accounting for fiber setup and coupling loss. This signal power was determined to be sufficiently low to be in the small signal regime (i.e. resulting in negligible inversion of Tm^{3+} ions throughout the waveguide) while being sufficiently high to ensure stable tunable laser operation. We determined the launched pump power by measuring the incident power from the input fiber using an integrating sphere photodiode power monitor and accounting for 6 dB fiber-chip coupling loss [22].

Figure 3.4 shows the internal net gain versus wavelength for 7 different launched 1620-nm pump powers including 0, 30, 55, 110, 165, and 220, and 245 mW. The unpumped case shows the absorption spectrum corresponding to the same waveguide from 1860 to 2000 nm. The data shows broadband net optical gain is obtained between 1860–2000 nm for pump powers > ~60 mW. A peak internal net gain of 7.6 dB is obtained at 1870 nm for 245 mW launched power, corresponding to the peak Tm emission wavelength, while net gain > 2.9 dB is obtained over the entire range.

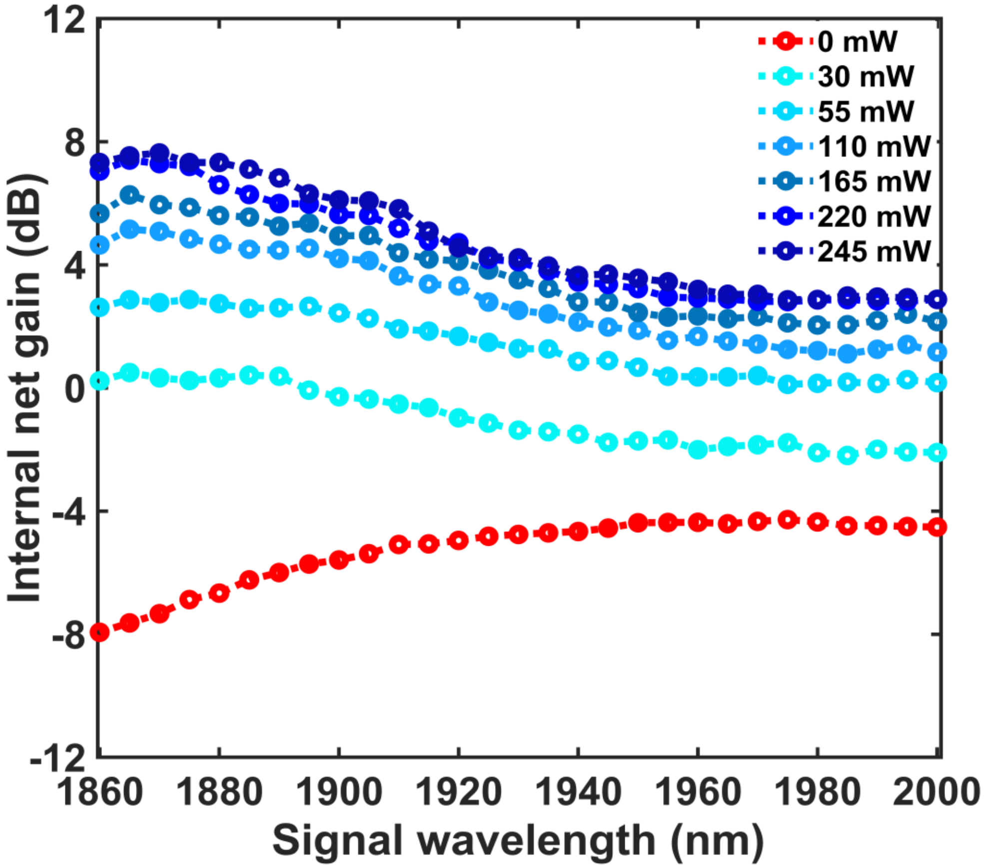

FIGURE 3.4: Internal net gain vs. wavelength measured in a 6.7-cm-long paperclip Tm-doped waveguide amplifier at different launched 1620-nm pump powers.

Figure 3.5 shows the internal net gain vs. pump power at different signal wavelengths for the s-bend $TeO_2:Tm^{3+}$-coated Si_3N_4 waveguide. Threshold gain is shown to be achieved at 30 mW launched pump power at 1870 nm. The peak gain value of 7.6 dB corresponds to a gain per unit length of 1.1 dB/cm. The inset shows the internal net gain measured versus launched pump power for the 2.2-cm-long straight waveguide and 6.7 cm s-bend waveguide and 1620 and 1870 nm pump and signal wavelengths, respectively. The saturated small signal gain in the case of the shorter wavelength is 2.6 dB, corresponding to 1.2 dB/cm, confirming that the gain measured in the s-bend waveguide is close to the maximum gain obtainable for this structure.

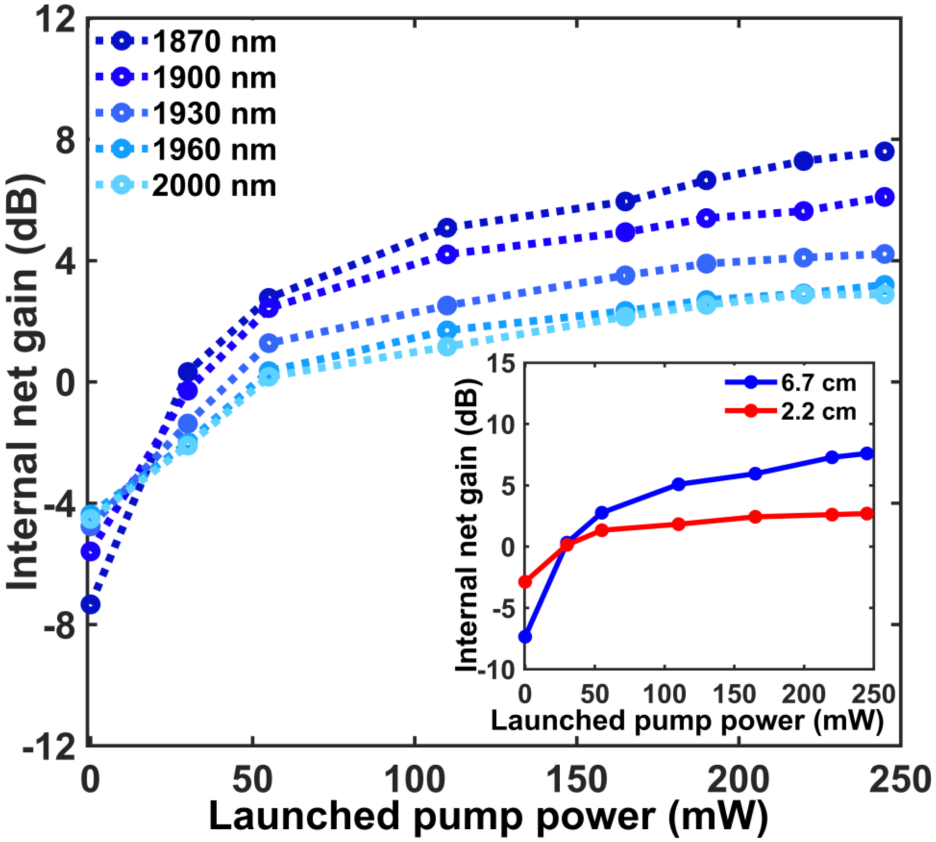

FIGURE 3.5: Internal net gain vs. pump power measured in a 6.7-cm-long $TeO_2:Tm^{3+}$ paperclip waveguide amplifier for 1620-nm pump wavelength and varying signal wavelength. Inset: internal net gain vs. pump power for amplifier lengths of 2.2 cm, and 6.7 cm at 1870-nm signal wavelength.

In the future, the amplifier performance can be improved by optimizing the waveguide cross-section including a thicker $TeO_2:Tm^{3+}$ layer for greater mode overlap with the gain medium, amplifier length, pump wavelength, and Tm^{3+} ion concentration based on the spectroscopic properties of the $TeO_2:Tm^{3+}$ material. We are currently carrying out spectroscopy measurements and developing a rate equation model in order to optimize the gain.

3.4 Compact High Gain $TeO_2:Tm^{3+}$ Waveguide Amplifiers

Following the initial results showing net gain in $TeO_2:Tm^{3+}$-Si_3N_4 amplifiers, higher gain in a smaller footprint device was investigated. The amplifier performance was improved by adjusting the waveguide cross-section including a thicker $TeO_2:Tm^{3+}$ layer for greater mode overlap with the gain medium, amplifier length, pump wavelength, and Tm^{3+} ion concentration based on the spectroscopic properties of the $TeO_2:Tm^{3+}$ films. A 1.0-µm-wide spiral waveguide with a bend radius of 200 µm on 200-nm-thick silicon nitride layer was coated with a 0.39-µm-thick $TeO_2:Tm^{3+}$ layer with a thulium ion dopant concentration of 4.2×10^{20} cm^{-3} and was pumped to explore its amplification properties.

The output power of the signal laser from 1870 to 2000 nm was maintained at −10 dBm resulting in an approximate signal power launched into the chip of −22 dBm accounting for fiber setup and coupling loss. This signal power was determined to be sufficiently high to ensure stable tunable laser operation while being sufficiently low to be in the small signal regime. The launched pump power was determined by measuring the incident power from the input fiber using an integrating sphere photodiode power monitor and accounting for 16 dB fiber-chip coupling loss at pump wavelength.

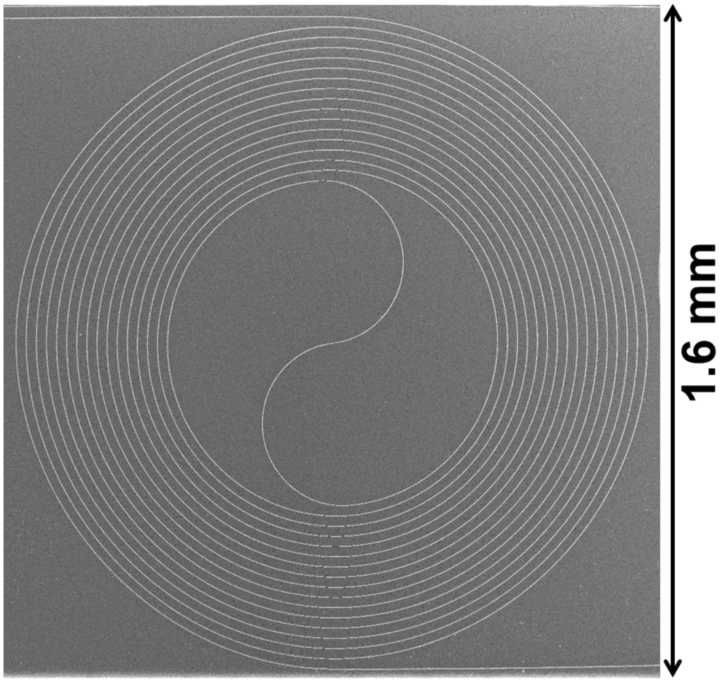

FIGURE 3.6: Top-view SEM image of a 5-cm-long TeO_2:Tm^{3+}-coated Si_3N_4 spiral waveguide.

The same process for determining background loss with a ring resonator on the same chip as that described in section 3.3 was used. An internal quality factor of 4.5×10^5 was fit to the resonance spectrum of an under-coupled ring resonator, corresponding to 0.75 dB/cm waveguide propagation loss at 1510 nm wavelength, suggesting 8 dB of fiber-chip coupling loss at each facet. The optical propagation loss was measured of 0.3 dB/cm in the fabricated paperclip on the same chip at 2000 nm wavelength. The paperclip waveguide structures are with different lengths varying from 2.45 to 3.93 cm. The propagation loss was fitted using linear regression of the insertion losses measured in the paperclip at 2000 nm wavelength.

To measure the maximum internal net gain per unit length, the gain was measured in short 1-cm-long straight waveguide amplifiers with varying Tm concentrations. The internal net gain versus launched pump power measured in 1-cm-long TeO_2:Tm^{3+} straight waveguide amplifiers is shown in figure 3.7 for thulium concentrations ranging from 2.0×10^{20} cm^{-3} to 6.0×10^{20} cm^{-3}. The highest internal net gain was measured for the thulium-doped tellurium amplifier with the thulium concentration of 4.2×10^{20} cm^{-3}.

A significant reduction was observed in the gain per unit length at higher thulium concentrations. This can occur by increasing the background loss due to the different post-processing runs and the quenching process. The inset of figure 3.8 shows luminescent lifetime measurements that were carried out on the 1-cm-long $TeO_2:Tm^{3+}$ waveguides using a diode laser that was modulated with a 5 μs turn off time, by a 40 Hz square wave signal using a function generator and the output was launched onto the chip. The back-collected fluorescence signal was recorded of the photodetector on an oscilloscope from the waveguide and its decay after the pumping was switched off was fit in a logarithmic scale to calculate the lifetime. The lifetime decreases for increasing thulium concentration, which might be attributed to quenched ions, OH^- impurities, background waveguide loss [36]. This decreasing lifetime leads to lower pumping efficiency and reduced gain beyond the optimum concentration for a given amplifier length.

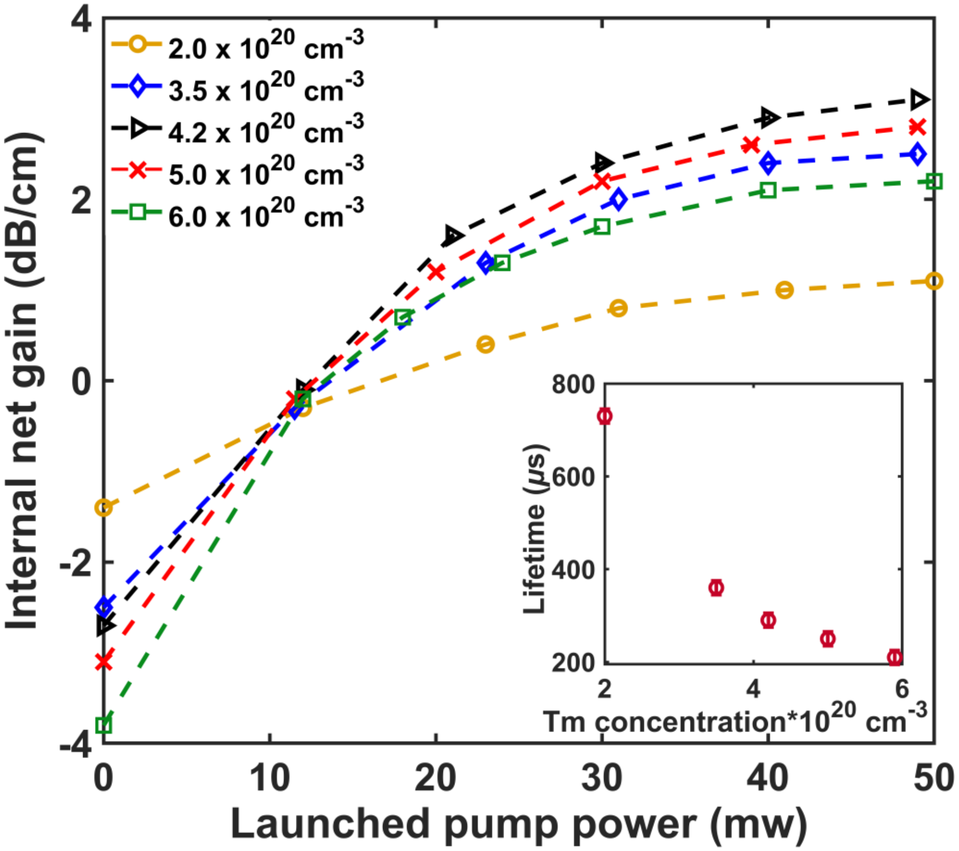

FIGURE 3.7: Measured internal net gain per unit length versus launched pump power for different thulium concentrations at signal and pump wavelengths of 1870 and 1607 nm, respectively, in 1-cm long $TeO_2:Tm^{3+}$ straight waveguide amplifiers. Inset: measured luminescent lifetime versus thulium concentration.

Figure 3.8 shows the internal net gain versus wavelength for different launched pump powers ranging from 0 to 49 mW at 1607-nm pump wavelength. The unpumped case shows the absorption spectrum corresponding to the same waveguide from 1870 to 2000 nm. A peak internal net gain of 15 dB is demonstrated at 1870 nm for 49 mW launched power, while internal net gain of > 2.5 dB is obtained over the entire range. Threshold gain is shown to be achieved at ~10 mW launched pump power pumped at 1607 nm with a peak gain value of 15 dB, corresponding to a gain per unit length of 3 dB/cm.

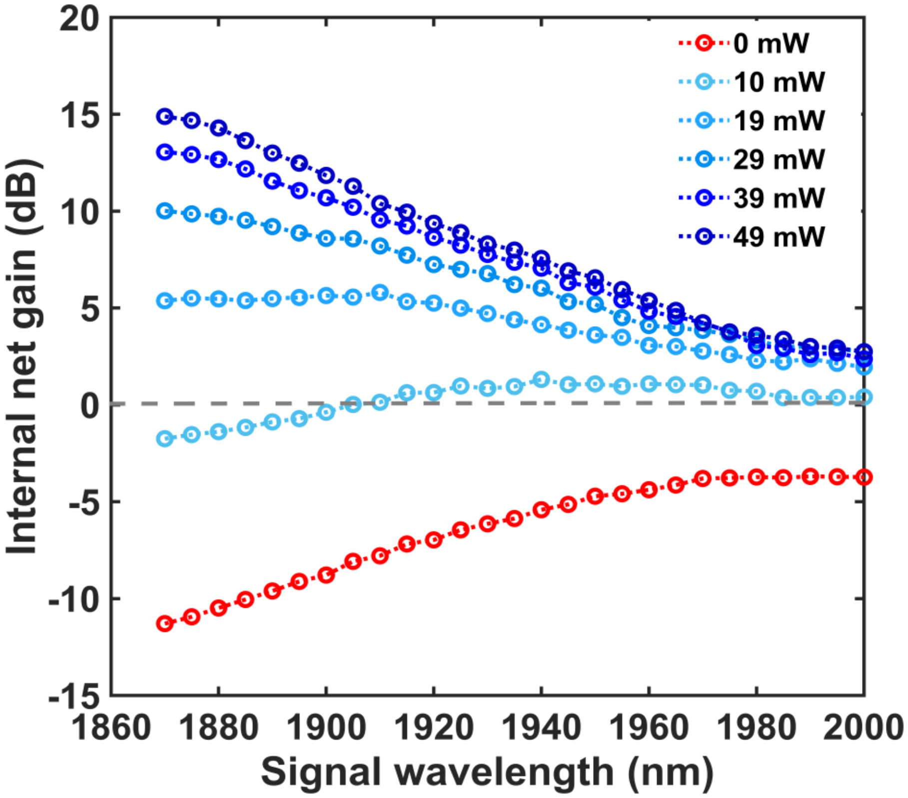

FIGURE 3.8: Internal net gain vs. wavelength measured in a 5-cm-long spiral Tm-doped waveguide amplifier at different launched 1607-nm pump powers.

The results presented in this work are prominent in comparison to the highest net gain in the $TeO_2:Tm^{3+}$ waveguide amplifier from the previous work in our group with 1.2 dB/cm internal net gain [37]. Outstanding progress has been conducted in this work including high total internal net gain, high gain per unit length, an ultra-compact spiral amplifier with a broad bandwidth net gain operation over 130 nm wavelength.

3.5 Conclusion

In summary, a thulium-doped tellurium oxide waveguide amplifier have been demonstrated with up to 7.6-dB internal net gain and net gain between 1860–2000 nm on a silicon nitride platform. Subsequently, a high total internal net gain of 15 dB, corresponds to a higher gain per unit length of 3 dB/cm on an ultra-compact 5-cm spiral waveguide with a broad bandwidth net gain operation over 130 nm wavelength have been demonstrated by optimizing the waveguide cross-section, amplifier length, pump wavelength, and thulium concentration. Such devices are promising for ultra-compact optical amplifiers in the proposed 2-µm optical communications band, empowering applications such as telecommunication chips, data transmission, quantum and optical computing, for which on-chip optical gain is required.

Bibliography

[1] D. J. Richardson, “Applied physics. Filling the light pipe,” *Science* **330**, 327 (2010).

[2] R. Soref, “Enabling 2 µm communications,” *Nat. Photonics* **9**, 358 (2015).

[3] F. C. Garcia Gunning, N. Kavanagh, E. Russell, R. Sheehan, J. O ’Callaghan, and B. Corbett, “Key enabling technologies for optical communications at 2000 nm,” *Appl. Opt.* **57**, E64 (2018).

[4] K. Scholle, S. Lamrini, P. Koopmann, and P. Fuhrberg, “2 µm laser sources and their possible applications,” *in Frontiers in Guided Wave Optics and Optoelectronics* (InTech, 2010).

[5] Q. Wang J. Geng, and S. Jiang, “2-µm fiber laser sources for sensing,” *Opt. Eng.* **53**, 061609 (2014).

[6] M. Tao, T. Yu, Z. Wang, H. Chen, Y. Shen, G. Feng, and X. Ye, “Super-flat supercontinuum generation from a Tm-doped fiber amplifier,” *Sci. Rep.* **6**, 23759 (2016).

[7] D. J. Thomson, L. Shen, J. J. Ackert, E. Huante-Ceron, A. P. Knights, M. Nedeljkovic, A. C. Peacock, and G. Z. Mashanovich, "Optical detection and modulation at 2μm-2.5μm in silicon," *Opt. Express* **22**, 10825 (2014).

[8] J. J. Ackert, D. J. Thomson, L. Shen, A. C. Peacock, P. E. Jessop, G. T. Reed, G. Z. Mashanovich, and A. P. Knights, "High-speed detection at two micrometres with monolithic silicon photodiodes," *Nat. Photonics* **9**, 393 (2015).

[9] D. J. Blumenthal, R. Heideman, D. Geuzebroek, A. Leinse, and C. Roeloffzen, "Silicon nitride in silicon photonics," *Proc. IEEE* **106**, 2209 (2018).

[10] M. Lamy, C. Finot, A. Parriaux, C. Lacava, T. Dominguez Bucio, F. Gardes, G. Millot, P. Petropoulos, and K. Hammani, "Si-rich Si nitride waveguides for optical transmissions and toward wavelength conversion around 2 μm," *Appl. Opt.* **58**, 5165 (2019).

[11] K. Shtyrkov, P. A. T. Callahan, N. Li, E. S. Magden, A. Ruocco, D. Vermeulen, F. X. Kärtner, M. R. Watts, and E. P. Ippen, "Integrated CMOS-compatible Q-switched mode-locked lasers at 1900nm with an on-chip artificial saturable absorber," *Opt. Express* **27**, 3542 (2019).

[12] R. Wang, A. Vasiliev, M. Muneeb, A. Malik, S. Sprengel, G. Boehm, M. C. Amann, I. Šimonyt, A. Vizbaras, K. Vizbaras, R. Baets, and G. Roelkens, "III–V-on-silicon photonic integrated circuits for spectroscopic sensing in the 2–4 μm wavelength range," *Sensors* **17**, 1788 (2017).

[13] P. Latawiec, V. Venkataraman, M. J. Burek, B. J. M. Hausmann, I. Bulu, and M. Lončar, "On-chip diamond Raman laser," *Optica* **2,** 924 (2015).

[14] R. Soref, “Silicon-based silicon-germanium-tin heterostructure photonics,” *Phil. Trans. R. Soc.* A **372**, 1098 (2014).

[15] N. Volet, A. Spott, E. J. Stanton, M. L. Davenport, L. Chang, J. D. Peters, T. C. Briles, I. Vurgaftman, J. R. Meyer, and J. E. Bowers, “Semiconductor optical amplifiers at 2.0-μm wavelength on silicon,” *Laser Photonics Rev.* **11**, 1600165 (2017).

[16] Z. Li, A. M. Heidt, J. M. O. Daniel, Y. Jung, S. U. Alam, and D. J. Richardson, “Thulium-doped fiber amplifier for optical communications at 2μm,” *Opt. Express* **21**, 9289 (2013).

[17] Z. Li, A. M. Heidt, N. Simakov, Y. Jung, J. M. O. Daniel, S. U. Alam, and D. J. Richardson, “Diode-pumped wideband thulium-doped fiber amplifiers for optical communications in the 1800 – 2050 nm window,” *Opt. Express* **21**, 26450 (2013).

[18] J. Wang, S. Liang, Q. Kang, Y. Jung, S. Alam, and D. J. Richardson, “Broadband silica-based thulium doped fiber amplifier employing multi-wavelength pumping,” *Opt. Express* **24**, 23001 (2016).

[19] M. A. Khamis and K. Ennser, “Theoretical model of a thulium-doped fiber amplifier pumped at 1570 nm and 793 nm in the presence of cross relaxation,” *J. Lightwave Technol.* **34**, 5675 (2016).

[20] J. D. B. Bradley and M. Pollnau, “Erbium-doped integrated waveguide amplifiers and lasers,” *Laser Photonics Rev.* **5**, 368 (2011).

[21] H. C. Frankis, K. Miarabbas Kiani, D. Su, R. Mateman, A. Leinse, and J. D. B. Bradley, “High-Q tellurium-oxide-coated silicon nitride microring resonators,” *Opt. Lett.* **44**, 118 (2019).

[22] H. C. Frankis, K. Miarabbas Kiani, D. B. Bonneville, C. Zhang, S. Norris, R. Mateman, A. Leinse, N. D. Bassim, A. P. Knights, and J. D. B. Bradley, "TeO_2 waveguides integrated on a low-loss Si_3N_4 platform for application in scalable photonic circuits," *Opt. Express* **27**, 12529 (2019).

[23] J. S. Wang, E.M. Vogel, and E. Snitzer , "Tellurite glass: a new candidate for fiber devices," *Opt. Mater.* **3,** 187 (1994).

[24] S. Shen, A. Jha, X. Liu, M. Naftaly, K. Bindra, H. J. Bookey, and A. K. Kar, "Tellurite glasses for broadband amplifiers and integrated optics," *J. Am. Ceram. Soc.* **85**, 1391 (2002).

[25] A. Jha, B. Richards, G. Jose, T. Teddy-Fernandez, P. Joshi, X. Jiang, and J. Lousteau, "Rare-earth ion doped TeO_2 and GeO_2 glasses as laser materials," *Prog. Mater. Sci*. **57**, 1426 (2012).

[26] K. Vu and S. Madden, "Tellurium dioxide erbium doped planar rib waveguide amplifiers with net gain and 2.8dB/cm internal gain," *Opt. Express* **18**, 19192 (2010).

[27] G. Nunzi Conti, S. Berneschi, M. Bettinelli, M. Brenci, B. Chen, S. Pelli, A. Speghini, and G.C. Righini, "Rare –earth doped tungsten tellurite glasses and waveguides: fabrication and characterization," *J. Non-Cryst. Solids* **345&346**, 343 (2004).

[28] H. Gebavi, S.Taccheo, and D. Milanese, "The enhanced two micron emission in thulium doped tellurite glasses," *Opt. Mater.* **35**, 1792 (2013).

[29] S. V. Muravyev, E. A. Anashkina, A. V. Andrianov, V. V. Dorofeev, S. E. Motorin, M. Y. Koptev, and A. V. Kim, "Dual-band Tm^{3+}-doped tellurite fiber amplifier and laser at 1.9 μm and 2.3 μm," *Sci. Rep.* **8**, 16164 (2018).

[30] M. George, "Ti:Tm:$LiNbO_3$ waveguide amplifiers and lasers," Ph.D. Thesis (University of Paderborn, Germany, 2012).

[31] A. S. K. Tong, C. J. Mitchell, J. I. Mackenzie, and J. S. Wilkinson, "Photoluminescence of Tm-doped Ta_2O_5 waveguides," *in Conference on Lasers and Electro-Optics (CLEO)*, OSA Technical Digest Series, s2545 (2014).

[32] Purnawirman, J. Sun, T. N. Adam, G. Leake, D. Coolbaugh, J. D. B. Bradley, E. Shah Hosseini, and M. R. Watts, "C- and L-band erbium-doped waveguide lasers with wafer-scale silicon nitride cavities," *Opt. Lett.* **38**, 1760 (2013).

[33] M. Belt, T. Huffman, M. L. Davenport, W. Li, J. S. Barton, and D. J. Blumenthal, "Arrayed narrow linewidth erbium-doped waveguide-distributed feedback lasers on an ultra-low-loss silicon-nitride platform," *Opt. Lett.* **38**, 4825 (2013).

[34] Z. Su, N. Li, E. S. Magden, M. Byrd, Purnawirman, T. N. Adam, G. Leake, D. Coolbaugh, J. D. B. Bradley, and M. R. Watts, "Ultra-compact and low threshold thulium microcavity laser monolithically integrated on silicon," *Opt. Lett.* **41**, 5708 (2016).

[35] N. Li, Purnawirman, Z. Su, E. S. Magden, P. T. Callahan, K. Shtyrkova, M. Xin, A. Ruocco, C. Baiocco, E. P. Ippen, F. X. Kärtner, J. D. B. Bradley, D. Vermeulen, and M. R. Watts, "High-power thulium lasers on a silicon photonics platform," *Opt. Lett.* **42**, 1181 (2017).

[36] N. J. Ramírez-Martínez, M. Núñez-Velázquez, and J. K. Sahu, "Study on the dopant concentration ratio in thulium-holmium doped silica fibers for lasing at 2.1µm," *Opt. Express* **28**, 24961-24967 (2020).

[37] K. Miarabbas Kiani, H. C. Frankis, H. M. Mbonde, R. Mateman, A. Leinse, A. P. Knights, and J. D. B. Bradley, “Thulium-doped tellurium oxide waveguide amplifier with 7.6 dB net gain on a silicon nitride chip,” *Opt. Lett.* **44**, 5788-5791 (2019).

Chapter 4

Thulium-Doped Tellurium Oxide Microring Lasers Integrated on a Low-Loss Silicon Nitride Platform

Thesis preface

The following chapter presents on the design, fabrication, and characterization of the integrated thulium-doped tellurium oxide ($TeO_2:Tm^{3+}$) microring lasers on a low-loss silicon nitride (Si_3N_4) platform. Large-scale implementation of silicon photonics (SiP) telecommunication infrastructure will require light sources (lasers) to generate signals on the chip. The low propagation loss and wide transparency window of Si_3N_4, make it a versatile complimentary silicon-compatible platform for on-chip passive, active, and nonlinear devices. Here, a thulium gain medium is added on low-loss Si_3N_4 microring resonators to realize compact integrated lasers. The thulium-doped tellurium oxide (TeO_2:Tm^{3+}) is deposited onto foundry-fabricated Si_3N_4 chips via reactive radio frequency (RF) co-sputtering, which is a straightforward and monolithic approach that can be extended to the wafer scale, in the Centre for Emerging Device Technologies (CEDT) at McMaster University. The passive transmission properties and lasing were characterized on chips with a silicon nitride microring with a radius of 300 µm and Tm concentrations of 3.6, 4.1 and 5.9 × 10^{20} atom/cm^{3+}. The microring laser with a thulium concentration of 4.1 × 10^{20} atoms/cm^3 is selected for detailed measurements and forms the focus of this chapter due to its measured lower threshold power and higher slope efficiency.

An introduction and motivation for integrated thulium lasers on the silicon nitride platform is given in section 4.1. Section 4.2 describes the microring laser design, fabrication and structure, which includes a 300 µm radius and 200 nm thick Si_3N_4 microring resonator coated with 390 nm thick-TeO_2:Tm^{3+} layer as the active area of the laser. In section 4.3, the optical passive transmission properties is characterized of the microring resonators, including the Q factor and losses, using a fiber-chip coupling setup. In section 4.4 the TeO_2:Tm^{3+}-Si_3N_4 microring resonators is pumped to explore their lasing potential and the laser results is described. Multimode and single-mode lasing are shown with a double-sided output power of approximately 9 mW around a wavelength of 1828 nm via efficient pumping at telecom wavelengths around 1610 nm, with a single-sided slope efficiency of 11% versus launched pump power into the silicon nitride bus waveguide. Furthermore, laser emission spectra is characterized for devices with different gaps of 0.9, 1.1, 1.4, 1.6, and 1.8 µm, which show multi-mode lasing and laser modes spanning from 1815 to 1895 nm. Section 4.5 presents additional laser results for devices with different thulium concentrations. The results are compared and provide a guide towards optimized $TeO_2:Tm^{3+}-Si_3N_4$ microring lasers. The main results are summarized, and conclusions are given in section 4.6.

Thulium-doped tellurium oxide microring lasers integrated on a low-loss silicon nitride platform

Khadijeh Miarabbas Kiani[1], Henry C. Frankis[1], Richard Mateman[2], Arne Leinse[2], Andrew P. Knights[1], and Jonathan D. B. Bradley[1]
[1]McMaster University, 1280 Main Street West, Hamilton, ON, Canada
[2]LioniX International BV, PO Box 456, Enschede, 7500 AL, The Netherlands

This paper was published in Optical Materials Express in October 2021.
DOI: 10.1364/OME.444087

Sections added in the following thesis chapter that were not included in the published manuscript include section 4.5. on the study of $TeO_2:Tm^{3+}-Si_3N_4$ microring lasers with different Tm concentrations. These laser results were made to include details to show the high performance and repeatability of the $TeO_2:Tm^{3+}-Si_3N_4$ hybrid platform for integrated thulium lasers.

Abstract

We demonstrate compact, monolithically integrated thulium-doped tellurium oxide microring lasers on a low-loss silicon nitride platform. We observe lasing in the wavelength range of 1815–1895 nm under 1610 nm resonant pumping at varying waveguide-microring gap sizes and on-chip single-sided output powers up to 4.5 mW. The microlasers exhibit thresholds as low as 18 mW (11 mW) and a single-sided slope efficiency as high as 11% (17%) with respect to the pump power coupled into the $TeO_2:Tm^{3+}$-coated Si_3N_4 bus waveguide (absorbed pump power). These results are a promising development for integrated tellurite glass devices and light sources for the emerging 2-µm band in silicon nitride photonic integrated circuits.

4.1 Introduction

Laser sources and optical amplifiers operating in the 2 µm window (~1.7–2.3 µm) are of increasing importance for diverse applications, including free-space and fiber-optic communications, medical diagnostics and surgery, spectroscopy, light detection and ranging (LIDAR), and sensing [1–3]. In particular, the 2-µm band has recently attracted interest for relieving a bandwidth bottleneck in data communications systems, due to the development of low-loss, and low latency hollow-core photonic bandgap fibers, low nonlinearity, broadband thulium fiber amplifiers, and semiconductor optoelectronic lasers, photodetectors, and modulators [4,5]. For applications requiring a small form factor, silicon has emerged as an ideal platform for compact, low-loss, and high-speed 2-µm integrated photonic devices and systems [6–8]. In addition, silicon nitride's (Si_3N_4's) low propagation loss (≤ 0.1 dB⁄cm) and wide transparency window (~400 nm to 2.35 µm), high refractive index contrast, nanoscale feature resolution, and mature fabrication methods has made it a versatile complimentary silicon-compatible platform for passive, active, and nonlinear devices [9–14]. However, due to the indirect bandgap and two photon absorption of silicon and large bandgap of silicon nitride, researchers are investigating different materials to integrate 2-µm band laser sources and amplifiers on silicon chips [15–17].

Trivalent thulium ions can be pumped at telecom wavelengths around 1.6 µm and show broad emission on the $^3F_4$ excited state to $^3H_6$ ground state energy transition. Thulium lasers are of interest for 2 µm applications because of their high efficiencies, high output powers, design flexibility and eye-safe emission at wavelengths ranging from 1.7 to 2.2 µm. 2-µm thulium lasers have been developed using glass fibers [18–20], planar and channel waveguides [21–24], and bulk crystals [25], and other integrated hosts materials such as $LiNbO_3$ [26]. Compared to fiber and bulk platforms, integrated waveguide lasers are compact, low cost, and use straightforward fabrication methods, enabling wafer-scale processing and integration with other photonic devices for compact high-performance microsystems [27–29]. Besides continuous wave devices, waveguide lasers have high potential for advanced light sources such as tunable lasers [30,31] and mode-locked lasers for applications such as low-noise frequency synthesis [24]. High performance integrated thulium-doped channel waveguide lasers have been developed in a variety of oxide host materials. Tungstate crystals are particularly promising based on their high rare earth solubility without clustering, resulting in high performance laser demonstrations [32], including devices with a maximum output power of 262 mW and slope efficiency of 82.6%

[33]. Recently, thulium lasers have also been demonstrated on silicon and silicon nitride, enabling them to leverage the low-cost, scalable manufacturing and advanced device libraries and microsytems functionalities available on those platforms. Low-threshold Tm-doped microcavity lasers and high-power Tm-doped distributed feedback (DFB) and distributed Bragg reflector (DBR) lasers on silicon have been demonstrated based on micro-trenches and Si_3N_4 waveguides coated with Tm-doped amorphous Al_2O_3 gain layers [22,23]. A high gain coefficient and high laser power were also achieved by applying a high Tm concentration and a well-confined waveguide structure for compact integrated devices in a Tm-doped Ta_2O_5 waveguide on silicon [21].

Compared to other metal oxides, tellurium dioxide (TeO_2), is a highly promising material for active monolithically integrated optical devices and host for rare-earth ions due to its high rare-earth solubility, low quenching, and low phonon energy of around 600–800 cm^{-1} [34]. TeO_2 has a high refractive index and is transparent throughout the visible and near-infrared and into the mid-infrared with low dispersion. It also has higher nonlinearity and higher Raman gain than Si_3N_4 [34–36]. Thus, TeO_2 is an ideal medium for active (light-emitting), passive, and nonlinear devices on a single platform. Its low temperature and straightforward wafer-scale deposition via sputtering also make TeO_2 a versatile and inexpensive material for hybrid integration on silicon and silicon nitride platforms [37–39]. In [40], an erbium-doped tellurium oxide waveguide amplifier pumped at 980 nm was demonstrated with high internal gain exceeding 14 dB and lasing was observed from the end facets, showing the potential for high-performance active on-chip devices in the material. Prior to this work, we have also reported a hybrid TeO_2:Tm^{3+}-Si_3N_4 waveguide amplifier with 7.6 dB internal net gain [41,42] and an erbium-doped tellurium oxide ($TeO_2:Er^{3+}$)-Si_3N_4 amplifier with up to 5 dB gain. We have also demonstrated low-loss waveguides and resonators [39,43] and the prospect for efficient nonlinear devices on the TeO_2-Si_3N_4 platform [12,44]. However, to the best of our knowledge, an integrated tellurite-based laser on a silicon nitride platform had not previously been demonstrated. Here, we report on integrated $TeO_2:Tm^{3+}$-Si_3N_4 microring resonator lasers. We describe the film and waveguide fabrication, design and characterization of the waveguide lasers and show up 4.5 mW single-sided output power at 1828 nm and lasing from 1815–1895 nm for different microring-bus gaps. Such integrated thulium-doped lasers are promising for emerging silicon-nitride-based photonic microsystems operating around 2 µm.

4.2 Design and Fabrication

We fabricated the thulium-doped tellurium oxide waveguide lasers on a silicon nitride platform using a wafer-scale foundry process and a monolithic, reactive co-sputtering post-processing step outlined in [39]. We first deposited a 0.2-µm-thick Si_3N_4 film on a 100-mm silicon wafer with an 8-µm-thick thermal SiO_2 layer using low pressure chemical vapor deposition (LPCVD). The Si_3N_4 layer thickness was chosen as a standard nitride thickness to achieve low-loss, single-mode, and moderate confinement strip waveguides for compact bends in ring resonator structures. Stepper lithography and reactive ion etching were applied to pattern 1.0-µm-wide microring resonators with 300-µm radii, and gaps varying from 0.9 to 1.8 µm between the outer walls of the Si_3N_4 ring and bus waveguide. The wafers were then annealed at high temperature (> 1100 °C) for several hours in N_2 to remove hydrogen from the Si_3N_4 layer and reduce absorption around 1.5 µm wavelength. The silicon nitride wafer was then diced into chips for post-processing.

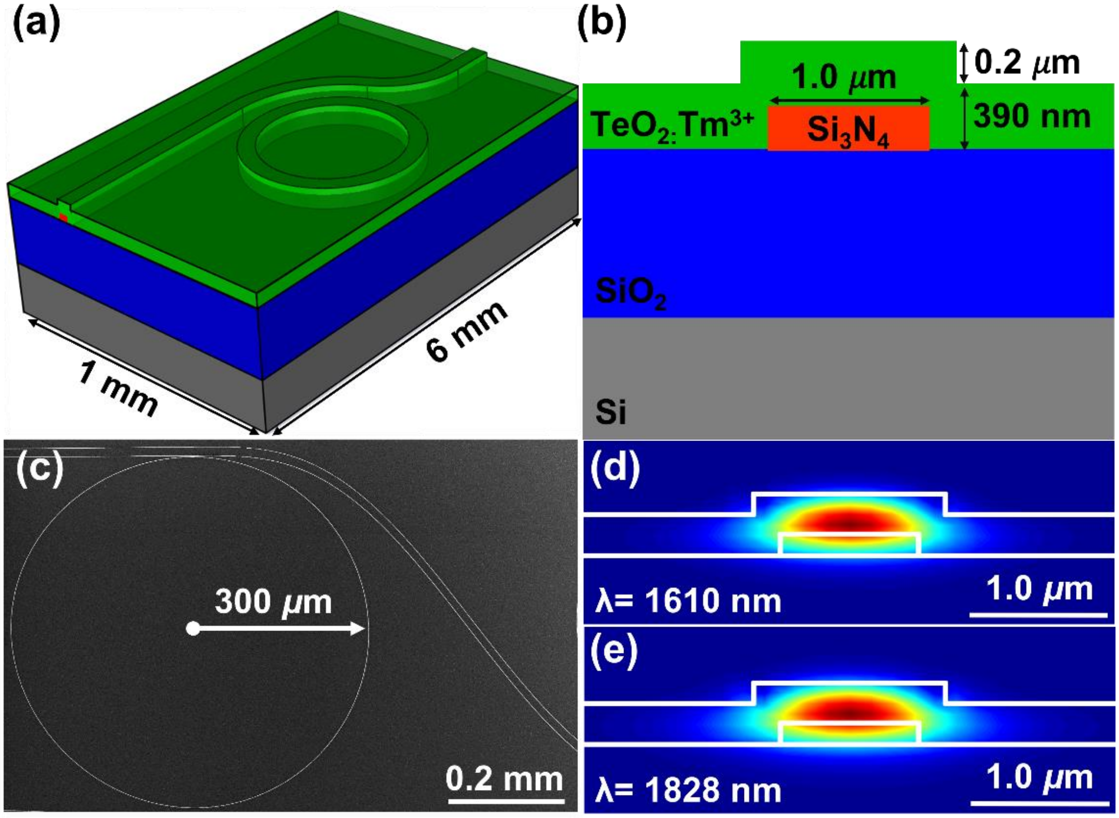

FIGURE 4.1: a) 3D drawing of the $TeO_2:Tm^{3+}$-Si_3N_4 ring laser. b) Cross-section profile of the hybrid waveguide structure. c) Top-view SEM image of a $TeO_2:Tm^{3+}$-Si_3N_4 ring laser. d) Calculated electric field profile of the fundamental TE-polarized mode at 1610 nm pump and 1828 nm laser wavelengths for a silicon nitride strip width and height of 1.0 and 0.2 µm, respectively, and $TeO_2:Tm^{3+}$ film height of 390 nm.

We deposited a 0.39-µm-thick $TeO_2:Tm^{3+}$ coating layer onto the passive silicon nitride chips using a radio frequency (RF) reactive co-sputtering process. Three-inch metallic tellurium and thulium targets with 99.999 and 99.9% purity, respectively, were sputtered in an argon/oxygen atmosphere at ambient temperature. We set the Te and Tm RF sputtering powers to 120 and 85 W, and the Ar and O_2 flow rates to 12 and 7.4 sccm, respectively, at 20°C. The deposition rate for the $TeO_2:Tm^{3+}$ film was 11 nm/min and its refractive index was 2.03 at 638 nm and 1.98 at 1550 nm wavelengths measured by spectroscopic ellipsometry. Thin film propagation losses of ≤ 1.0 dB/cm at 847 nm and ≤ 0.75 dB/cm at 1510 nm were determined using the prism coupling method and a witness sample deposited on a thermally oxidized wafer. We measured a thulium ion dopant concentration of 4.1×10^{20} cm^{-3} using Rutherford backscattering spectrometry (RBS). The thulium concentration was selected to be high enough to achieve greater gain than microring roundtrip losses, including propagation and ring-waveguide coupling losses. We prepared smooth waveguide end facets using focused-ion-beam (FIB) milling. In figure 4.1, we display the microring laser structure. Figures 4.1(a) and 4.1(b) show a 3D drawing of the $TeO_2:Tm^{3+}$-coated Si_3N_4 ring resonator and a cross section diagram of the hybrid waveguide structure, respectively. A scanning electron microscope (SEM) image of the top view of ring resonator and its bus waveguide is shown in figure 4.1(c). The calculated electric field profile of the transverse-electric- (TE-) polarized fundamental mode for the laser wavelength using a finite-element method mode solver is displayed in figure 4.1(d).

The theoretical properties of the $TeO_2:Tm^{3+}$-coated Si_3N_4 ring resonators were investigated using a finite element method (FEM) mode solver. The waveguides were designed to be single mode at > 1500 nm wavelength. Due to the asymmetry of the waveguide structure, simulations show that it only supports the TE-polarized mode. According to the simulation results, approximately 66.7% of the optical power at 1610 nm is confined in the $TeO_2:Tm^{3+}$ coating, with 18.1% confined to the nitride layer with the calculated mode area is 1.2 μm^2, and the rest of the optical power in the SiO_2 and air. At the laser wavelength, 63.3% of the optical power is in the $TeO_2:Tm^{3+}$ coating, with 17.3% confined to the nitride layer, and the rest of the optical power in the SiO_2 and air with a similar mode area of 1.4 μm^2. The hybrid waveguide design was selected to provide good optical confinement in the $TeO_2:Tm^{3+}$ layer while also minimizing both the mode size to enhance intensity and the bend radius for compact rings. The calculated radiation loss and equivalent Q factor for the $TeO_2:Tm^{3+}$-coated silicon nitride microring structure using a finite element bent eigenmode solver, shows that radiation loss is negligible at the selected bend radius of 300 µm [43]. These results show the potential for the fabrication of more compact devices without introducing significant radiation losses.

4.3 Experimental Setup

We characterized the microring lasers using the experimental setup shown in figure 4.2. We coupled pump light from a tunable 1510–1640 nm laser set around 1610 nm and high-power L-band erbium-ytterbium-co-doped fiber amplifier (L-band EYDFA) to the chip via a polarization controller, a 1600/1900 nm fiber wavelength division multiplexor (WDM), and 2-µm spot size tapered optical fiber at 1550-nm wavelength mounted on an xyz stage. The laser output was also coupled from the chip using a lensed fiber with a 2-µm spot size tapered fiber at 1550-nm wavelength, filtered from the pump light with a 1600/1900 nm WDM and coupled to an optical spectrum analyzer (OSA) to observe the output spectrum and power. The transmitted pump light was also measured using a power detector.

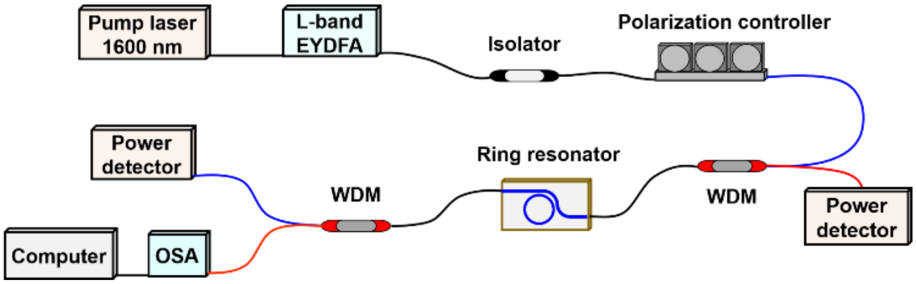

FIGURE 4.2: Experimental setup used for measuring the on-chip thulium-doped microring lasers.

During measurements, the polarization paddles and xyz stages were adjusted to select TE polarization and maximize the transmitted pump/signal intensity. Passive transmission measurements were carried out on the same setup without the L-band EYDFA and the OSA replaced with a photodetector to determine the background waveguide propagation loss. Passive characterization was carried out over the full range of the tunable laser to include wavelengths around 1510 nm, where we observe negligible thulium absorption loss, and the fitted Q factor can be assumed to represent the passive waveguide loss of the structure.

4.4 Results

We measured the transmission properties of the $TeO_2:Tm^{3+}$ coated Si_3N_4 waveguides and ring resonators around the pump wavelength from 1510 nm to 1610 nm. The transmitted pump power for a device with waveguide-resonator gap of 1.1 μm and TE polarization is shown in figure 4.3. We observe decreasing Q factor and lower extinction ratios corresponding to increasing Tm^{3+} ion absorption at wavelengths > ~1550 nm as observed in other host materials [45] (we note that the measurement upper limit was determined by the maximum wavelength of the tunable laser – 1620 nm and the Tm^{3+} absorption peak is around 1650 nm). As displayed in the inset, we observe narrow resonances associated with the fundamental TE mode in the resonator. We performed a best fit of the resonance, assuming a Lorentzian shape of the transmission dip. The quality factor is intrinsically limited by thulium absorption and waveguide propagation loss. As shown in the inset of figure 4.3, the background propagation loss is 0.75 dB/cm at 1519 nm wavelength linked to an internal quality factor of 4.8×10^5 fitted to the resonance spectrum obtained in the under-coupled ring resonator [43]. The fiber-chip coupling loss was determined to be 5.0 dB, influenced by mode mismatch, Fresnel reflections and scattering due to the conformal $TeO_2:Tm^{3+}$ coating on the facet.

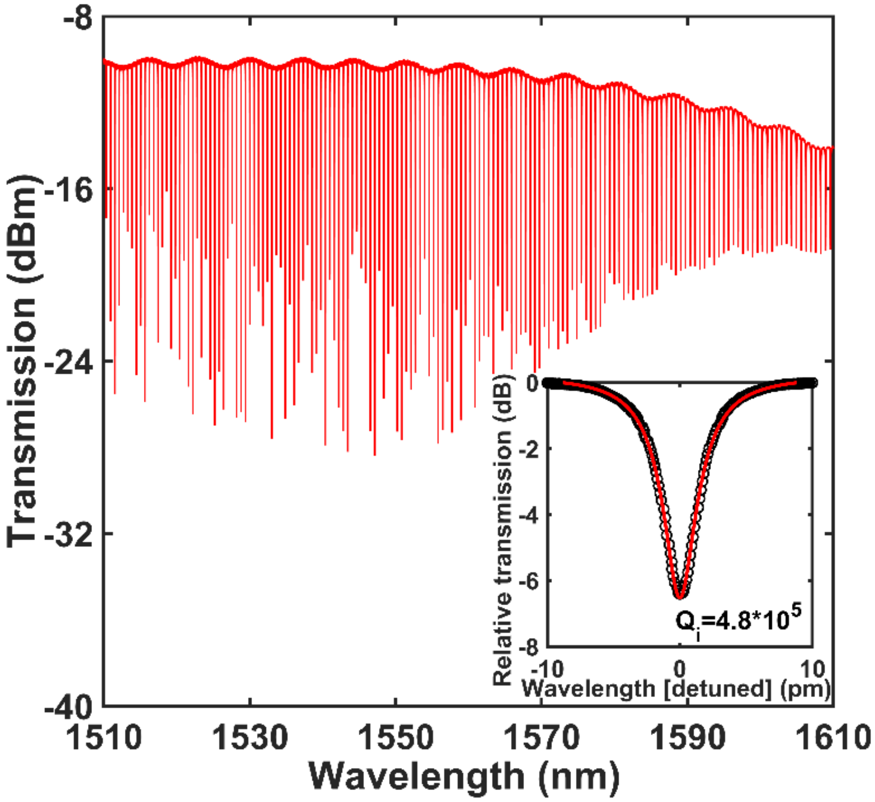

FIGURE 4.3: Transmission measurement in a thulium-doped microring with a microring-waveguide gap of 1.1 μm from 1510 to 1620 nm and for TE polarization. The inset picture shows a zoomed-in view of the resonance at 1519 nm wavelength and fitted Lorentzian function giving an internal Q factor of 4.8×10^5. This corresponds to 0.75 dB/cm waveguide propagation loss at 1519 nm wavelength, which is outside the Tm absorption range and can be taken as the pump background loss.

We resonantly pumped the TeO_2:Tm^{3+}-coated Si_3N_4 ring resonators to investigate their lasing potential, with up to 60 mW power launched into the bus waveguide. We determined the launched pump power by measuring the incident power from the input fiber using an integrating sphere photodiode power monitor and accounting for 5.0 dB fiber-chip coupling loss. As shown in figure 4.4, we observe multimode lasing around 1828 nm for thulium-doped laser with a gap of 1.1 μm at 1610 nm pump wavelength. The laser output is bidirectional and a similar output power was observed at the pump input side of the chip. Single mode laser emission was also observed in the resonator with up to 3.6 mW single-sided on-chip power and 7.2 mW double-sided output power, when the pump wavelength was shifted to 1600 nm, as shown in the inset of figure 4.4. We observed single mode laser emission for pump wavelengths from 1590 to 1604 nm where the thulium absorption is not as high as the thulium absorption around the peak. When pumping at wavelengths from 1604 to 1620 nm, where the thulium absorption is high, we observed multimode lasing with higher output powers in the device.

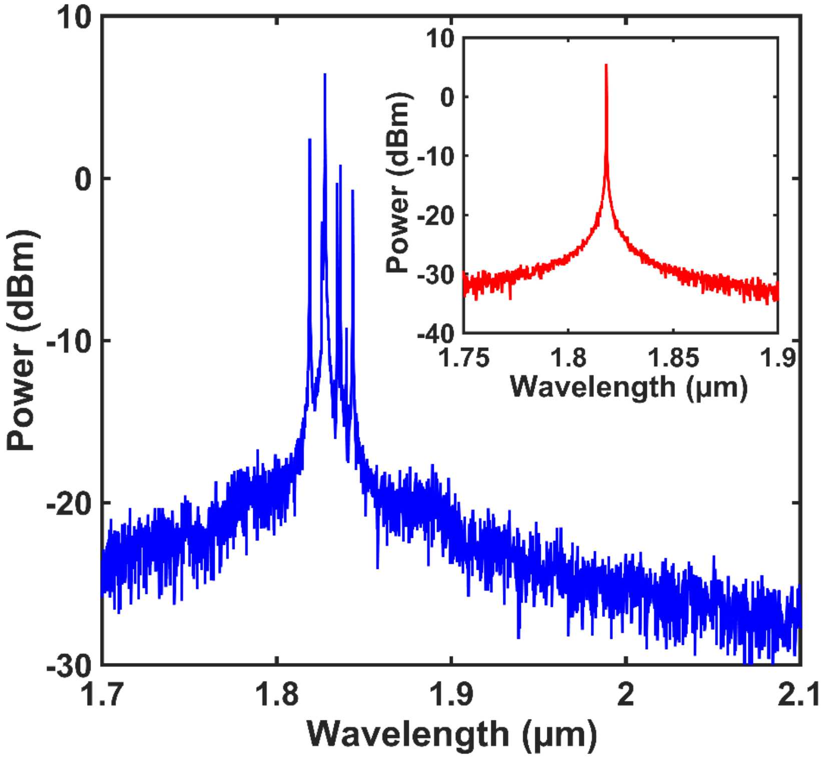

FIGURE 4.4: Multimode laser emission spectrum of a $TeO_2:Tm^{3+}$-coated Si_3N_4 ring resonator under 1610-nm pumping at a microring-waveguide gap of 1.1 µm obtained with ~60 mW on-chip pump power. The inset picture shows single mode laser emission of the same $TeO_2:Tm^{3+}$-coated Si_3N_4 ring resonator pumped at 1600 nm.

We observed the highest output power and laser efficiency for the device with gap of 1.1 µm and for a pump wavelength of 1610 nm. Figure 4.5 shows the single-sided laser output power of up to 4.5 mW measured as a function of on-chip and absorbed pump power. The on-chip power is the power coupled into the silicon nitride bus waveguide, taking into account the fiber-chip coupling loss of ~5.0 dB per facet, and the absorbed power is the power coupled into the resonator. We note that the laser output power also includes a small amount of amplification in the $TeO_2:Tm^{3+}$-coated bus waveguide (we measured a peak internal net gain of up to 1.4 dB in the 0.6 cm long straight waveguide at 1870 nm for 60 mW launched power [41]). We observe the lowest device threshold of 18 mW versus on-chip launched pump power at a gap of 1.1 µm to the bus waveguide and 11 mW as the threshold pump power in the ring resonator. We observe slope efficiencies of 11% and 17% in the ring laser, respectively. Considering bidirectional emission, we observe 9 mW total on-chip output power and a slope efficiency versus absorbed pump power of 34%.

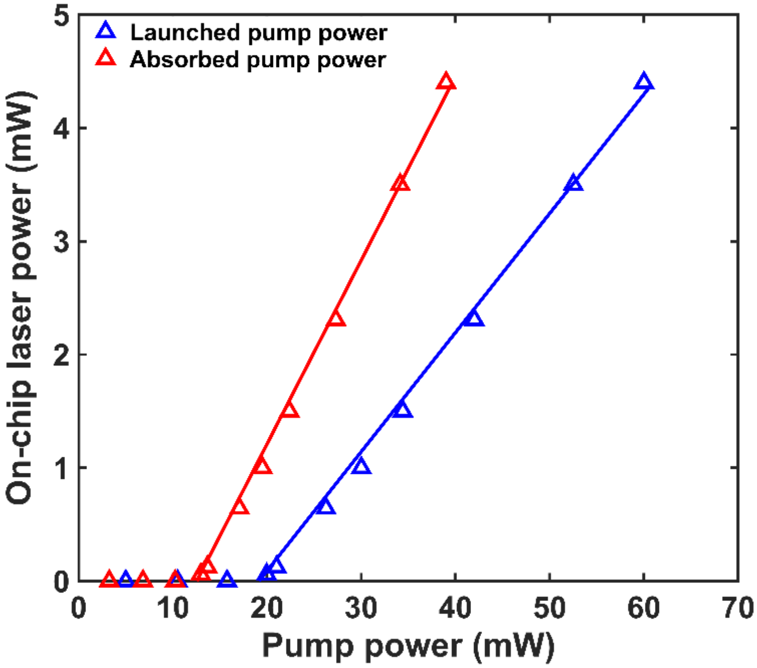

FIGURE 4.5: Tm^{3+} laser curves for a microring resonator with a gap of 1.1 μm, showing a maximum on-chip output power of up to 4.5 mW and slope efficiencies of 11% and 17% versus launched and absorbed pump power.

In figure 4.6 we show the laser spectra obtained under 1610-nm pumping and at different gaps of 0.9, 1.1, 1.4, 1.6 and 1.8 μm. We observe multi-mode lasing and laser modes spanning from 1815 to 1895 nm. For smaller gap sizes (and longer wavelengths), the ring resonator modes incur greater coupling losses, favoring lasing closer to the thulium gain peak around 1800 nm, while, for larger gap sizes, the laser output shifts to longer wavelengths where the Tm^{3+} absorption is lower, and population inversion is more easily achieved. Therefore, by pumping different gaps, different lasing wavelengths can be achieved. The laser performance can be enhanced, and emission wavelength can be controlled by engineering the pump and signal coupling using, for example, Mach-Zehnder couplers [45]. Furthermore, by building on this demonstration of a $TeO_2:Tm^{3+}$ integrated laser and silicon nitride's versatile and high-resolution wafer-scale fabrication, various laser cavity designs of interest can be explored, including DBR, DFB and tunable lasers. In addition to thulium devices, different rare earth dopants can be investigated for lasing at a wide variety of wavelengths on the hybrid tellurite glass-silicon nitride platform.

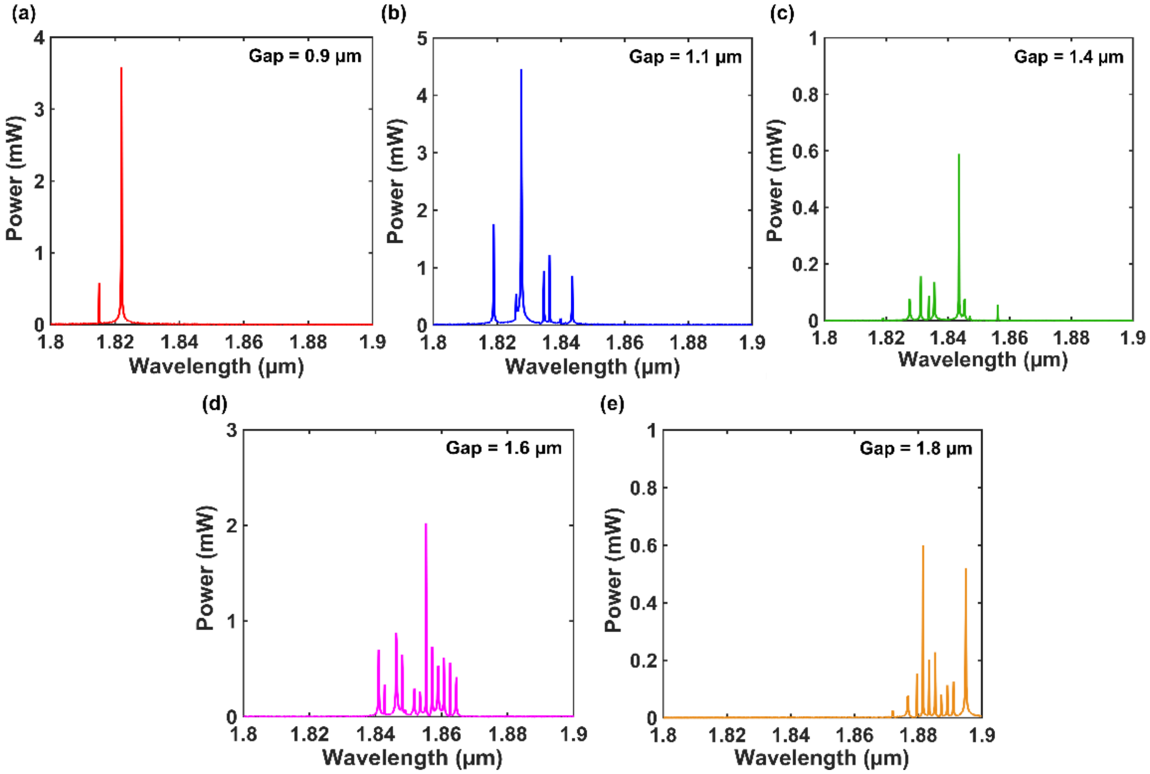

FIGURE 4.6: Laser emission spectra of $TeO_2:Tm^{3+}$-Si_3N_4 ring resonators under 1610-nm pumping and for microring-waveguide gaps of a) 0.9 µm b) 1.1 µm, c) 1.4 µm, d) 1.6 µm and e) 1.8 µm. The laser emission shifts from ~1815 to 1895 nm by increasing the gap size.

4.5 Investigation of $TeO_2:Tm^{3+}$-Si_3N_4 Microring Lasers with Different Tm^{3+} Concentrations

The thulium concentration of 4.1×10^{20} cm^{-3} was selected as an optimized thulium concentration to have the highest slope efficiency and the lowest threshold pump power launched into the bus waveguide [47,48]. To study more about the influence of thulium concentration on laser performance, similar devices are fabricated where the Tm RF sputtering powers are set to 80 and 100 W. The refractive index was 2.03, and 2.02 at 638 nm and 1.98 and 1.96 at 1550 nm wavelengths, respectively, measured by spectroscopic ellipsometry with thulium ion dopant concentrations of 3.6×10^{20} cm^{-3} and 5.9×10^{20} cm^{-3}, respectively, measured by RBS. Similar passive and laser experiments were carried out on these chips as those described in sections 4.3 and 4.4. The properties of the ring lasers with the best performance on each chip are compared in table 4.1.

TABLE 4.1: Comparison of the properties of $TeO_2:Tm^{3+}$-coated Si_3N_4 ring lasers with different thulium concentrations.

Tm^{3+} concentration (atom/cm^3)	3.6×10^{20}	4.1×10^{20}	5.9×10^{20}
Radius (μm)	300	300	300
Gap (μm)	1.0	1.1	1.1
$TeO_2:Tm^{3+}$ thickness (nm)	372	390	302
Intrinsic Q factor	4.1×10^5	4.8×10^5	3.6×10^5
Background propagation loss (dB/cm)	0.9	0.75	1.1
Maximum laser slope efficiency	5%	11%	8%
Ring slope efficiency	6%	17%	14%
Minimum laser threshold (mW)	25	18	53.4
Ring threshold (mW)	21	11	29.9

The transmission properties are measured of the $TeO_2:Tm^{3+}$-coated Si_3N_4 waveguides and ring resonators with thulium concentrations of 3.6×10^{20} cm^{-3} and 5.9×10^{20} cm^{-3} around the pump wavelength from 1510 nm to 1610 nm. They exhibited internal quality factors of 4.1×10^5 and 3.6×10^5 at 1529.2 nm and 1513.1 nm, respectively, corresponding to 0.9 dB/cm and 1.1 dB/cm background propagation losses, respectively [49,50]. As shown in figure 4.7, multimode lasing is observed around 1818 nm for a thulium-doped laser with the thulium concentration of 3.6×10^{20} cm^{-3} in a gap size of 1.0 μm pumped at 1610 nm wavelength. The laser output is bidirectional with the single-sided output power of up to 4.3 mW for an on-chip pump power of 117 mW and laser slope efficiency of 5% with respect to power launched into the bus waveguide. Similar output power was observed at the pump input side of the chip. In figure 4.8 the laser spectra is shown obtained for the same chip under 1610-nm pumping and at different gaps of 1.0, 1.3, and 1.4 μm.

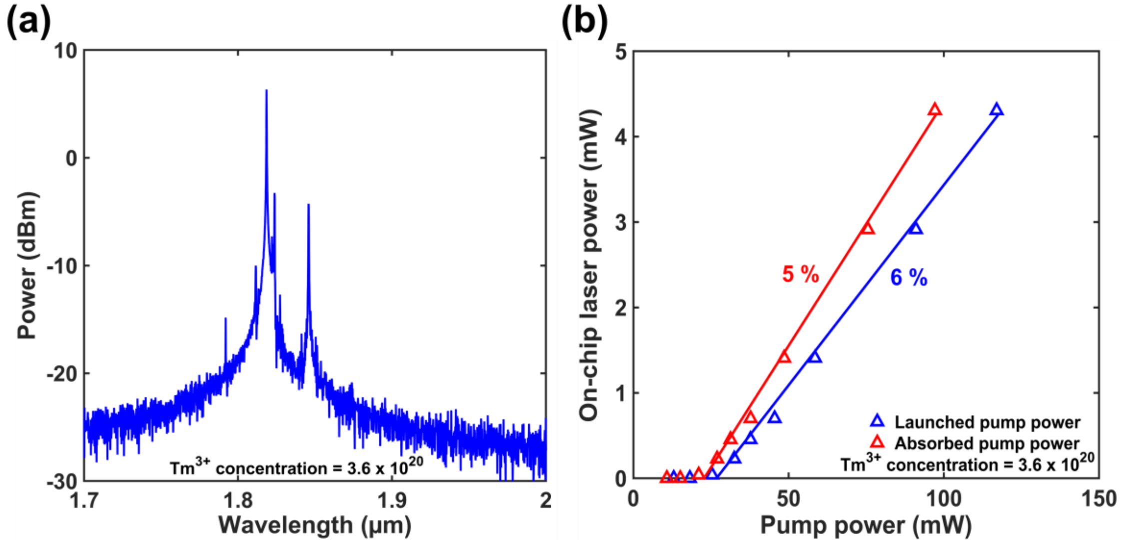

FIGURE 4.7: a) Multimode laser emission spectrum of a TeO$_2$:Tm^{3+}-coated Si$_3$N$_4$ ring resonator under 1610-nm pumping at a microring-waveguide gap of 1.0 μm obtained with ~117 mW on-chip pump power for thulium concentration of 3.6 × 10^{20} cm^{-3}. b) Tm^{3+} laser curves for a microring resonator with a gap of 1.0 μm, showing a maximum on-chip output power of up to 4.3 mW and slope efficiencies of 5% and 6% versus launched and absorbed pump power.

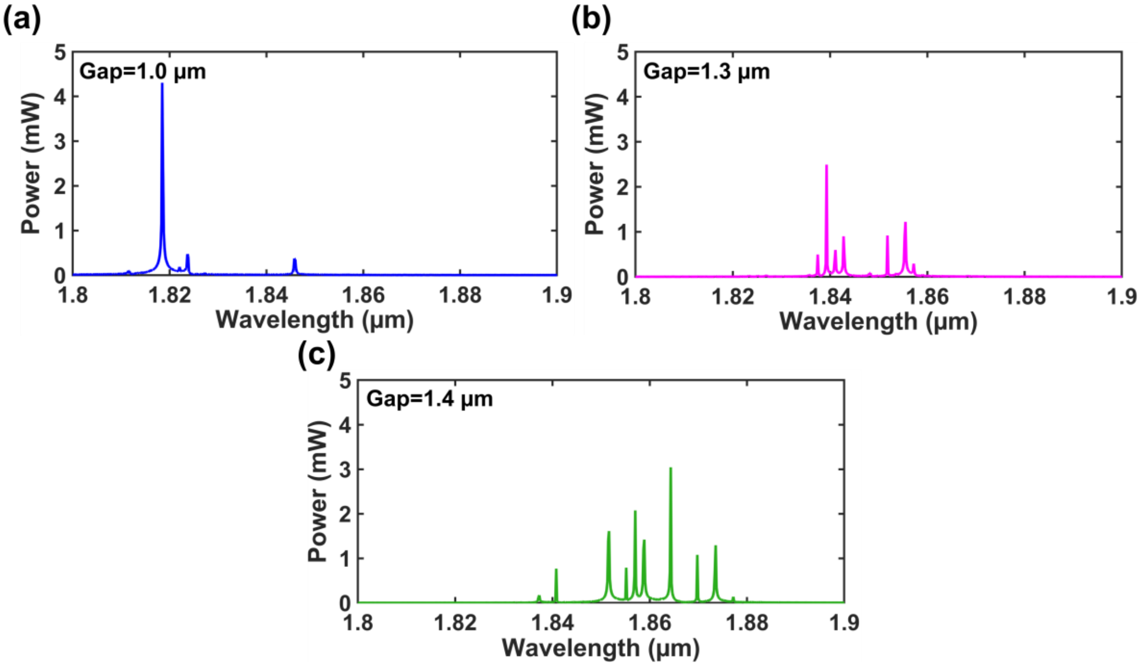

FIGURE 4.8: Laser emission spectra of TeO$_2$:Tm^{3+}-Si$_3$N$_4$ ring resonators under 1610-nm pumping and for microring-waveguide gaps of a) 1.0 μm b) 1.3 μm, c) 1.4 μm. The laser emission shifts from ~1815 to 1878 nm by increasing the gap size.

Multimode lasing is observed around 1843 nm for a thulium-doped laser with the thulium concentration of 5.9 × 10^{20} cm^{-3} and a gap size of 1.1 μm pumped at 1610 nm wavelength. The laser output is bidirectional with the single-sided on-chip output power of up to 7.9 mW for an on-chip pump power of 163 mW and laser slope efficiency of 8% with respect to power launched into the bus waveguide. In figure 4.10, the laser spectra obtained under 1610-nm pumping and at different gaps of 1.1, 1.3, and 1.8 μm. We observe multi-mode lasing and laser modes spanning from 1825 to 1896 nm.

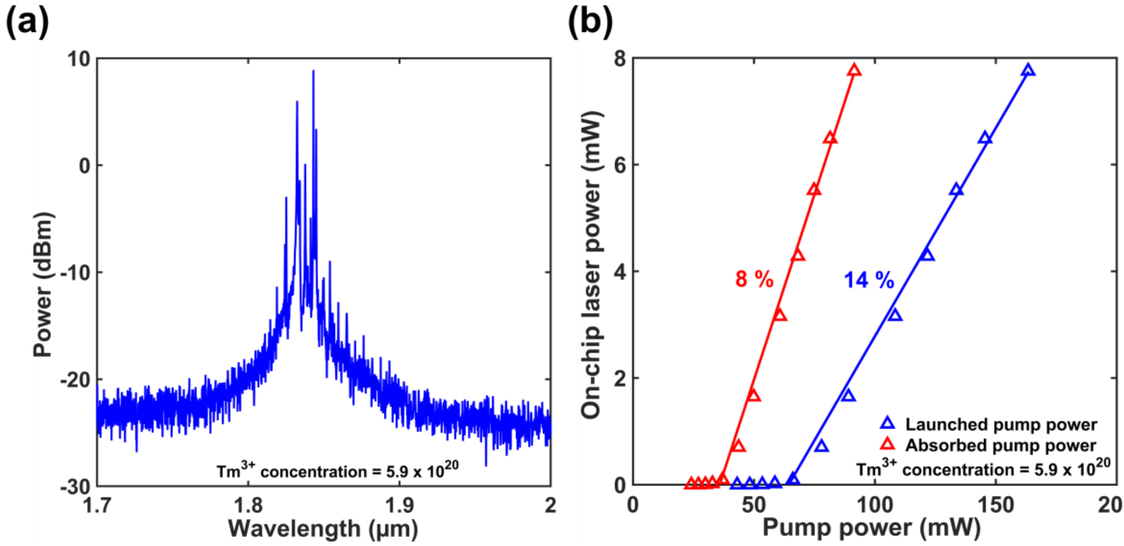

FIGURE 4.9: a) Multimode laser emission spectrum of a TeO_2:Tm^{3+}-coated Si_3N_4 ring resonator under 1610-nm pumping at a microring-waveguide gap of 1.1 μm obtained with ~163 mW on-chip pump power for thulium concentration of 5.9 × 10^{20} cm^{-3}. b) Tm^{3+} laser curves for a microring resonator with a gap of 1.1 μm, showing a maximum on-chip output power of up to 7.9 mW and slope efficiencies of 8% and 14% versus launched and absorbed pump power.

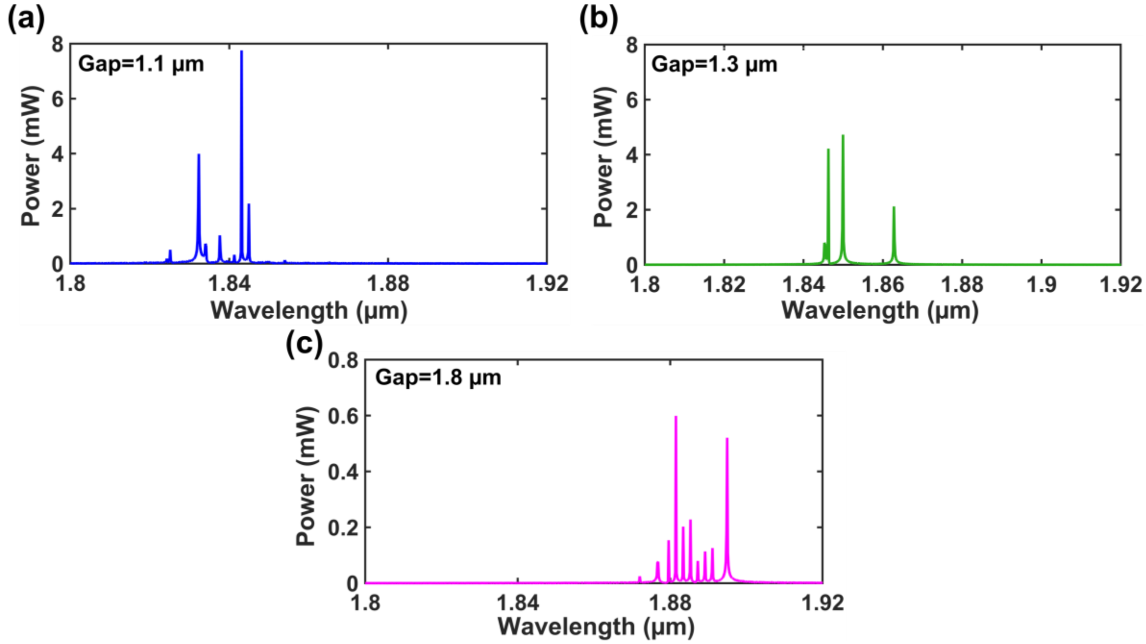

FIGURE 4.10: Laser emission spectra of TeO_2:Tm^{3+}-Si_3N_4 ring resonators under 1610-nm pumping and for microring-waveguide gaps of a) 1.1 µm b) 1.3 µm, c) 1.8 µm. The laser emission shifts from ~1825 to 1896 nm by increasing the gap size.

While the background propagation losses are almost the same, the output powers and slope efficiency for the TeO^2:Tm^{3+} microring laser with a thulium concentration of 4.1 x 10^{20} atom/cm^{3+} is higher than the other two concentrations. These laser results on different chips show the consistent performance and high quality of the TeO_2:Tm^{3+}-Si_3N_4 hybrid platform and provide a guide for future work on optimization of integrated thulium lasers.

4.6 Conclusion

In summary, we have demonstrated thulium-doped tellurium oxide microring resonator lasers emitting at wavelengths from 1815–1895 nm on a silicon nitride chip. We measure a minimum threshold of 18 (11) mW and maximum slope efficiency of 11% (17%) with respect to on-chip (absorbed) pump power. In the future, optimizing the coupler and cavity designs and waveguide cross-section can lead to efficient and low threshold laser emission over a wider wavelength range across thulium's broad gain spectrum ($\sim 1.7 - 2.1$ µm). Such devices are promising for ultra-compact light sources for silicon-based photonic microsystems in the emerging 2-µm optical communications and sensing band.

Bibliography

[1] K. Scholle, S. Lamrini, P. Koopmann, and P. Fuhrberg, "2 µm laser sources and their possible applications," *Frontiers in Guided Wave Optics and Optoelectronics* (InTech, 2010).

[2] Q. Wang, J. Geng, and S. Jiang, "2-µm fiber laser sources for sensing," *Opt. Eng.* **53**(6), 061609 (2014).

[3] M. Ebrahim-Zadeh, G. Leo, and I. Sorokina, "Mid-infrared coherent sources and applications: introduction," *J. Opt. Soc. Am. B* **35**(12), MIC1–MIC1 (2018).

[4] R. Soref, "Enabling 2 µm communications," *Nat. Photonics* **9**(6), 358–359 (2015).

[5] F. C. Garcia Gunning, N. Kavanagh, E. Russell, R. Sheehan, J. O'Callaghan, and B. Corbett, "Key enabling technologies for optical communications at 2000 nm," *Appl. Opt.* **57**(22), E64–E70 (2018).

[6] D. J. Thomson, L. Shen, J. J. Ackert, E. Huante-Ceron, A. P. Knights, M. Nedeljkovic, A. C. Peacock, and G. Z. Mashanovich, "Optical detection and modulation at 2µm-2.5µm in silicon," *Opt. Express* **22**(9), 10825–10830 (2014).

[7] J. J. Ackert, D. J. Thomson, L. Shen, A. C. Peacock, P. E. Jessop, G. T. Reed, G. Z. Mashanovich, and A. P. Knights, "High-speed detection at two micrometres with monolithic silicon photodiodes," *Nat. Photonics* **9**(6), 393–396 (2015).

[8] W. Cao, D. Hagan, D. J. Thomson, M. Nedeljkovic, C. G. Littlejohns, A. Knights, S. Alam, J. Wang, F. Gardes, W. Zhang, S. Liu, K. Li, M. Said Rouifed, G. Xin, W. Wang, H. Wang, G. T. Reed, and G. Z. Mashanovich, "High-speed silicon modulators for the 2 μm wavelength band," *Optica* **5**(9), 1055–1062 (2018).

[9] D. J. Blumenthal, R. Heideman, D. Geuzebroek, A. Leinse, and C. Roeloffzen, "Silicon nitride in silicon photonics," *Proc. IEEE* **106**(12), 2209–2231 (2018).

[10] J. Mu, M. Dijkstra, J. Korterik, H. Offerhaus, and S. M. García-Blanco, "High-gain waveguide amplifiers in Si_3N_4 technology via double-layer monolithic integration," *Photon. Res.* **8**(10), 1634–1641 (2020).

[11] L. Gaeta, M. Lipson, and T. J. Kippenberg, "Photonic-chip-based frequency combs," *Nat. Photonics* **13**(3), 158–169 (2019).

[12] K. Miarabbas Kiani, H. M. Mbonde, H. C. Frankis, R. Mateman, A. Leinse, A. P. Knights, and J. D. B. Bradley, "Four-wave mixing in high-Q tellurium-oxide-coated silicon nitride microring resonators," *OSA Continuum* **3**(12), 3497–3507 (2020).

[13] J. F. Bauters, M. J. R. Heck, D. D. John, J. S. Barton, C. M. Bruinink, A. Leinse, R. G. Heideman, D. J. Blumenthal, and J. E. Bowers, "Planar waveguides with less than 0.1 dB/m propagation loss fabricated with wafer bonding," *Opt. Express* **19**(24), 24090–24101 (2011).

[14] J. P. Epping, M. Hoekman, R. Mateman, A. Leinse, R. G. Heideman, A. van Rees, P. J.M. van der Slot, C. J. Lee, and K-J. Boller, "High confinement, high yield Si_3N_4 waveguides for nonlinear optical applications," *Opt. Express* **23**(2), 642–648 (2015).

[15] E. Kasper, M. Kittler, M. Oehme, and T. Arguirov, "Germanium tin: silicon photonics toward the mid-infrared [Invited]," *Photon. Res.* **1**(2), 69–76 (2013).

[16] G. Roelkens, U. D. Dave, A. Gassenq, N. Hattasan, C. Hu, B. Kuyken, F. Leo, A. Malik, M. Muneeb, E. Ryckeboer, D. Sanchez, S. Uvin, R. Wang, Z. Hens, R. Baets, Y. Shimura, F. Gencarelli, B. Vincent, R. Loo, J. Van Campenhout, L. Cerutti, J.-B. Rodriguez, E. Tourni´e, X. Chen, M. Nedeljkovic, G. Mashanovich, L. Shen, N. Healy, A. C. Peacock, X. Liu, and R. Osgood, "Silicon-based photonic integration beyond the telecommunication wavelength range," *IEEE J. Sel. Top. Quantum Electron.* **20**(4), 8201511 (2014).

[17] A. Elbaz, D. Buca, N. Driesch, K. Pantzas, G. Patriarche, N. Zerounian, E. Herth, X. Checoury, S. Sauvage, I. Sagnes, A. Foti, R. Ossikovski, J.-M. Hartmann, F. Boeuf, Z. Ikonic, P. Boucaud, D. Grützmacher, and M. El Kurdi, "Ultra-low-threshold continuous-wave and pulsed lasing in tensile-strained GeSn alloys," *Nat. Photonics* **14**(6), 375–382 (2020).

[18] N. J. Ramírez-Martínez, M. Núñez-Velázquez, A. A. Umnikov, and J. K. Sahu, "Highly efficient thulium-doped high-power laser fibers fabricated by MCVD," *Opt. Express* **27**(1), 196–201 (2019).

[19] S. V. Muravyev, E. A. Anashkina, A. V. Andrianov, V. V. Dorofeev, S. E. Motorin, M. Y. Koptev, and A. V. Kim, “Dual-band Tm^{3+}-doped tellurite fiber amplifier and laser at 1.9 μm and 2.3 μm,” *Sci. Rep.* **8**, 16164 (2018).

[20] S. D. Jackson, “Towards high-power mid-infrared emission from a fibre laser,” *Nat. Photonics* **6**(7), 423–431 (2012).

[21] A. S. K. Tong, C. J. Mitchell, A. Aghajani, N. Sessions, G. S. Murugan, J. I. Mackenzie, and J. S. Wilkinson, “Spectroscopy of thulium-doped tantalum pentoxide waveguides on silicon,” *Opt. Mater. Express* **10**(9), 2201–2211 (2020).

[22] Z. Su, N. Li, E. Salih Magden, M. Byrd, Purnawirman, T. N. Adam, G. Leake, D. Coolbaugh, J. D. B. Bradley, and M. R. Watts, “Ultra-compact and low-threshold thulium microcavity laser monolithically integrated on silicon,” *Opt. Lett.* **41**(24), 5708–5711 (2016).

[23] N. Li, Purnawirman, Z. Su, E. S. Magden, P. T. Callahan, K. Shtyrkova, M. Xin, A. Ruocco, C. Baiocco, E. P. Ippen, F. X. Kärtner, J. D. B. Bradley, D. Vermeulen, and M. R. Watts, “High-power thulium lasers on a silicon photonics platform,” *Opt. Lett.* **42**(6), 1181–1184 (2017).

[24] K. Shtyrkova, P. T. Callahan, N. Li, E. S. Magden, A. Ruocco, D. Vermeulen, F. X. Kärtner, M. R. Watts, and Erich P. Ippen, “Integrated CMOS-compatible Q-switched mode-locked lasers at 1900nm with an on-chip artificial saturable absorber,” *Opt. Express* **27**(3), 3542–3556 (2019).

[25] F. D. Trapani, X. Mateos, V. Petrov, A. Agnesi, U. Griebner, H. Zhang, J. Wang and H. Yu, “Continuous-wave laser performance of Tm: $LuVO_4$ under Ti:sapphire laser pumping,” *Laser Physics.* **24**(3), 035806 (2014).

[26] M. George, “Ti: Tm: $LiNbO_3$ waveguide amplifiers and lasers,” Ph.D. Thesis (University of Paderborn, Germany, 2012).

[27] M. Pollnau and J. D. B. Bradley, “Optically pumped rare-earth-doped Al_2O_3 distributed-feedback lasers on silicon [Invited],” *Opt. Express* **26**(18), 24164–24189 (2018).

[28] S. Li, D. Zhang, J. Zhao, Q. Yang, X. Xiao, S. Hu, L. Wang, M. Li, X. Tang, Y. Qiu, M. Luo, and S. Yu, “Silicon micro-ring tunable laser for coherent optical communication,” *Opt. Express* **24**(6), 6341–6349 (2016).

[29] F. Kish, V. Lal, P. Evans, S. W. Corzine, M. Ziari, T. Butrie, M. Reffle, H. S. Tsai, A. Dentai, J. Pleumeekers, M. Missey, M. Fisher, S. Murthy, R. Salvatore, P. Samra, S. Demars, N. Kim, A. James, A. Hosseini, P. Studenkov, M. Lauermann, R. Going, M. Lu, J. Zhang, J. Tang, J. Bostak, T. Vallaitis, M. Kuntz, D. Pavinski, A. Karanicolas, B. Behnia, D. Engel, O. Khayam, N. Modi, M. R. Chitgarha, P. Mertz, W. Ko, R, Maher, J. Osenbach, J. T. Rahn, H. Sun, K. T. Wu, M. Mitchell, and D. Welch, “System-on-chip photonic integrated circuits,” *IEEE J. Sel. Top. Quantum Electron.* **24**(1), 6100120 (2018).

[30] M. Ahmadi, W. Shi, and S. LaRochelle, “Widely tunable silicon Raman laser,” *Optica* **8**(6), 804–810 (2021).

[31] N. Li, D. Vermeulen, Z. Su, E. Salih Magden, M. Xin, N. Singh, A. Ruocco, J. Notaros, C. V. Poulton, E. Timurdogan, C. Baiocco, and M. R. Watts, “Monolithically

integrated erbium-doped tunable laser on a CMOS-compatible silicon photonics platform," *Opt. Express* **26**(13), 16200–16211 (2018).

[32] K. van Dalfsen, S. Aravazhi, C. Grivas, S. M. García-Blanco, and M. Pollnau, "Thulium channel waveguide laser in a monoclinic double tungstate with 70% slope efficiency," *Opt. Lett.* **37**(5), 887–889 (2012).

[33] E. Kifle, P. Loiko, U. Griebner, V. Petrov, P. Camy, A. Braud, M. Aguiló, F. Díaz, and X. Mateos, "Diamond saw dicing of thulium channel waveguide lasers in monoclinic crystalline films," *Opt. Lett.* **44**(7), 1596–1599 (2019).

[34] A. Jha, B. D. O. Richards, G. Jose, T. T. Fernandez, C. J. Hill, J. Lousteau, and P. Joshi, "Review on structural, thermal, optical and spectroscopic properties of tellurium oxide-based glasses for fibre optic and waveguide applications," *Int. Mater. Rev.* **57**(6), 357–382 (2012).

[35] S. Shen, A. Jha, X. Liu, M. Naftaly, K. Bindra, H. J. Bookey, and A. K. Kar, "Tellurite glasses for broadband amplifiers and integrated optics," *J. Am. Ceram. Soc.* **85**(6), 1391–1395 (2002).

[36] K. Vu and S. Madden, "Tellurium dioxide erbium doped planar rib waveguide amplifiers with net gain and 2.8dB/cm internal gain," *Opt. Express* **18**(18), 19192–19200 (2010).

[37] R. Nayak, V. Gupta, A. L. Dawar, and K. Sreenivas, "Optical waveguiding in amorphous tellurium oxide thin films," *Thin Solid Films* **445**(1), 118–126 (2003).

[38] S. J. Madden and K. T. Vu, “Very low loss reactively ion etched tellurium dioxide planar rib waveguides for linear and non-linear optics,” *Opt. Express* **17**(20), 17645–17651 (2009).

[39] H. C. Frankis, K. Miarabbas Kiani, D. B. Bonneville, C. Zhang, S. Norris, R. Mateman, A. Leinse, N. D. Bassim, A. P. Knights, and J. D. B. Bradley, “Low-loss TeO_2-coated Si_3N_4 waveguides for application in photonic integrated circuits,” *Opt. Express* **27**(9), 12529–12540 (2019).

[40] K. Vu, S. Farahani, and S. Madden, “980nm pumped erbium doped tellurium oxide planar rib waveguide laser and amplifier with gain in S, C and L band,” *Opt. Express* **23**(2), 747–755 (2015).

[41] K. Miarabbas Kiani, H. C. Frankis, H. M. Mbonde, R. Mateman, A. Leinse, A. P. Knights, and J. D. B. Bradley, “Thulium-doped tellurium oxide waveguide amplifier with 7.6 dB net gain on a silicon nitride chip,” *Opt. Lett.* **44**(23), 5788–5791 (2019).

[42] K. Miarabbas Kiani, H. Frankic, R. Mateman, A. Leinse, A. P. Knights and J. D. B. Bradley, “High gain thulium-doped tellurium oxide waveguide amplifier for optical communication in the 2 µm window,” *2021 Photonics North (PN)*, 1-1 (2021).

[43] H. C. Frankis, K. Miarabbas Kiani, D. Su, R. Mateman, A. Leinse, and J. D. B. Bradley, “High-Q tellurium-oxide-coated silicon nitride microring resonators,” *Opt. Lett.* **44**(1), 118–121 (2019).

[44] N. Singh, H. M. Mbonde, H. C. Frankis, E. Ippen, J. D. B. Bradley, and F. X. Kärtner, “Nonlinear silicon photonics on CMOS-compatible tellurium oxide,” *Photon. Res.* **8**(12), 1904–1909 (2020).

[45] G. Huber, C. Kränkel, and K. Petermann, “Solid-state lasers: status and future,” *J. Opt. Soc. Am. B* **27**(11), B93–B105 (2010).

[46] L. Chang, M. de Goede, M. Dijkstra, C. I. van Emmerik, and S. M. García-Blanco, “Modular microring laser cavity sensor,” *Opt. Express* **29**(2), 1371–1383 (2021).

[47] K. Miarabbas Kiani, H. C. Frankis, R. Mateman, A. Leinse, A. P. Knights, and J. D. B. Bradley, “Thulium-doped tellurium oxide microring lasers integrated on a low-loss silicon nitride platform,” *Opt. Mater. Express* **11**, 3656-3665 (2021).

[48] K. Miarabbas Kiani, H. C. Franki, R. Mateman, A. Leinse, A. P. Knights, and J. D. B. Bradley, “Thulium-doped tellurium oxide laser for optical communication at 2-µm window,” in *Conference on Lasers and Electro-Optics, OSA,* SM1A.6 (2021).

[49] K. Miarabbas Kiani, D. B. Bonneville, A. P. Knights and J. D. B. Bradley, “High-Q-factor tellurium oxide clad silicon microring resonators,” *2021 IEEE 17th International Conference on Group IV Photonics (GFP)*, 1-2 (2021).

[50] K. Miarabbas Kiani, D. B. Bonneville, A. P. Knights, and J. D. B. Bradley, “High-*Q* TeO_2–Si hybrid microring resonators,” *Appl. Sci.* **12**, 1363 (2022).

Chapter 5

High-*Q* TeO_2-Si Hybrid Microring Resonators

Preface

The following chapter presents the integration of low loss (high quality factor) tellurium oxide (TeO_2) coated silicon microring resonators on silicon photonic chips. The loss mechanisms are crucial in the design of silicon photonic devices, particularly the on-chip optically pumped lasers investigated in this thesis, since the laser efficiency depends on the pump light loss and coupling into the resonator and the round-trip laser loss. Three different microring resonator designs with different cladding layers including tellurium oxide, silicon oxide, and air were designed, fabricated, and measured. The silicon microring structure was fabricated in the Advanced Micro Foundry (AMF) in Singapore and a radio frequency (RF) magnetron sputtering system in the Centre for Emerging Device Technologies (CEDT) at McMaster University was used to deposit tellurium oxide (TeO_2) onto the silicon microrings to achieve a low loss silicon platform. This approach on tellurium oxide-coated silicon microring resonators enables a photonic platform that can combine tellurium oxide's promising passive, active and nonlinear optical material properties for the fabrication of high-performance rare earth doped active devices such as amplifiers and lasers as well as low-loss passive and nonlinear devices in silicon photonic platforms.

An introduction and the motivation for integrated tellurium oxide cladded silicon microring resonators are given in section 5.1. Section 5.2 describes the design, fabrication, and structure of uncoated and SiO_2- and TeO_2 -coated silicon microring resonators. The calculated optical properties of these three silicon microrings platforms are summarized using a finite element bent eigenmode solver. In section 5.3, the transmission properties of the uncladded and cladded silicon microring resonators are characterized to determine their quality factors and the losses using a fiber-chip coupling setup. The scattering loss is calculated as a function of wavelength for microring resonators with air, SiO_2, and TeO_2 claddings based on the 3D Payne-Lacey model, and the model is shown to agree with the experimental results. The main results are summarized, and conclusions are given in section 5.4.

High-Q TeO_2–Si hybrid microring resonators

Khadijeh Miarabbas Kiani, Dawson B. Bonneville, Andrew P. Knights, and Jonathan D. B. Bradley

McMaster University, 1280 Main Street West, Hamilton, ON, Canada

This paper was published in Applied Sciences on January 27, 2022.

DOI: 10.3390/app12031363

Abstract

We present the design and experimental measurement of tellurium-oxide-clad silicon microring resonators with internal *Q* factors of up to 1.5×10^6, corresponding to a propagation loss of 0.42 dB/cm at wavelengths around 1550 nm. This compares to propagation loss of 3.4 dB/cm for unclad waveguides and 0.97 dB/cm for waveguides clad with SiO_2. We compare our experimental results with the Payne-Lacey model describing propagation dominated by sidewall scattering. We conclude that the relative increase in refractive index of the TeO_2 reduces scattering sufficiently to account for the low propagation loss. These results, in combination with the promising optical properties of TeO_2, provide a further step towards realizing compact, monolithic, and low loss passive, nonlinear and rare-earth-doped active integrated photonic devices on a silicon photonic platform.

5.1 Introduction

The impact of silicon photonics on the development of photonic integrated circuits (PICs) is considerable, because of device compatibility with complementary metal-oxide-semiconductor (CMOS) technology and the leveraging of decades of research stimulated by the microelectronics industry [1]. The miniaturization of photonic waveguides has emerged as one of the most prominent technology platforms for PICs over the past few decades [2].

The reduction of propagation loss associated with silicon waveguides is an ongoing research area because loss is a key parameter for link budget management in on-chip optical networks and many important micro-photonic devices, and passive and active systems including sensors, filters, delay lines, and light sources [3-6]. One device structure for which propagation loss is particularly critical is the microring resonator (MRR). The MRR provides an efficient cavity that has a compact size, wavelength selectivity, tunability, scalability, and functional versatility [7], making it a prominent candidate for a variety of applications including lasers [8,9], optical sensors [10], nonlinear optics [11,12], quantum optics [13], (de-)multiplexing systems [14], optical filters [15], and optical modulators [16]. The loss in MRRs can be quantified by the cavity *Q* factor, which is typically limited to values on the order of 10^5 in standard 220-nm-high single-mode silicon MRRs around 1550 nm.

Several approaches have been explored for enhancing the *Q* factor in silicon MRRs, including minimizing light scattering at roughened sidewalls via shallow-etched or multimode waveguide designs and alternative fabrication methods based on selective oxidation, e-beam lithography, reactive ion plasma etching, inductively coupled plasma (ICP) etching, or low-pressure chemical vapor deposition (LPCVD). High *Q*-factor silicon MRRs fabricated using a selective oxidation process have been shown with intrinsic *Q*-factors of 5.1×10^5 [17] and 7.6×10^5 [18], although challenges remain in control of the fabrication process [19]. A silicon microring resonator with a *Q*-factor of 1.7×10^6 was demonstrated using a large cross-section multi-mode waveguide with a severely limited free spectral range (FSR) of 17.1 pm [20]. With a similar approach, a silicon microring resonator with a high *Q* of 1.3×10^6 and larger FSR was proposed in [21] with a bend radius of 450 µm. A silicon MRR with internal *Q*-factor of 1.1×10^6 and FSR of 0.208 nm and utilizing a multi-mode ridge waveguide was fabricated using a standard CMOS compatible silicon-on-insulator (SOI) process [22]. A multimode ultrahigh quality factor racetrack resonator with 1.6 µm width was proposed using standard single-etching process with the quality factor of 2.3×10^6 provided by a multiproject wafer foundry [23]. An internal quality factor of $2.2 \times 10^{7,}$ corresponding to 2.7 dB⁄m propagation loss was achieved in a silicon microring resonator with a radius of 2.45 mm cladded with silicon oxide [24] by oxidizing the wafer surface in a steam oxidation process and using a reflowing photoresist strategy. An intrinsic *Q*-factor of 1.57×10^6, corresponding to a waveguide loss of 0.35 dB/cm, was realized in a silicon MRR with a radius of 150 µm and an FSR of 0.845 nm using e-beam lithography with a top cladding of a glass-like compound from hydrogen silsequioxane (HSQ) covered with a silicon oxide layer [25]. Low-loss submicron silicon-on-insulator strip waveguides were reported with 0.5 dB/cm loss at 1310 nm with 30 µm bend radius cladded with silicon oxide [26] using H_2 plasma post-lithography treatment and H_2 thermal annealing after silicon etching. More generally, propagation losses lower than 0.4 dB/cm for the *C*-band and 0.8 dB/cm for the *O*-band for the silicon wire waveguides have been reported for waveguides with a 440 nm core width and 220 nm core height and 2 μm-thick SiO_2 cladding layer defined by a high-resolution immersion lithography process [27]. While all of these approaches to improving *Q* factors in silicon MRRs are promising for different applications, they either suffer from performance trade-offs (e.g. multi-mode operation, larger footprint and/or significantly reduced FSR) or added fabrication cost and complexity.

In this paper we demonstrate a silicon MRR with a *Q*-factor of 1.5×10^6 at 1550 nm, corresponding to a propagation loss of 0.42 dB/cm, fabricated with a standard foundry process, plus a low-temperature post-process deposition of a TeO_2 cladding layer. In addition to enabling a straightforward and monolithic low-loss hybrid waveguide structure, TeO_2 has promising optical properties for new functionalities in silicon photonic microsystems. TeO_2 has been shown to be thermally and chemically stable, possess high nonlinearity, low optical attenuation from visible to mid-infrared wavelengths (0.4 ~ 5 µm), have a high refractive index (2.1 at 1550 nm) and low dispersion [28]. Furthermore, the unique site variability in the TeO_2 glass matrix enables high rare earth dopant solubility and leads to large emission bandwidths, motivating its application in integrated optical amplifiers and lasers [29-31], including the recent demonstration of a hybrid rare-earth laser directly on silicon with the internal quality factor of 5.6×10^5 [32]. This low-loss platform has significant potential for linear, nonlinear, and active optical applications in silicon photonics.

5.2 Microring Resonator Fabrication and Design

The microring resonator structure used in this work is displayed in figure 5.1. It consists of an integrated silicon microring and bus waveguide coated with a thin film of tellurium oxide (TeO_2). The silicon structure was fabricated in a silicon photonics foundry on a wafer-scale SOI platform with a 220-nm silicon layer thickness and consists of a 30-µm-radius silicon microring constructed using a 0.5 µm-wide waveguide. The bus waveguide is 0.4 µm wide, and the point coupling gap is 1.0 µm. The structure was cladded with SiO_2 and subsequently a window on top of the microring resonator was etched to the silicon layer for use in the post-processing TeO_2 deposition or unclad device experiments. A set of devices with identical dimensions but without the SiO_2 cladding etched was also fabricated for comparison. Deep etching was used for end-facet preparation and wafer dicing. For the TeO_2-clad devices, the structure was coated with a 270 nm thick TeO_2 film deposited using a room-temperature reactive RF co-sputtering post-processing step with 145 W of tellurium target sputtering power, 2.8 mTorr chamber pressure, and 12 and 7.6 sccm of argon and oxygen flow, respectively. The substrate temperature was set at 20°C. A top-view scanning electron microscope (SEM) image and the cross-section diagram of the TeO_2-coated Si microring resonator are displayed in figure 5.1a and 5.1b, respectively. Figure 5.1c and 5.1d show the image of the experimental setup and microscopic image of microring resonator with open window structure.

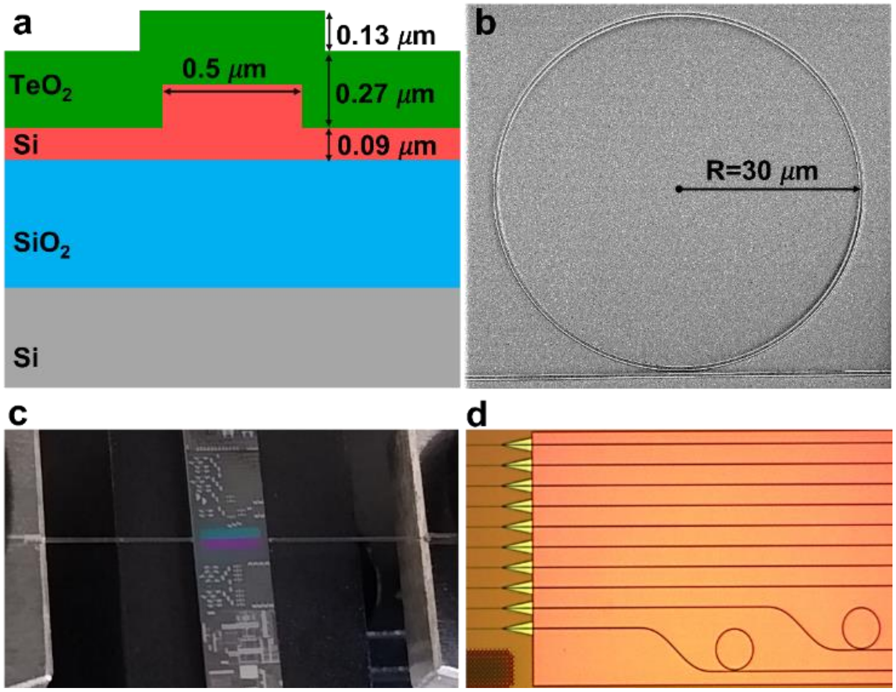

FIGURE 5.1: a) Cross-section profile of the TeO_2-coated Si microring showing the microring structure. b) Top-view SEM image of a TeO_2-coated Si microring resonator. c) Photograph of the coupling setup during measurement showing the SOI chip with window opening for TeO_2 post-processing deposition. d) Microscopic image of the open window microring resonator structure.

The electric field profiles of the transverse-electric- (TE-) polarized fundamental modes calculated using a finite element method (FEM) modesolver for the (cladding-core) TeO_2-Si, SiO_2-Si, and air-Si waveguide at 1550 nm wavelength are displayed in figure 5.2a, figure 5.2b, and figure 5.2c, respectively. We also summarize the calculated optical properties of the TeO_2-Si, SiO_2-Si, and air-Si microring resonator structure in figure 5.2d. The microring resonators and the bus waveguides were designed to achieve single-mode waveguide conditions at 1.55 µm to 2 µm wavelengths. The ring waveguide structure supports the TE-polarized and TM-polarized modes, and it has low bending radiation loss at 1550 nm for TE only. The effective index of the TeO_2-coated resonator is 2.8, which is almost 7.7 and 12% higher than the air and SiO_2 clad devices. For the TeO_2-coated Si microring resonator, 21.7 % of the optical power is confined in the TeO_2 coating layer, while 65 % is confined in the silicon layer. The rest of the optical power is confined in the lower SiO_2 cladding. Slightly lower cladding confinement of 15.8 and 17.2 %, respectively, is observed in the air and SiO_2 clad cases. The effective area is slightly larger in the TeO_2-coated Si microring resonator than SiO_2-coated and uncoated silicon microring resonators, although the mode is pulled upward more into the cladding, both of which can influence the ring-bus waveguide coupling.

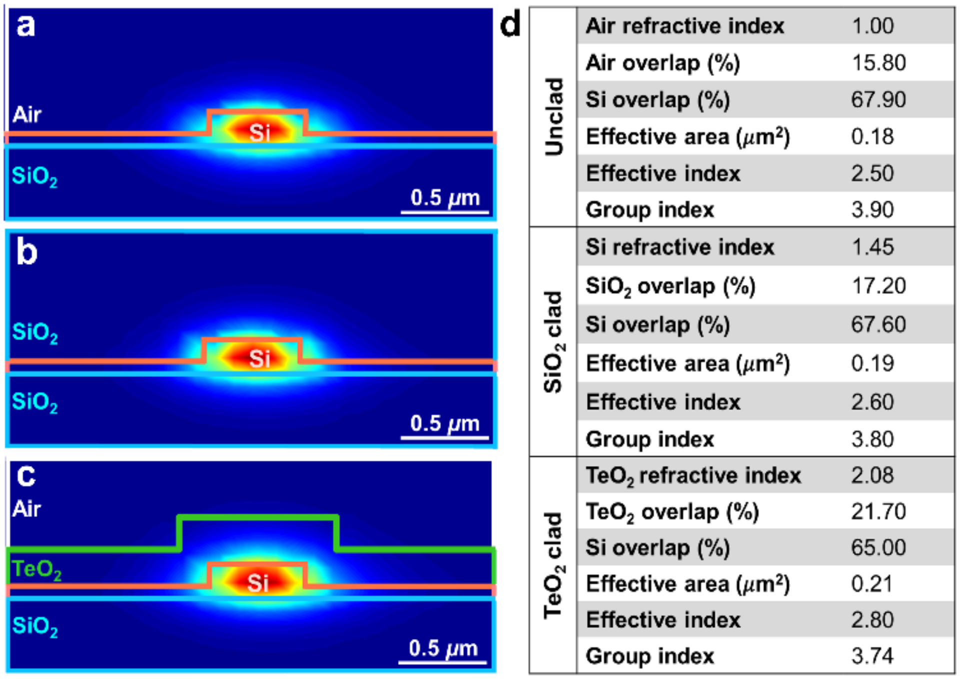

Unclad	Air refractive index	1.00
	Air overlap (%)	15.80
	Si overlap (%)	67.90
	Effective area (μm^2)	0.18
	Effective index	2.50
	Group index	3.90
SiO_2 clad	Si refractive index	1.45
	SiO_2 overlap (%)	17.20
	Si overlap (%)	67.60
	Effective area (μm^2)	0.19
	Effective index	2.60
	Group index	3.80
TeO_2 clad	TeO_2 refractive index	2.08
	TeO_2 overlap (%)	21.70
	Si overlap (%)	65.00
	Effective area (μm^2)	0.21
	Effective index	2.80
	Group index	3.74

FIGURE 5.2: Calculated electric field profile of the fundamental transverse-electric- (TE-) polarized mode for a) unclad, b) SiO_2-clad, and c) TeO_2-clad silicon microring resonators. d) Calculated fractional optical intensity overlap factors and effective mode areas for the fundamental TE microring mode at 1550 nm wavelength

The TeO_2-coated resonator has a higher mode area of approximately 0.20 μm^2 at 1.55 μm. The effective index increases for the TeO_2 film cladding as the resonant mode becomes more confined in the TeO_2 layer. The expansion of the optical mode at longer wavelengths decreases the effective index. The results show that approximately 60% of the mode power is confined in the Si region and 26% in the TeO_2 cladded layer for TeO_2-cladding at a wavelength of 1.55 μm.

5.3 Microring Resonator Characterization

We used a fiber-chip edge coupling setup, tunable Agilent 81640A 1510-1640 nm laser and a fiber probe station to characterize the passive transmission properties of the silicon microring resonators. TE polarized light from a 1550-nm tunable laser was launched into the chip through the polarization controller and lensed fiber, and the transmitted light across the chip was launched to the output lensed fiber connected to the Agilent power sensor. We observe TE single mode resonances supported by the microring resonator as shown in figures 5.3a, 5.3b, and 5.3c. For the TeO_2-coated silicon microring resonator, we measured a free spectral range (FSR) of 3.7 nm at a wavelength of 1573 nm. The air and SiO_2-clad devices are undercoupled over the measured transmission range, while the TeO_2-clad MRR is under-coupled at shorter wavelengths and becomes critically coupled above ~1600 nm. By fitting the transmission responses of the under-coupled resonator using a Lorentzian function as indicated in figures 5.3d, 5.3e, and 5.3f we obtain internal quality factors, Q_i, of 2.0×10^5 at 1542.43 nm, 6.7×10^5 at 1587.28 nm, and 1.5×10^6 at 1579.94 nm for the uncoated, SiO_2-coated, and TeO_2-coated silicon MRR, respectively, corresponding to 3.4

dB/cm, 0.97 dB/cm, 0.42 dB/cm propagation loss in the microring [33]. The results are summarized in Table 1, including the TeO_2 film loss measured by prism coupling on a witness sample, showing low material loss, and fitted external and internal *Q* factors for the MRRs with different top claddings.

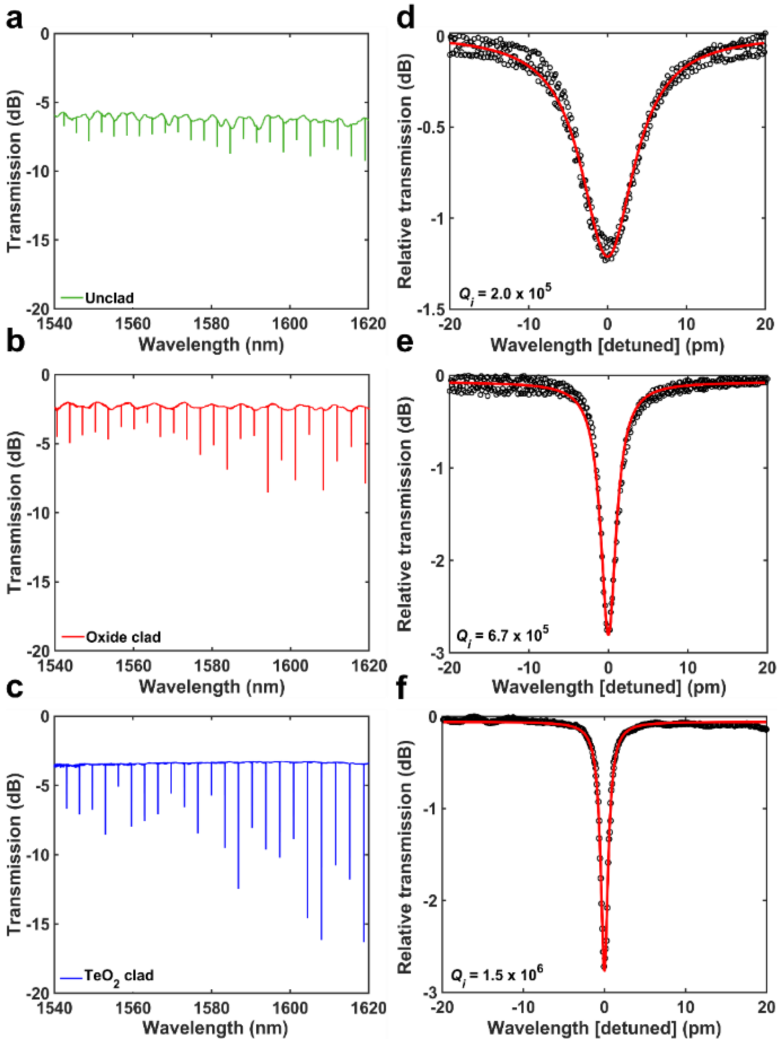

FIGURE 5.3: Measured TE transmission spectra for a) uncoated b) SiO_2-coated c) TeO_2-coated silicon microring resonators with a microring-waveguide gap of 1.0 µm. Close-up views of the under-coupled resonances for the d) uncoated, e) SiO_2-coated, and f) TeO_2-coated silicon microring resonators showing an intrinsic quality factor, Q_i, of 1.5 x 10^6 corresponding to 0.42 dB/cm optical propagation loss for the TeO_2-coated silicon microring resonator.

The total loss in the MRR can be expressed as the losses from the bulk materials, which includes contributions from the Si, SiO_2 and TeO_2 linear absorption and Si nonlinear (two-photon) absorption, radiation loss due to waveguide bends and surface scattering losses related to the waveguide surface roughness and geometry. The bulk loss includes losses from impurities, internal defects, absorption loss due to chemical bonds, and nano- and micro-voids. Because of the high-quality silicon-on-insulator and SiO_2 foundry materials, and low TeO_2 film loss, we expect the bulk material loss contribution to be negligible. Furthermore, nonlinear optical loss is anticipated to be low due to the low power used in transmission experiments.

TABLE 5.1: Measured properties of silicon microring resonators with different cladding materials

Cladding material	Cladding thickness (nm)	Film loss @ 638 nm (dB/cm)	Film loss @ 1550 nm (dB/cm)	Extinction ratio (dB)	External *Q* factor	Internal *Q* factor	Propagation loss (dB/cm)
Uncladded	----	----	----	1.2	2.8×10^6	2.0×10^5	3.4
SiO_2	2000	----	----	2.8	4.2×10^6	6.7×10^5	0.97
TeO_2	270	0.5±0.2	0.1±0.1	2.8	9.0×10^6	1.5×10^6	0.42

We calculated the theoretical radiation loss and equivalent *Q* factor for the TeO_2-coated silicon microring resonator structure using an FEM bent eigenmode solver, for varying bend radius as shown in figure 5.4a. The dashed lines in figure 5.4a indicate the experimentally determined internal *Q* factors for the MRRs with different claddings. The calculated radiation limited *Q* factors were measured 3×10^8, 1×10^8, and 1.7×10^7 for

TeO_2 clad, SiO_2 clad, and unclad microring resonators, respectively, at a radius of 30 µm corresponding to 0.002 dB/cm, 0.007 dB/cm, and 0.04 dB/cm of propagation losses. The results show that the radiation loss is negligible ($Q > 10^7$) at the selected bend radius of 30 µm.

The surface scattering loss is the waveguide scattering loss per unit length and was calculated using the widely used Payne-Lacey model [34]. This model has been applied previously to 3D-SOI bent waveguides [35-37] such that:

$$\alpha_{Surface\ Scattering} = 4.34 \frac{\sigma^2}{\sqrt{2} k_0 (\frac{W}{2})^4 n_1} f.g.\eta \tag{5.1}$$

where σ, k_0, W, and n_1, are the roughness, free-space wave vector, waveguide width, and core index, respectively. The function f is determined by the correlation length (L_c), while g is determined by the geometry of the waveguide and accounts for ridge-type waveguide structures such as the SOI ridge rings investigated here. Both σ and L_c are typically measured via atomic force microscopy or scanning-electron microscopy of a waveguide. We assumed values of 1.0 nm and 50 nm for σ and L_c, respectively, based on previous measurements on SOI waveguides [35-38]. We also assume the roughness of the TeO_2 coating can be neglected based on previous AFM roughness measurements showing < 1 nm root mean square (RMS) surface roughness on low-loss sputtered thin films [38]. Details of the expressions g and f can be found in the Payne-Lacey model [34]. The Payne-Lacey model was modified for bent waveguides and rings by adding a correction factor η [35] which allows us to accurately predict the loss of bent waveguides or resonators given the value of sidewall roughness. The correction factor η is defined as the ratio of the mode overlap between bent and straight waveguides using an FEM simulation. In the Payne-Lacey bending model, η is considered 1 in the straight waveguide. We plot the sidewall scattering loss as a function of wavelength in figure 5.4b. The experimental loss obtained from the quality factor measurements of the MRRs follows the same trend as the Payne-Lacey model, which indicates that the losses in the different MRRs are largely influenced by the core cladding refractive index contrast and sidewall roughness [23]. These results show that the application of a high refractive index TeO_2 top cladding can be considered promising for low-loss passive components as well as active devices such as monolithic amplifiers and lasers with improved performance on the SOI platform [32].

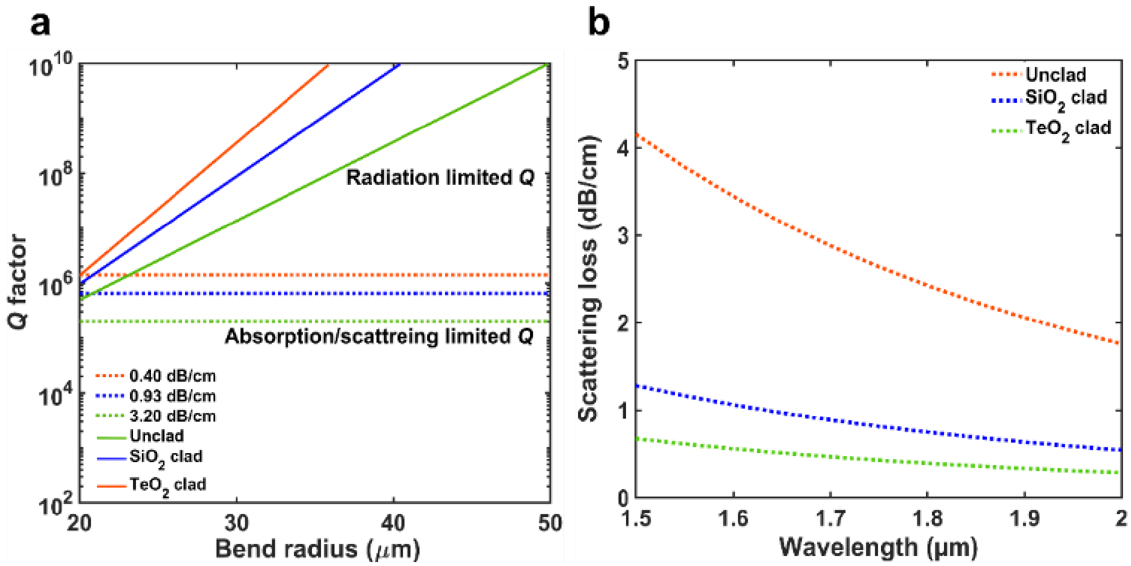

FIGURE 5.4: a) Calculated internal Q factor of uncoated-, SiO_2-coated, TeO_2-coated silicon resonator waveguides versus bend radius. b) Calculated scattering loss as a function of wavelength for microring resonators with air, SiO_2 and TeO_2 claddings based on the 3D Payne-Lacey model.

5.4 Conclusion

In summary, we have demonstrated a compact, single-mode TeO_2-Si hybrid microring resonator with 1.5×10^6 internal Q factor corresponding to 0.42 dB/cm propagation loss. The resonator is fabricated using a standard wafer-scale foundry process and a simple post-processing TeO_2 deposition step at room temperature. We propose that these results on tellurium oxide coated silicon microring resonators are promising for fabrication of integrated on-chip low cost and high-performance rare earth doped active devices such as amplifiers and lasers as well as low-loss passive and nonlinear devices in silicon photonic platforms, with signal processing, light generation, microwave photonics, environmental and biological sensing, and communications applications.

Bibliography

[1] D. Thomson, A. Zilkie, J. E. Bowers, T. Komljenovic, G. T. Reed, L. Vivien, D. Marris-Morini, E. Cassan, L. Virot, J.-M. Fédéli, J.-M. Hartmann, J. H. Schmid, D.-X. Xu, F. Boeuf, P. O'Brien, G. Z. Mashanovich, and M. Nedeljkovic, "Roadmap on silicon photonics," *J. Opt.* **18**, 073003 (2016).

[2] R. Baets, A. Z. Subramanian, S. P. Clemmen, B. Kuyken, P. Bienstman, N. Le Thomas, G. N. Roelkens, D. Van Thourhout, P. Helin, and S. Severi, "Silicon photonics: silicon nitride versus silicon-on-insulator," *Optical Fiber Communications Conference and Exhibition* (IEEE)1–3 (2016).

[3] M. R. Watts, M.J. Shaw, and G. N. Nielson, “Optical resonators: microphotonic thermal imaging,” *Nat. Photonics* **1,** 632 (2007).

[4] M. A. Tran, D. Huang, T. Komljenovic, J. Peters, A. Malik and J. E. Bowers, “Ultra-low-loss silicon waveguides for heterogeneously integrated silicon/III-V photonics,” *Appl. Sci.* **8**, 1139 (2018).

[5] C. Xiang, W. Jin, J. Guo, C. Williams, A. M. Netherton, L. Chang, P. A. Morton, and J. E. Bowers, “Effects of nonlinear loss in high-Q Si ring resonators for narrow-linewidth III-V/Si heterogeneously integrated tunable lasers,” *Opt. Express* **28**, 19926–19936 (2020).

[6] A. Biberman and K. Bergman, “Optical interconnection networks for high performance computing system,” *Rep. Prog. Phys.* **75**, 046402 (2012).

[7] S. Xiao, M. H. Khan, H. Shen, and M. Qi, “Multiple-channel silicon micro-resonator-based filters for WDM applications,” *Opt. Express* **15**, 7489–7498 (2007).

[8] E. Salih Magden, N. Li, Purnawirman, J. D. B. Bradley, N. Singh, A. Ruocco, G. S. Petrich, G. Leake, D. D. Coolbaugh, E. P. Ippen, M. R. Watts, and L. A. Kolodziejski, “Monolithically-integrated distributed feedback laser compatible with CMOS processing,” *Opt. Express* **25**, 18058–18065 (2017).

[9] B. Stern, X. Ji, A. Dutt, and M. Lipson, “Compact narrow-linewidth integrated laser based on a low-loss silicon nitride ring resonator,” *Opt. Lett.* **42**, 4541–4544 (2017).

[10] Y. Sun, and X. Fan, “Optical ring resonators for biochemical and chemical sensing. Analytical and Bioanalytical Chemistry,” *Anal Bioanal Chem* **399**, 205–211 (2011).

[11] M. Ji, H. Cai, L. Deng, Y. Huang, Q. Huang, J. Xia, Z. Li, J. Yu, and Y. Wang, “Enhanced parametric frequency conversion in a compact silicon-graphene microring resonator,” *Opt. Express* **23**, 18679–18685 (2015).

[12] K. Miarabbas Kiani, H. M. Mbonde, H. C. Frankis, R. Mateman, A. Leinse, A. P. Knights, and J. D. B. Bradley, “Four-wave mixing in high-Q tellurium-oxide-coated silicon nitride microring resonators,” *OSA Continuum* **3**, 3497–3507 (2020).

[13] D. Grassani, S. Azzini, M. Liscidini, M. Galli, M. J. Strain, M. Sorel, J. E. Sipe, and D. Bajoni, “Micrometer-scale integrated silicon source of time-energy entangled photons,” *Optica* **2**, 88–94 (2015).

[14] M. La Notte, B. Troia, T. Muciaccia, C. E. Campanella, F. De Leonardis, and V. M. Passaro, “Recent advances in gas and chemical detection by Vernier effect-based photonic sensors,” *Sensors* **14**, 4831–4855 (2014).

[15] D. G. Rabus, M. Hamacher, U. Troppenz, and H. Heidrich, “Optical filters based on ring resonators with integrated semiconductor optical amplifiers in GaInAsP-InP,” *IEEE. J. Sel. Top. Quantum Electron.* **8**, 1405–1411 (2002).

[16] O. Dubray, M. A. Seyedi, C. H. Chen, B. Charbonnier, A. Descos, M. Fiorentino, R. G. Beausoleil, and S. Menezo, “30Gbit/s PAM-4 transmission by modulating a dual silicon ring resonator modulator,” *Optical Interconnects Conference* (IEEE) 6–7 (2016).

[17] L. Luo, G. S. Wiederhecker, J. Cardenas, C. Poitras, and M. Lipson, “High quality factor etchless silicon photonic ring resonators,” *Opt. Express* **19**, 6284–6289 (2011).

[18] A. Griffith, J. Cardenas, C. B. Poitras, and M. Lipson, “High quality factor and high confinement silicon resonators using etchless process,” *Opt. Express* **20**, 21341–21345 (2012).

[19] P. Dong, W. Qian, S. Liao, H. Liang, C. Kung, N. Feng, R. Shafiiha, J. Fong, D. Feng, A. V. Krishnamoorthy, and M. Asghari “Low loss shallow-ridge silicon waveguides,” *Opt. Express* **18**, 14474–14479 (2010).

[20] M. A. Guill, M. Caverley, E. Cretu, N. A. F. Jaeger, and L. Chrostowski, “Large-area, high- Q SOI ring resonators,” *IEEE Photonics Conf. IPC* **4**, 336–337 (2014).

[21] M. Burla, B. Crockett, L. Chrostowski, and J. Azaña, “Ultra-high Q multimode waveguide ring resonators for microwave photonics signal processing,” *International Topical Meeting on Microwave Photonics (MWP)* 1–4 (2015).

[22] Y. Zhang, X. Hu, D. Chen, L. Wang, M. Li, P. Feng, X. Xiao, and S. Yu, “Design and demonstration of ultra-high-Q silicon microring resonator based on a multi-mode ridge waveguide,” *Opt. Lett.* **43**, 1586–1589 (2018).

[23] L. Zhang, L. Jie, M. Zhang, Y. Wang, Y. Xie, Y. Shi, and D. Dai, “Ultrahigh-Q silicon racetrack resonators,” *Photon. Res.* **8**, 684–689 (2020).

[24] A. Biberman, M. J. Shaw, E. Timurdogan, J. B. Wright, and M. R. Watts, “Ultralow-loss silicon ring resonators,” *Opt. Lett.* **37**, 4236–4238 (2012)

[25] M. P. Nezhad, O. Bondarenko, M. Khajavikhan, A. Simic, and Y. Fainman, “Etch-free low loss silicon waveguides using hydrogen silsesquioxane oxidation masks,” *Opt. Express* **19**, 18827–18832 (2011).

[26] C. Bellegarde, E. Pargon, C. Sciancalepore, C. Petit-Etienne, V. Hugues, D. Robin-Brosse, J. Hartmann, and P. Lyan, "Improvement of sidewall roughness of submicron SOI waveguides by hydrogen plasma and annealing," *IEEE Photonics Technol. Lett.* **30**, 591–594 (2018).

[27] T. Horikawa, D. Shimura, and T. Mogami, "Low-loss silicon wire waveguides for optical integrated circuits," *MRS Communications* **6**, 9–15 (2016).

[28] H. C. Frankis, K. Miarabbas Kiani, D. B. Bonneville, C. Zhang, S. Norris, R. Mateman, A. Leinse, N. D. Bassim, A. P. Knights, and J. D. B. Bradley, "Low-loss TeO_2-coated Si_3N_4 waveguides for application in photonic integrated circuits," *Opt. Express* **27**, 12529–12540 (2019).

[29] K. Miarabbas Kiani, H. C. Frankis, H. M. Mbonde, R. Mateman, A. Leinse, A. P. Knights, and J. D. B. Bradley, "Thulium-doped tellurium oxide waveguide amplifier with 7.6 dB net gain on a silicon nitride chip," *Opt. Lett.* **44**, 5788–5791 (2019).

[30] K. Miarabbas Kiani, H. C. Frankis, R. Mateman, A. Leinse, A. P. Knights, and J. D. B. Bradley, "Thulium-doped tellurium oxide microring lasers integrated on a low-loss silicon nitride platform," *Opt. Mater. Express* **11**, 3656-3665 (2021).

[31] A. Jha, B. Richards, G. Jose, T. Teddy-Fernandez, P. Joshi, X. Jiang, and J. Lousteau, "Rare-earth ion doped TeO_2 and GeO_2 glasses as laser materials," *Prog. Mater. Sci.* **57**, 1426–1491 (2012).

[32] K. Miarabbas Kiani, H. C. Frankis, C. M. Naraine, D. B. Bonneville, A. P. Knights, and J. D. B. Bradley, "Lasing in a hybrid rare-earth silicon microdisk," *Laser Photon. Rev.* **16**, 210034 (2022).

[33] K. Preston, B. Schmidt, and M. Lipson, “Polysilicon photonic resonators for large-scale 3D integration of optical networks” *Opt. Express* **15**, 17283–17290 (2013).

[34] F. P. Payne, and J. P. R. Lacey, “A theoretical analysis of scattering loss from planar optical waveguides,” *Opt. Quantum Electron.* **26**, 977–986 (1994).

[35] D. E. Hagan, and A. P. Knights, “Mechanisms for optical loss in SOI waveguides for mid-infrared wavelengths around 2 μm” *J. Opt.* **19**, 025801 (2017).

[36] K. P. Yap, A. Delâge, J. Lapointe, B. Lamontagne, J. H. Schmid, P. Waldron, B. A. Syrett, and S. Janz, “Correlation of scattering loss, sidewall roughness and waveguide width in SiO_2/Si silicon-on-insulator (SOI) ridge waveguides,” *J. Lightwave Technol.* **27**, 3999-4008 (2009).

[37] H. Shang, D. Sun, P. Yu, B. Wang, T. Yu, T. Li, and H. Jiang, “Investigation for Sidewall Roughness Caused Optical Scattering Loss of Silicon-on-insulator waveguides with confocal laser scanning microscopy,” *Coatings* **10** (3), 236 (2020).

[38] J. W. Miller, M. Chesaux, D. Deligiannis, P. Mascher, and J. D. B. Bradley, “Low-loss GeO_2 thin films deposited by ion-assisted alternating current reactive sputtering for waveguide applications,” *Thin Solid Films* **709**, 138165 (2020).

Chapter 6

Lasing in a Hybrid Rare-Earth Silicon Microdisk

Preface

The following chapter focuses on a novel rare-earth silicon hybrid-integrated microdisk laser. On-chip light sources are of significant interest for silicon photonic microsystems because silicon is a poor light emitter, and various approaches have been investigated which typically involve significant tradeoffs in performance, fabrication complexity and/or cost. Our hybrid laser is based on a thulium-doped tellurite-glass-coated silicon microresonator. The thulium gain medium is deposited via reactive radio frequency (RF) co-sputtering, which is a straightforward, low-cost and monolithic approach to achieve gain and lasing in silicon. The silicon microdisk laser was fabricated using the Advanced Micro Foundry (AMF) silicon photonics fabrication process in Singapore and a sputtering system in the

Centre for Emerging Device Technologies (CEDT) at McMaster University. Importantly, the developed methods, including low-temperature deposition of the gain medium, are compatible with standard passive and active silicon photonic devices, enabling the laser's implementation in high performance silicon photonic integrated circuits. The advantages of this hybrid silicon microdisk laser versus alternative approaches include its low cost, simplicity, high compactness, and compatibility with volume manufacturing using standard silicon photonic foundry processes.

Section 6.2 describes the microdisk laser design and structure, which includes a 20 µm radius and 220 nm thick silicon microdisk cladded with a 370 nm thick TeO_2:Tm^{3+} layer as the active medium. Pump light and laser emission are coupled to and from the disk, respectively, via an integrated silicon bus waveguide. The calculated optical properties of the hybrid TeO_2:Tm^{3+}-Si resonator structure using a finite element bent eigenmode solver are summarized. In section 6.3, The optical properties of the TeO_2:Tm^{3+}-coated silicon microdisk resonator is characterized. The resonator's passive transmission properties are measured, including its resonance spectrum and Q factor. The TeO_2:Tm^{3+}-Si hybrid microdisk resonator is pumped to explore its lasing potential and describe the laser results. Single-mode lasing is shown and output powers of approximately 1 mW around a wavelength of 1900 nm via efficient pumping at telecom wavelengths around 1600 nm, with a single-sided slope efficiency of 4.2% versus launched pump power into the silicon bus waveguide. Section 6.4 discusses the advantageous properties and performance of the microdisk laser in the context of previous rare-earth lasers on silicon and suggests future directions of research for improved designs and prospective applications.

In section 6.5, lower $TeO_2:Tm^{3+}$ film propagation loss, optimized thulium concentration, and optimized pump wavelength, enabled us to achieve on-chip, low-threshold, thulium-doped silicon microdisk lasers with 20 μm and 30 μm radii next to a pulley-coupled silicon bus waveguide. These lasers results showing higher power on chips with different $TeO_2:Tm^{3+}$ film properties provide a guide for future work on optimization of integrated thulium doped silicon lasers. The results are summarized, and conclusions are given in section 6.6. Additional specific details are provided in section 5.6. Section 6.7.1 describes the laser fabrication process including the post-processing $TeO_2:Tm^{3+}$ thin film deposition as the top cladding material. The background loss and theoretical gain are calculated in section 6.7.2 using a finite-element modesolver (RSoft FemSIM) method. Section 6.7.3 and 6.7.4 describe the active and passive properties of the silicon microdisk laser and the experimental gain measurement method, including the demonstration of net optical gain in the hybrid $TeO_2:Tm^{3+}$-Si bus waveguide.

Lasing in a hybrid rare-earth silicon microdisk

Khadijeh Miarabbas Kiani, Henry C. Frankis, Cameron M. Naraine, Dawson B. Bonneville, Andrew P. Knights, and Jonathan D. B. Bradley

McMaster University, 1280 Main Street West, Hamilton, ON, Canada

This paper was published in Photonics & Lasers Review on November 12, 2021.

DOI: 10.1002/lpor.202100348

Section 6.5 on the low-threshold high power silicon microdisk lasers were added in the following thesis chapter and will form the basis of a future submission for publication as a journal article. Minor modifications have also been made to the abstract, introduction, and conclusions based on these additional results.

Abstract

Silicon photonics is an ideal platform for low-cost, energy-efficient, and high-performance optical microsystems. However, because silicon is an inefficient light-emitting material, the development of simple, inexpensive, and scalable monolithic amplifiers and light sources has been a significant challenge. Here, we report on optical gain and lasing in an ultra-compact hybrid rare-earth silicon microdisk resonator. The microdisk design is straightforward and compatible with the fabrication steps and device dimensions available in all silicon photonics foundries, while the thulium-doped tellurite gain medium is added in a low-temperature single-step sputter deposition. This approach allows for low-cost and high-volume wafer-scale manufacturing and co-integration of rare-earth amplifiers and light sources with silicon passive and active devices with no adjustment to standard process flows. The hybrid laser is pumped at standard telecom wavelengths around 1.6 µm and exhibits stable single-mode emission at 1.9 µm, with an internal slope efficiency of 60% and > 1 mW on-chip output power. Recently, I demonstrated low-threshold lasing around 1.9 µm in compact thulium-silicon hybrid microdisk resonators with a pulley-coupled design. We observe total double-sided on-chip output powers of > 2 mW and threshold pump powers of < 1 mW launched into the bus waveguides. The laser is highly promising for emerging communications and sensing applications and opens new possibilities for the development of monolithic rare-earth optical amplifiers and lasers directly on silicon.

6.1 Introduction

Silicon photonics technology enables compact, low-power, and cost-effective optical microsystems on a chip by leveraging the materials and advanced fabrication methods developed over decades for integrated silicon electronics [1,2]. Silicon photonics foundries now provide standard services and process design kits containing many of the building blocks required for high-performance optical circuits, including passive components such as optical waveguides, filters and (de-)multiplexors and active optoelectronic components such as high-speed modulators, switches, and photodetectors [3–5]. However, on-chip optical amplifiers and light sources are still a significant challenge for foundry offerings in terms of the required provision for high-yield, widely deployed, integrated building blocks [6–8]. Silicon is an inefficient light-emitting material because it is an indirect bandgap semiconductor. Thus, electron-hole recombination must be mediated by phonon emission or absorption to conserve momentum, which makes radiative carrier recombination much less likely than non-radiative recombination. Further, light emission via carrier recombination is also limited to wavelengths < 1.1 μm due to silicon's 1.1 eV bandgap, which is below wavelengths compatible with low-loss silicon photonic microsystems. Compact amplifiers and light sources are in increasing demand for silicon photonics applications including communications, sensing, detection and ranging, metrology, quantum information and artificial intelligence over an ever-broadening wavelength range extending from the near- to mid-infrared.

Various methods have been developed to build optical amplifiers and light sources onto silicon chips, including stimulated Raman emission in silicon [9], heterogeneously bonded or directly grown III-V semiconductors [10], germanium [11] and germanium-tin alloys [12], silicon-nitride based parametric oscillators [13], silicon-organic hybrid devices [14], and rare-earth gain media [15]. Many promising results have been reported, particularly in the direction of electrically-pumped III-V heterogeneously- and hybrid-integrated devices based on substantial research and development, leading to commercial devices and systems [16,17]. Nevertheless, because of the costly and complex methods, materials, and fabrication infrastructure required, such processes are not universally adopted in all silicon photonics foundries and multi-project wafer services. Silicon Raman and germanium-based devices are favourable for their monolithic integration, yet currently face limitations due to silicon's narrowband Raman gain and strong two-photon absorption-induced free carrier absorption and germanium's indirect bandgap, respectively. As an alternative option for many applications, low-cost optically-pumped solutions can be explored using monolithic broadband dielectric gain materials [14,15], motivated by extensive developments in packaging and assembly of photonic integrated circuits (PICs) and the availability of compact commercial III-V gain dies and lasers for external pump sources [18]. General challenges such as heating due to high currents and large metal pad count in on bonded on-chip electrically-pumped amplifiers and lasers [19], by comparison make such a scheme potentially transformative by enabling straightforward broadband all-optical gain and light emission in the silicon circuit with a standardized fixed-wavelength pump source and single intra-chip interconnection. Straightforward approaches for building monolithic gain materials directly on silicon chips, which are compatible with silicon photonic foundry processes, are highly attractive for their low cost and versatility in device and system design.

Building on their success in fiber-optic and bulk glass and crystal platforms, rare-earth-doped optical gain materials have recently shown significant promise for silicon-based amplifiers and light sources [20–26]. Rare-earth gain materials can be deposited monolithically on silicon allowing for low-cost wafer-scale fabrication and versatile device designs, have high thermal stability, exhibit narrow intrinsic linewidths, and provide broadband optical gain and lasing in important near- and mid-infrared bands. However, the development of on-chip rare-earth amplifiers and lasers integrated directly with silicon has proven challenging because of a combination of high optical loss in silicon waveguides, relatively low rare-earth gain and low optical overlap with the gain medium, making it difficult to achieve net optical gain in waveguides and lasing in silicon-based cavities. Signal enhancement was investigated in [27] and lasing from a microdisk into a fiber was shown in [28], but optical gain or lasing in a silicon-on-insulator (SOI) waveguide on the chip were not demonstrated, and both studies used high-temperature fabrication steps which are incompatible with integration on silicon photonic active chips. Recently, rare-earth waveguide lasers have been demonstrated on a silicon photonics platform using a hybrid design based on multi-layer integration of silicon nitride cavities and erbium-doped aluminum oxide coatings with SOI waveguides [15,29]. However, despite their promising performance and utility in multi-layer silicon photonic circuits, in such devices the gain was not implemented directly in the silicon layer, the cavity sizes were relatively large, and high-power optical pumping was required. Such rare-earth laser designs are based on multiple low-loss silicon nitride waveguide layers in addition to the silicon waveguide layer, which increases the design complexity, is a non-standard feature in many silicon photonics foundries and separates the gain medium from the efficient passive and active functionality possible within the silicon waveguide layer, including thermal tuning and doping for modulation and detection. Further, the device footprints are orders of magnitude larger than other silicon photonic devices, with weakly-confined waveguides that require large bend radii and cavity lengths of several millimeters, limiting integration density in silicon photonic microsystems. The requirement for an off-chip optical pump would also limit their scalability and utility, unless smaller and more efficient designs can enable one fixed wavelength optical pump source to power many lasers on the chip. Gain in a more compact and straightforward design directly in silicon can enable a low-cost, scalable approach to rare-earth amplifiers and lasers on silicon.

Here, we demonstrate optical gain and lasing in a hybrid-integrated rare-earth silicon microdisk. The laser structure is straightforward, robust, low-cost and can be implemented using existing wafer-scale silicon photonics fabrication processes and a single room-temperature post-processing step. In contrast to previous rare-earth lasers, the laser cavity and output are directly in the silicon layer, and the ultra-compact device size of 40-µm-diameter is on a scale compatible with standard passive and active silicon photonic devices. We show single-mode lasing around 1.9 µm using a monolithic thulium-doped tellurite gain medium and efficient pumping at wavelengths around 1.6 µm, where silicon is highly transparent and commercial pump light sources are readily available. I subsequently show low-threshold hybrid-integrated thulium-doped tellurium oxide silicon microdisk lasers based on a pulley-coupled design showing lasing in 40 and 60 μm diameter microdisks with > 2 mW double-sided output power and slope efficiencies of up to 13.4% with respect to 1620 nm pump power launched to the bus waveguides. Both single-mode and multimode laser emissions were observed spanning across wavelengths from 1825 to 1939 nm with optimized thulium concentration of 4.3×10^{20} cm^{-3} for and the thresholds of < 1 mW versus launched pump power. Ultimately, these low threshold lasers with emission over a > 100 nm range have prospective applications in data communications, quantum information systems, artificial intelligence, nonlinear optical systems and open the door to highly compact monolithic PICs with optical gain on silicon photonics platforms in the emerging ~1.8–2.0 μm wavelength band. Besides demonstrating an effective and low-cost approach to rare-earth gain for silicon photonic microsystems, such lasers provide an incentive for expanding applications in an emerging 2-μm wavelength band, which is of interest for communications, nonlinear and quantum optics, and sensing [30–33] and is motivated by silicon's lower two-photon absorption and the recent development of efficient monolithic passive and active silicon devices in this range [34–37]. Optical gain and lasing in a hybrid rare-earth silicon structure opens the door to on-chip amplifiers for low-loss circuits and versatile integrated laser designs, using the wideband rare-earth gain available in different near- and mid-infrared wavelength regions of interest [38] and the high-performance passive and active functionality in the silicon layer, on silicon photonics platforms.

6.2 Fabrication and Design

In figure 6.1, we display the microdisk laser structure. The hybrid laser consists of an integrated silicon microdisk and bus waveguide which are coated in a thulium-doped tellurium oxide ($TeO_2:Tm^{3+}$) layer. The silicon structure was fabricated in a silicon photonics foundry on a wafer-scale SOI platform with a 220-nm silicon layer thickness and consists of a 40-µm-diameter silicon microdisk next to a point-coupled silicon bus waveguide. After silicon waveguide etching, and deep etching for end-facet preparation and wafer dicing, the uncoated SOI chips were transferred from the foundry for post-processing. We then coated the entire structure in a 0.37-µm-thick thulium-doped tellurium oxide ($TeO_2:Tm^{3+}$) film using a room-temperature reactive co-sputtering post-processing step. Further details on the fabrication can be found in the Methods section. Tellurium oxide was selected as a host material for thulium because of its low loss, high rare-earth solubility, high refractive index (n ~2.1) for compact devices and enhanced mode overlap, good thermal and chemical stability, and low temperature deposition, allowing for straightforward post-processing on chips containing silicon photonics active layers including metallic interconnects [39]. Of various rare-earth elements, we selected thulium because it offers key advantages as a laser ion for silicon. Trivalent thulium ions are a quasi-three level laser system with thermally-populated broadened Stark-split ground and excited states, which can be pumped at telecom wavelengths around 1.6 µm and show broad emission from ~1.7–2.1 µm on the $^3F_4$ excited state to $^3H_6$ ground state energy transition. Tm^{3+} ions exhibit relatively shifted absorption and emission spectra (resulting in low ground state absorption at longer laser wavelengths), minimal quenching effects at high ion concentrations and emission near the edge of silicon's low two-photon absorption window, allowing for straightforward population inversion in the laser cavity and efficient optical pumping and lasing. However, while high efficiency on-chip thulium lasers have been demonstrated in crystalline waveguides [40] and dielectric host materials on silicon substrates [41–43], thulium is relatively unexplored as a laser ion in an SOI platform. Importantly, here a standard silicon photonics foundry process was used to fabricate the disk platform and bus waveguide, which enables such hybrid lasers to be co-integrated with other passive and active silicon photonic devices on the same chip. Figure 6.1a shows a 3D drawing of the hybrid laser and energy level diagram for Tm^{3+} with the energy bands and transitions most relevant for the laser operation. A cross section diagram and a focused-ion-beam (FIB)-milled cross section of the silicon laser structure are displayed in figure 6.1b and 6.1c, respectively. Figure 6.1d shows a top view scanning electron microscope (SEM) image of the hybrid laser.

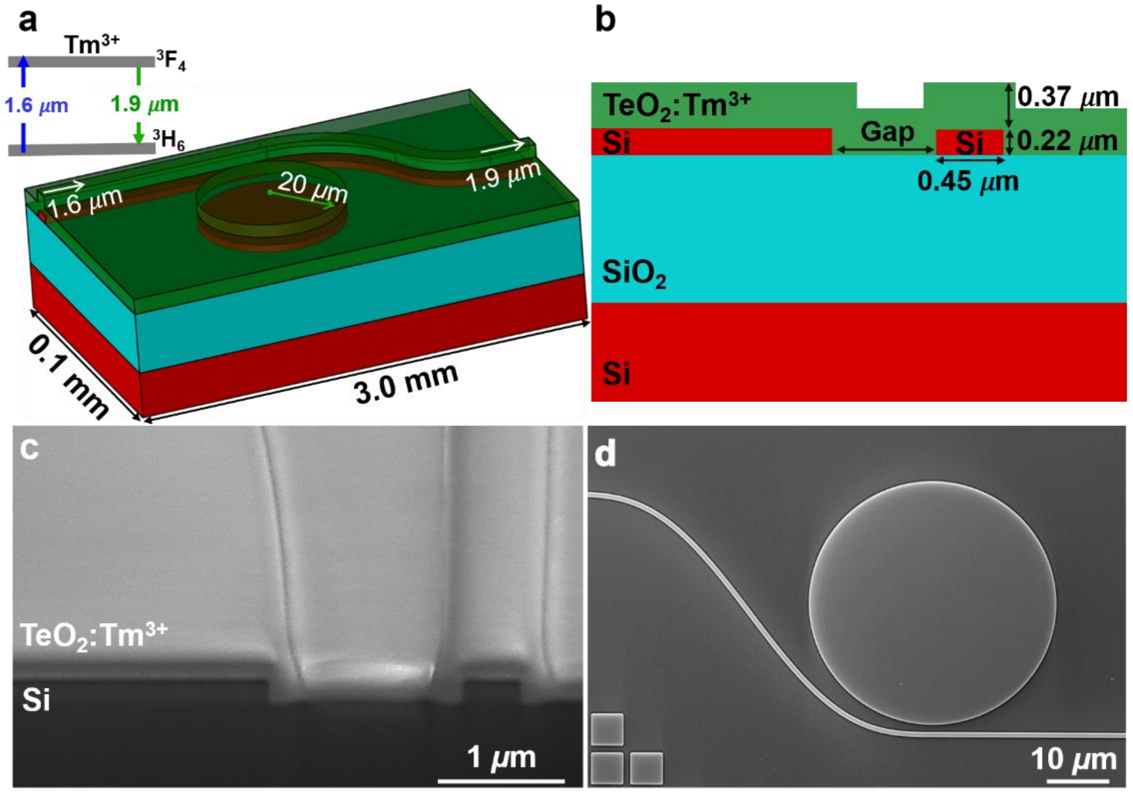

FIGURE 6.1: Silicon hybrid microdisk laser images: a) 3D drawing of the $TeO_2:Tm^{3+}$-coated silicon microdisk laser. Inset in a: Two-level Tm^{3+} energy diagram showing 1.6 µm photon absorption and excitation into upper level and de-excitation into the lower level and 1.9 µm photon emission. b) Cross-section profile of the $TeO_2:Tm^{3+}$-coated Si microdisk laser showing the microdisk structure and the bus waveguide dimensions. c) Focused ion beam milled scanning electron microscope (SEM) cross-section image of the coupling region between the $TeO_2:Tm^{3+}$-coated Si microdisk and bus waveguide. d) Top-view SEM image of a $TeO_2:Tm^{3+}$-coated Si microdisk laser.

We summarize the calculated optical properties of the hybrid $TeO_2:Tm^{3+}$-Si resonator structure in figure 6.2. The electric field profiles of the transverse-electric- (TE-) polarized fundamental modes for the microdisk resonator and waveguide and 1610-nm pump wavelength are displayed in figure 6.2a and figure 6.2b, respectively. Similarly, the TE-polarized fundamental modes for the microdisk and waveguide at the laser wavelength of 1906 nm are shown in figure 6.2c and figure 6.2d, respectively. To achieve gain in the disk resonator structure, a sufficient percentage of optical intensity must overlap with the

TeO_2:Tm^{3+} gain material. The theoretical properties of the pump and laser modes in the microdisk structure are displayed in figure 6.2e. For the microdisk resonator, approximately 15% and 19% of the optical power is confined in the TeO_2:Tm^{3+} coating at the pump and laser wavelengths, respectively. Because of strong optical confinement in the silicon disk, low loss and a relatively high Tm^{3+} concentration is required for sufficient amplification in the resonator and to achieve roundtrip net gain and lasing. The propagation loss in the microdisk includes contributions from the Si, TeO_2 and SiO_2 linear absorption, Si nonlinear (two-photon) absorption, Tm^{3+} absorption, scattering loss at interfaces and bending radiation loss. Linear absorption is low for all materials used in the hybrid resonator. The two-photon absorption coefficient at 1.9 μm is about half that at 1.5 μm [44], thus nonlinear absorption and its influence on the roundtrip gain are expected to be minimal near the lasing threshold. Since Tm^{3+} absorption at the laser wavelength is also low because of the small Tm^{3+} absorption cross section around 1900 nm, in our design we expect to be limited by the bending radiation and scattering loss, the former of which can be designed to be low by selecting an appropriate bending radius and the latter of which is limited by fabrication steps such as etching and must be extracted from experiment. We calculated the theoretical radiation loss and equivalent Q factor for the TeO_2:Tm^{3+}-coated silicon microdisk structure using a finite element bent eigenmode solver, as shown in figure 6.2f. The calculated radiation limited Q factor at pump and laser wavelengths shows that radiation loss is negligible at the selected bend radius of 20 μm. These results show that such disks can be effectively designed with a 20-μm radius and below before introducing significant radiation losses, potentially allowing for the fabrication of more compact devices than reported here.

When the bending loss is negligible the internal Q factor of the microdisk becomes limited by absorption and scattering losses, which are independent of bend radius. The dashed lines in figure 6.2f indicate the internal Q factors corresponding to different absorption/scattering-limited microdisk propagation losses. To achieve roundtrip gain and lasing in the cavity, the gain must exceed the cavity losses, including radiation, absorption/scattering loss and resonator-waveguide coupling loss. The inset in figure 6.2f shows the calculated upper limit of the Tm gain for different Tm concentrations, including the Tm concentration selected in this study. These results show that net roundtrip gain is achievable, accounting for the fact that the resonators are point-coupled and in the under-coupled regime and the coupling coefficient is low. Additional details regarding these calculations can be found in the Methods section.

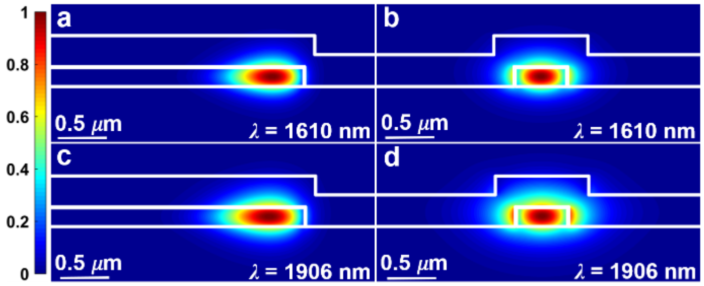

e

	Wavelength (nm)	Si Overlap (%)	TeO$_2$:Tm^{3+} Overlap (%)	Effective area (μm^2)
Microdisk	1610	76.3	14.7	0.35
	1906	69.4	19.0	0.47
Waveguide	1610	66.1	24.2	0.20
	1906	51.7	35.0	0.34

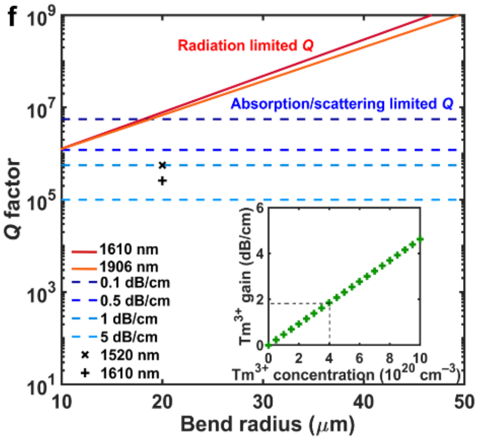

FIGURE 6.2: Calculated pump and laser modes and microdisk resonator loss and gain: Calculated electric field profile of the fundamental transverse-electric- (TE-) polarized mode for the laser wavelength using a finite-element method mode solver for a) the TeO$_2$:Tm^{3+}-coated silicon microdisk and b) the TeO$_2$:Tm^{3+}-coated silicon strip waveguide at the 1610 nm pump wavelength and c) microdisk and d) waveguide at the 1906 nm lasing wavelength. e) calculated fractional optical intensity overlaps and effective mode areas for the fundamental TE microdisk mode at the 1610 nm pump and 1906 nm lasing wavelengths. f) Calculated internal Q factor of the hybrid silicon microdisk laser at the pump and lasing wavelengths. The measured Q factors at 1521 and 1610 nm wavelength and 20 µm bend radius are also indicated with lines shown for several resonator losses, showing that the internal Q is limited by the absorption and scattering related propagation loss of the microdisk. The inset shows the calculated upper limit Tm^{3+} gain versus thulium concentration in the hybrid resonator.

6.3 Optical Characterization

We characterized the passive transmission properties of the microdisk resonator using a tunable laser and a fiber probe station (see Methods section for further details). As displayed in figure 6.3a, we observe narrow resonances associated with five different TE modes supported by the microdisk resonator. The extinction ratios are relatively low (≤ 1 dB), indicating the resonator is in the under-coupled regime. In this regime higher roundtrip gain can be achieved, increasing the probability of lasing, with the tradeoff that lower pump-power is coupled into the resonator resulting in reduced efficiency. By fitting the transmission responses of the under-coupled resonator using a Lorentzian function (inset of figure 6.3a), we obtain an internal quality factor, Q_i, of 5.6 × 10^5 at 1521 nm. This Q_i corresponds to a propagation loss of 1.0 dB/cm in the microdisk cavity. We expect even lower background propagation loss at the laser wavelength around 1900 nm [45]. We also obtain an internal quality factor of 2.7 × 10^5 corresponding to 1.9 dB/cm propagation loss at the pump wavelength of 1610 nm, confirming the higher Tm^{3+} ion absorption loss at this wavelength. These measurements are also shown on the plot in figure 6.2f and confirm that the Q factor is limited by Tm^{3+} absorption, background material loss and scattering loss inherent to the hybrid disk structure. In figure 6.3b, we measured the internal quality factors for various resonant modes and associated free spectral ranges (FSRs) (inset of figure 6.3b), in transmission experiments from 1520 nm to 1620 nm wavelength. The various microdisk modes show Q factors with similar magnitude and wavelength dependence, indicating similar background loss and mode overlap with the silicon and TeO_2:Tm^{3+} layers. The relatively large FSR of > 5 nm for our design increases the likelihood of single-mode as opposed to multi-mode lasing observed in previous integrated Tm microcavity lasers [35] and allows for engineering of the laser output wavelength by small adjustments in the resonator dimensions. The FSRs match well with those predicted via calculation and allow for us to confirm pumping on the fundamental TE microdisk mode.

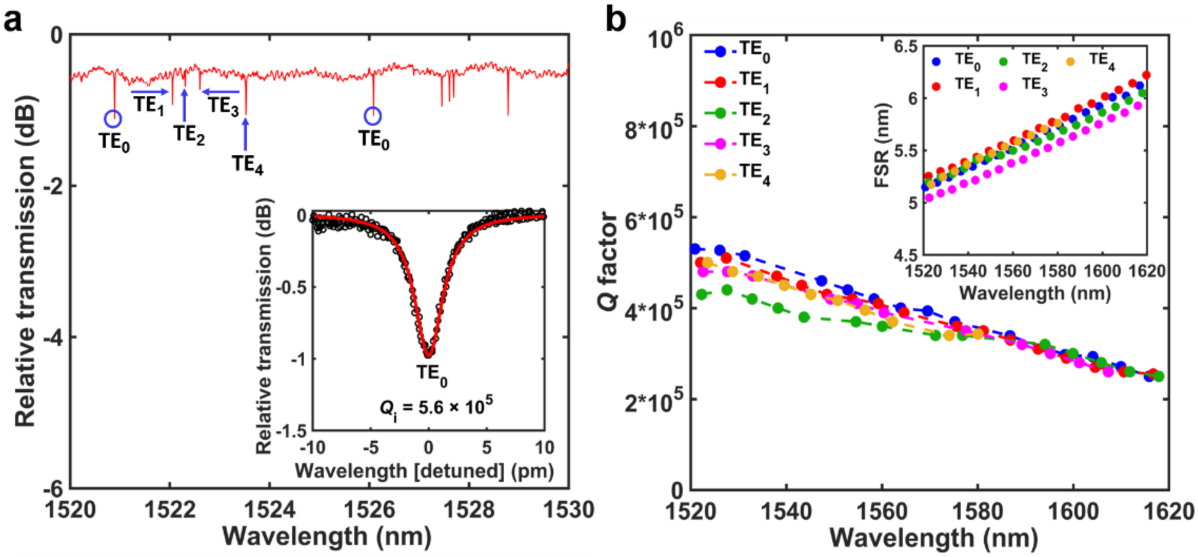

FIGURE 6.3: Transmission and loss measurements: a) Measured TE transmission spectrum for a $TeO_2:Tm^{3+}$-coated silicon microdisk with a microdisk-waveguide gap of 0.6 µm. Inset in a: a close-up view of the under coupled resonance at 1521 nm wavelength with extinction ratio of 0.95 dB and a fitted Lorentzian function yielding an intrinsic quality factor, Q_i, of 5.6 x 10^5 corresponding to 1 dB/cm background optical propagation loss. b) Microdisk intrinsic quality factor versus wavelength confirming the onset of thulium absorption at longer wavelengths. Inset in b: free spectral ranges (FSRs) of the microdisk modes versus wavelength.

A schematic of the measurement setup used to characterize the lasers is displayed in figure 6.4a. We coupled polarized pump light from a tunable 1520–1640 nm laser set at ~1610 nm and a high-power L-band erbium-ytterbium-co-doped fiber amplifier (L-band EYDFA) to the chip via a fiber polarization controller, a 1600/1900 nm fiber wavelength division multiplexor (WDM), and a 2-µm spot size at 1550-nm wavelength tapered optical fiber mounted on an *xyz* alignment stage. The microdisk laser output was also coupled from the chip using a tapered fiber mounted on an *xyz* stage, filtered from the pump light with a 1600/1900 nm WDM, and coupled to an optical spectrum analyzer (OSA) with a resolution of 0.1 nm to observe the output spectrum. The transmitted pump light was also measured using an optical power meter. During measurements the polarization paddles and *xyz* stages were adjusted to select TE polarization and maximize the off-resonance transmitted pump/signal intensity. Figure 6.4b and 6.4c show the image of the experimental setup and microscopic image of microdisk resonator.

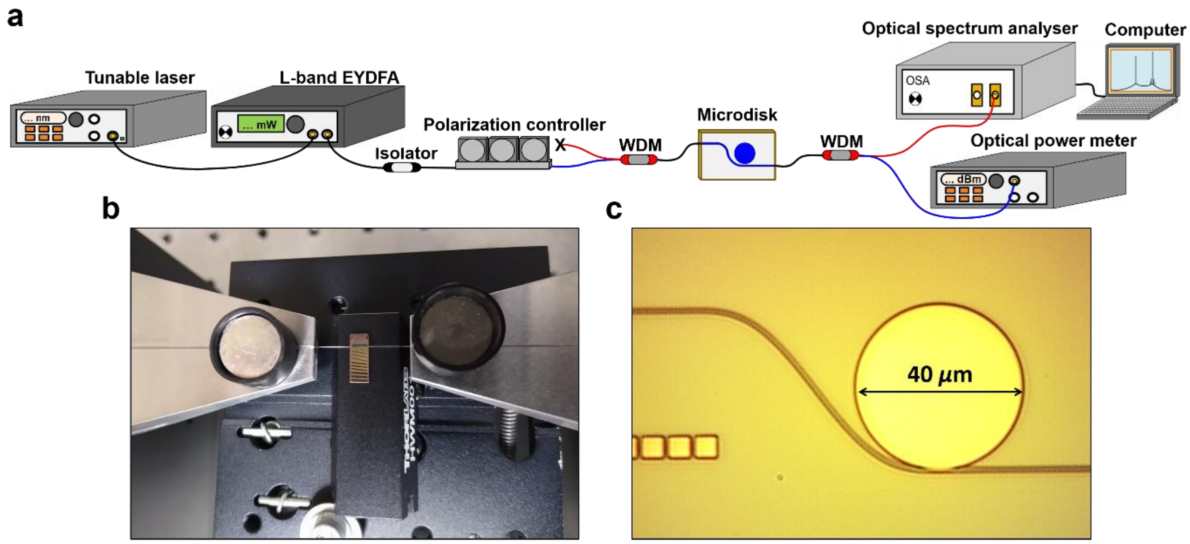

FIGURE 6.4: Transmission and loss measurements: a) Experimental setup used for measuring the on-chip hybrid TeO_2:Tm^{3+}-coated silicon microdisk lasers. b) Photograph of the coupling setup during measure. c) Microscopic image of the hybrid microdisk laser structure.

We describe the TeO_2:Tm^{3+}-Si hybrid microdisk laser results in figure 6.5. We resonantly pumped the TeO_2:Tm^{3+}-coated Si microdisk resonators to investigate their lasing potential, with up to 32.4 mW power launched into the bus waveguide. Lasing was observed for a disk-bus gap of 0.6 µm and the highest slope efficiency and laser output power were observed for pumping at the fundamental TE mode around 1610 nm. The laser output is bidirectional, and we observe similar output power at the pump input side of the chip. As shown in figure 6.5a, we observe a single-mode silicon microdisk laser output spectrum with up to 580 µW single-sided on-chip power and 1.16 mW double-sided output power. The inset shows the pump transmission and laser output spectrum measured at the chip output. A single laser line at 1906 nm is evident with a side-mode suppression of > 30 dB. We observe the laser output signal to be highly stable at room temperature without thermal control of the substrate or any adjustment of the pump wavelength required, even though the device is pumped on a narrow resonance. This is a result of silicon’s relatively strong thermo-optic effect which provides a natural closed-loop system for our microdisk laser when pumped on the blue-side of resonance. Stable operation was observed for at least 9 hours under 29 mW of pumping, with no external thermal stabilization of the laser chip. As shown in figure 6.5b, we observed lasing at a threshold pump power of 16 mW launched into the bus waveguide and 2.5 mW coupled into the microdisk resonator. The single-sided laser slope efficiency versus launched and microdisk-coupled pump power is 4.2 % and 30 %, respectively, which yields a bidirectional slope efficiency with respect to absorbed pump power of up to 60%.

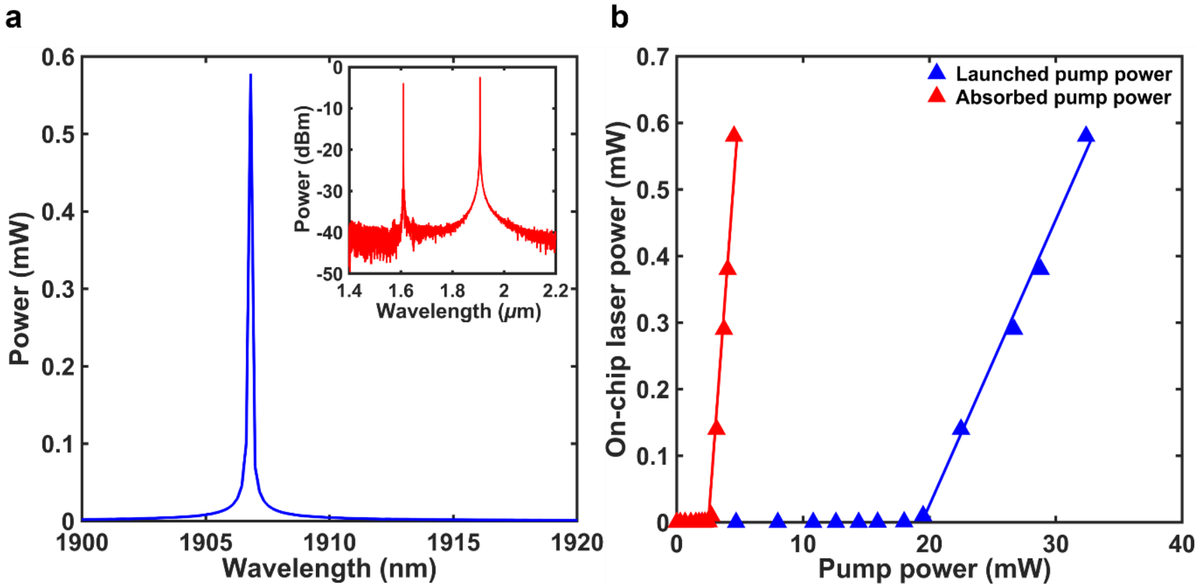

FIGURE 6.5: Hybrid thulium-silicon microdisk laser results: a) Single-mode laser emission spectrum at 1906 nm of a $TeO_2:Tm^{3+}$-coated Si microdisk resonator under 1610-nm pumping at a microdisk-waveguide gap of 0.6 μm obtained with 32.4 mW on-chip pump power. Inset in b: laser emission spectrum with a side-mode suppression of > 30 dB. b) Laser output curve showing a single-sided on-chip output power of up to 580 μW, slope efficiencies of 4.2% and 30% versus on-chip launched and absorbed 1610 nm pump power, and threshold pump powers of 16 mW in the bus waveguide and 2.5 mW in the microdisk resonator.

6.4 Discussion

With this result, we have demonstrated a straightforward and monolithic approach to gain and lasing in silicon using a hybrid rare-earth silicon structure. Compared to prior work on hybrid rare-earth silicon amplifiers and lasers [27,28], our entire structure is integrated on-chip with light emission in a silicon photonic waveguide and the fabrication methods, including low-temperature deposition of the tellurite gain medium, are fully compatible with a silicon photonics foundry process. Furthermore, compared to recent rare-earth lasers on silicon photonics platforms based on silicon nitride cavities [15,41], our cavity design is significantly less complex, has more than an order of magnitude smaller footprint in terms of area, and is directly implemented in the silicon layer. The ultra-compact microdisk cavity design allows for straightforward and large-scale integration of hybrid rare-earth lasers within silicon photonic circuits, where potentially one fixed-wavelength pump source could power multiple lasers for applications such as wavelength division multiplexed systems or parallel sensing. In such a scheme, many on-chip lasers can be effectively powered in a serial or parallel manner by partially coupling the pump light to multiple devices on a single bus or using integrated power splitters, respectively, and efficiently tuning each laser onto resonance. The performance of the lasers can be enhanced by engineering the pump and signal coupling to achieve critical coupling at the pump wavelength [46], increasing the cavity Q to reduce the threshold [47], and using feedback into the cavity to force uni-directional emission [48,49]. Besides the microdisk cavity design shown here, integration of rare-earth gain with silicon waveguides opens the possibility to develop versatile integrated cavity structures and new cost-effective chip-scale light sources such as tunable lasers [50] which leverage the monolithic and wideband rare-earth gain and silicon’s active optoelectronic functionalities and highly efficient thermo-optic tuning. By showing optical gain and lasing in a hybrid rare-earth silicon structure we also build on recent advances on monolithic rare-earth-doped amplifiers on silicon platforms [25,51] and provide incentive for developing new types of ultra-compact optical amplifiers, which are another important missing element in commercial silicon photonics process design kits. In addition to thulium devices operating around 2 µm, these results provide a guide for exploring other prospective dopants and host materials [38] for rare-earth silicon hybrid lasers and amplifiers which operate in near- to mid-infrared wavelength bands of interest for silicon microsystems.

6.5 Low-Threshold Thulium-Silicon Microdisk Lasers

Following the initial results on $TeO_2:Tm^{3+}$-Si lasers, higher power lasers at lower threshold was investigated to improve the lasers performances by adjusting the waveguide cross-section including a thicker $TeO_2:Tm^{3+}$ layer for greater mode overlap with the active area, pump wavelength, and Tm^{3+} ion concentration. The disks were fabricated with radii of 20 and 30 µm and 60º pulley-coupled single-mode strip Si waveguides coated with a 385-nm-thick $TeO_2:Tm^{3+}$ layer as the active area. Compared to the point-coupled design investigated in [52,53], the pulley-coupled design enables more versatility in adjusting the pump input and laser output coupling strength. The prism coupling method was used to determine a $TeO_2:Tm^{3+}$ thin-film propagation loss of ≤ 0.3 dB/cm at 1510 nm.

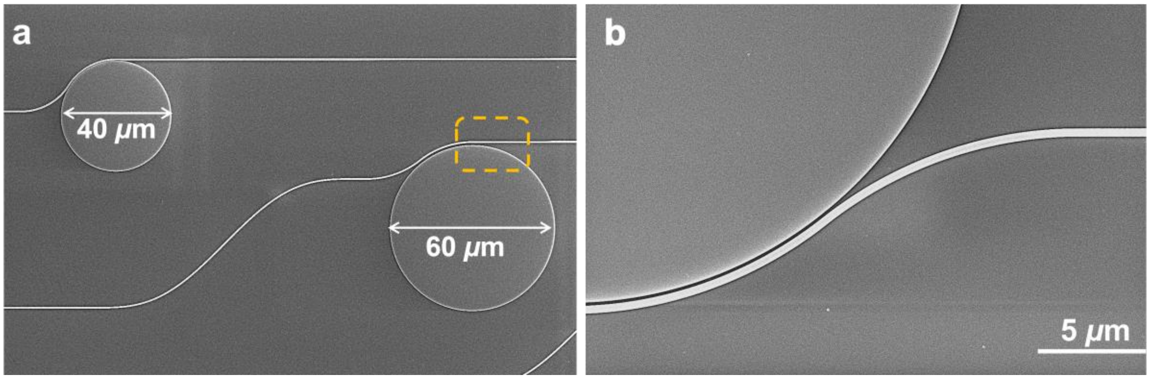

FIGURE 6.6: a) Top-view b) Zoomed top-view SEM image of a $TeO_2:Tm^{3+}$-coated Si microdisk laser with a radius of 20 μm radius with the bus waveguide pulley coupled around the resonator.

The top-view and the zoomed top-view scanning electron microscope (SEM) image of the hybrid lasers are displayed in figure 6.6a, and 6.6b for better visualization, respectively. The intrinsic Q factors were measured as $Q_{int} = 1.0 \times 10^6$ at 1530.43 nm and 1.0×10^6 at 1526.11 nm for 20 μm and 30 μm radii of microdisk, respectively, corresponding to the estimated propagation losses of 0.60 dB/cm and 0.54 dB/cm, respectively [54]. To improve the threshold and output power of the lasers, silicon microdisk structures were pumped with varying Tm concentrations ranging from 2.5×10^{20} cm^{-3} to 4.9×10^{20} cm^{-3}.

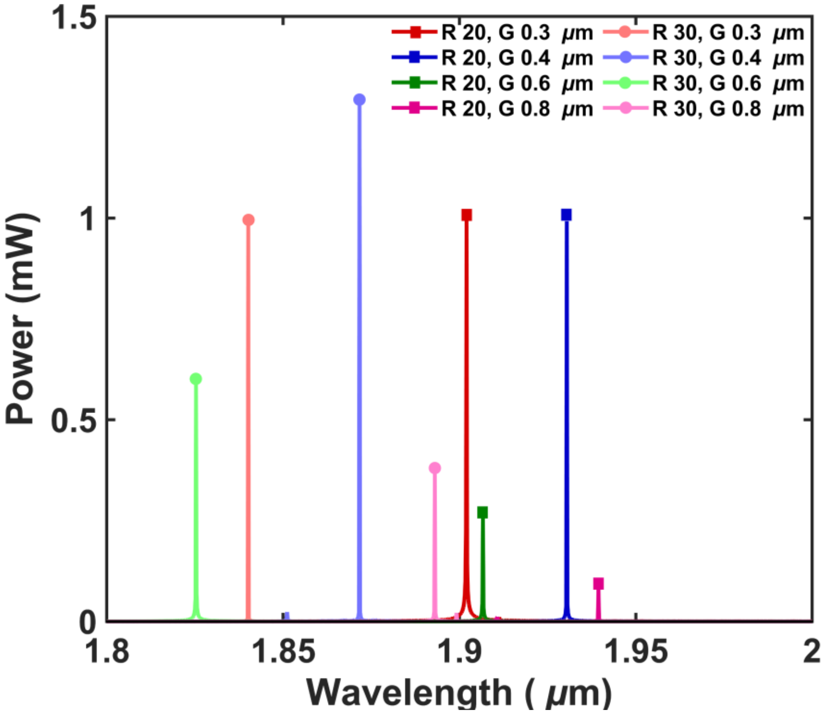

FIGURE 6.7: Laser emission spectra of $TeO_2:Tm^{3+}$-Si microdisk resonators under 1620-nm pumping and for microdisk-waveguide gaps ranging from 0.3 μm to 0.8 μm for 20 μm and 30 μm microdisk radii. The laser emission shifts from ~1825 to 1939 nm by changing the gap size.

The laser spectra were obtained under 1620-nm pumping up to 20 mW power launched into the bus waveguide and at different gaps of 0.3, 0.4, 0.6, and 0.8 μm shown in figure

6.7. Lasing is observed at wavelengths spanning from 1825 to 1939 nm in different micrdisk resonators with 20 μm and 30 μm radii. The highest laser output power, lowest threshold, and highest slope efficiency were observed for a disk-bus gap of 0.4 μm and pumping at the fundamental TE mode around 1620 nm with the thulium concentration of 4.3×10^{20} cm^{-3}. Single-mode lasing was observed at 1930 nm with up to 2 mW double-sided on-chip power in a 20 μm radius microdisk resonator with a gap of 0.4 μm and multi-mode lasing was observed at 1872 nm with up to 2.6 mW double-sided on-chip power in a 30 μm radius microdisk resonator with a gap of 0.4 μm.

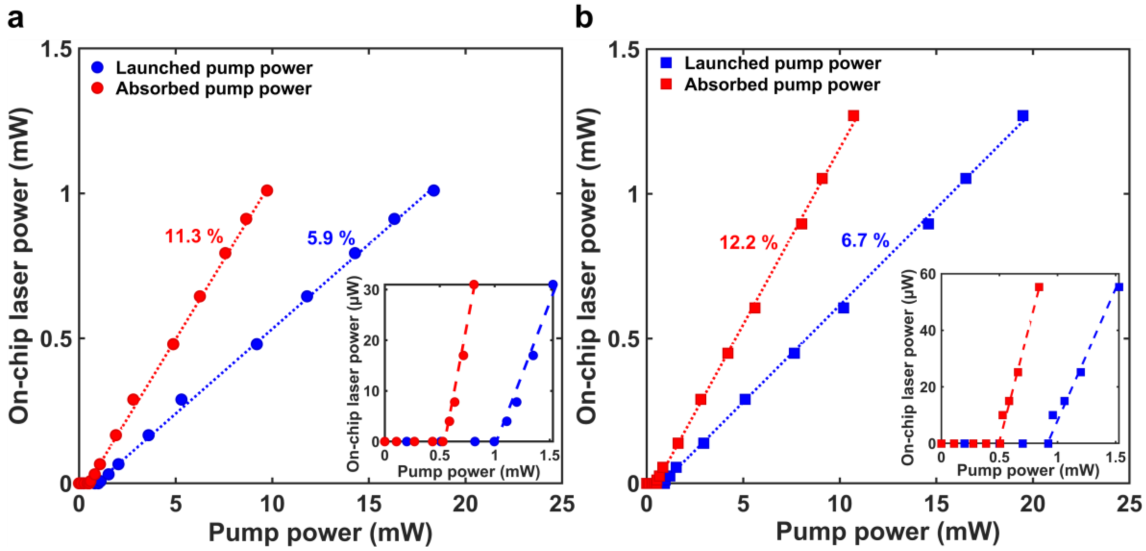

FIGURE 6.8: a) Single-sided on-chip output power of up to 1.0 mW with a slope efficiency of 5.9 % versus on-chip launched power pumped at 1620 nm and a threshold pump power of 997 μW in the bus waveguide in a 20-μm radius microdisk resonator. b) Single-sided on-chip output power of up to 1.3 mW with a slope efficiency of 6.7 % versus on-chip launched power pumped at 1620 nm and a threshold pump power of 918 μW in the bus waveguide in a 30-μm radius microdisk resonator.

Low threshold lasing is observed and the laser output signal to be highly stable at room temperature without thermal control of the substrate or any adjustment of the pump wavelength required, even though the device is pumped on a narrow resonance. As shown in figure 6.8a, a threshold pump power of 918 μW launched into the bus waveguide and 505 μW coupled into the microdisk resonator with 30 μm radius was measured. The single-sided laser slope efficiency versus launched and absorbed pump power is 6.7 and 12.2 %, respectively. The single-sided laser slope efficiency versus launched and absorbed pump power is 5.9% and 11.3%, respectively, with the threshold pump power of 997 μW and 531 μW in the bus waveguide and microdisk resonators, respectively, in 20 μm radius of the microdisk resonator as shown in figure 6.8b.

The performance of the lasers was enhanced by engineering the pump and signal coupling wavelength, thulium concentration, and loss mechanism. These laser results on different chips show the consistent performance and high quality of the TeO_2:Tm^{3+}-Si hybrid microdisk lasers and provide a guide for future work on optimization of integrated hybrid silicon lasers. The results presented in this work will enable us for having highly efficient thermo-optic laser control via implementing metal heaters operating in a wide range of wavelengths with further work on other rare-earth-silicon hybrid lasers and amplifiers.

6.6 Conclusion

We have demonstrated a single-mode hybrid thulium-silicon laser integrated on a chip. The hybrid laser is ultra-compact and fabricated using standard silicon photonic processing methods and cost-effective, low-temperature and wafer-scale post-processing steps enabling large-scale integration, volume production and implementation within advanced silicon photonic microsystems. The laser emits at 1906 nm with a threshold pump power of 16 mW and 2.5 mW with respect to the power coupled into the silicon bus waveguide microdisk, respectively. We observe more than 1 mW bi-directional on-chip output power and a slope efficiency versus absorbed pump power of 60%. Subsequently, low threshold silicon microdisk lasers were fabricated with on-chip output powers up to 2.6 mW with threshold pump powers as low as 505 μW absorbed into the microdisk resonator and emit over a wide range of wavelengths spanning more than 100 nm from 1825 nm to 1939 nm. The low thresholds demonstrate the potential for pumping using compact low-cost diodes and the wide gain and emission range is of interest for applications including on-chip broadband amplifiers and tunable lasers for emerging ~1.8–2.0 µm silicon photonic systems. These new, stable, compact, inexpensive, efficient, room temperature silicon lasers have implications for ultra-compact light sources for silicon-based photonic microsystems in the emerging 2-µm wavelength band. Integrated silicon lasers are in high demand for applications including data communications, quantum information systems, artificial intelligence, nonlinear optical systems, mid-infrared light generation, humidity, gas and bio sensors, detection and ranging, spectroscopy, and advanced metrology.

6.7 Methods

6.7.1 Laser Fabrication

The laser chips were fabricated on an SOI platform using the Advanced Micro Foundry (AMF) silicon photonics fabrication process in Singapore. Silicon strip bus waveguides of 0.45 µm width and microdisks with radii of 20 µm and gaps varying from 0.2–1.6 µm between the outer walls of the silicon disk and bus waveguide, were patterned using deep ultraviolet 193-nm lithography into a 0.22-µm-thick silicon waveguide layer on a 2 µm-thick SiO_2 buried oxide (BOX) layer, without top SiO_2 cladding, allowing for post-process $TeO_2:Tm^{3+}$ thin film deposition. The silicon waveguides were tapered from 0.45- to 0.18-µm width at the edge of the chip and deep trenches were etched into the BOX and silicon handle wafer to allow for low-loss fiber-chip light coupling. The SOI wafer was diced along the deep trenches into chips and the chips were transferred from the foundry. We then deposited a 0.37-µm-thick $TeO_2:Tm^{3+}$ coating layer onto the passive silicon chips at McMaster University using a radio frequency (RF) reactive magnetron co-sputtering process, which allows for fast deposition at room temperature and results in uniformly doped films with low losses. The process is similar to that reported for fabrication of silicon nitride hybrid amplifiers [55,56]. Three-inch metallic tellurium and thulium targets with 99.999 and 99.9% purity, respectively, were sputtered in an argon/oxygen atmosphere at ambient temperature. We set the Te and Tm RF sputtering powers to 120 W and 85 W, respectively, and the Ar and O_2 flow rates to 12 sccm and 9.4 sccm, respectively, at 20°C. The deposition rate for the $TeO_2:Tm^{3+}$ film was 13 nm/min and its refractive index was 2.04 at 638 nm and 1.99 at 1550 nm wavelengths measured by spectroscopic ellipsometry. $TeO_2:Tm^{3+}$ thin film propagation losses of ≤ 0.5 dB/cm at 1510 nm were determined using the prism coupling method and a separate film prepared on a thermally oxidized silicon substrate in the same deposition run. We measured a thulium ion dopant concentration of 4.0×10^{20} cm^{-3} using Rutherford backscattering spectrometry (RBS). The $TeO_2:Tm^{3+}$ layer thickness of 0.37 µm was chosen as a suitable top-cladding thickness to confine the mode within the hybrid resonator structure and for sufficient mode overlap with the gain medium, while the thulium ion dopant concentration of 4.0 × 10^{20} cm^{-3} was selected to be high enough to achieve greater gain than microdisk roundtrip losses, including propagation and disk-waveguide coupling losses. It is important to note that although the chips were unclad and passive-only in this study, the laser design allows for similar processing steps to be carried out on silicon photonic chips with active device layers, including metals and dopants, by etching a window into the top SiO_2 cladding (a standard processing step available within the silicon photonics foundry) and due to the low temperature $TeO_2:Tm^{3+}$ deposition.

6.7.2 Optical Mode, Laser Loss and Gain Calculations

We calculated the electric field profiles, intensity overlap factors, effective indices and effective areas of the hybrid $TeO_2:Tm^{3+}$-silicon waveguide and microdisk modes and radiation losses of the microdisk using a finite-element method modesolver (RSoft FemSIM) and the cross-sectional structure shown in figure 6.1b. The microdisk cavity Q factor was converted to an equivalent propagation loss using the assumptions and method outlined in reference [57] and a calculated group index of 3.53 at the pump wavelength. We calculated the maximum Tm^{3+} gain achievable in the resonator, g_{Tm} (in dB/cm), using the following equation:

$$g_{\mathrm{Tm}} = 10\log_{10}\mathrm{e} \times \Gamma \times \sigma_{21} \times \mathrm{N}_{\mathrm{Tm}} \tag{6.1}$$

where Γ is the calculated active medium confinement factor of the microdisk mode, σ_{21} is the Tm^{3+} ion emission cross section on the $^3F_4$–$^3H_6$ transition and is estimated to be 5.8×10^{-21} cm^2 at the laser wavelength for tellurite glass from reference [58], N_{Tm} is the Tm^{3+} ion concentration and we assume full Tm^{3+} population inversion to give an upper limit to the gain. The confinement factor (Γ) is calculated in terms of the electric field energy density factor (γ_A), group index (n_g) and active material index (n_A) using the following equation [59]:

$$\Gamma = \frac{n_g}{n_A}\gamma_A \tag{6.2}$$

We determine a confinement factor of 0.16 based on an energy density factor of 0.09, group index of 3.45 and TeO_2:Tm^{3+} refractive index of 1.94 at 1906 nm. This corresponds to a maximum Tm^{3+} gain of 1.6 dB/cm for the microdisk laser. We note that by using similar calculations for the hybrid bus waveguide structure, the single-sided thulium-related pump absorption and laser signal enhancement in the waveguide were determined to be < 1 dB and have minimal impact on the pump threshold power and laser output power, respectively.

6.7.3 Laser Measurements

We characterized the passive and active properties of the silicon microdisk laser using the experimental setup shown in figure 6.4. The fiber-chip coupling loss was determined to be 7.5 dB and 7.1 dB at 1610 and 1906 nm, respectively, by insertion loss measurements (with a 2 µm tunable laser coupled to the input WDM for the 1906 nm measurement), and is influenced by mode mismatch, Fresnel reflections and scattering due to the conformal $TeO_2:Tm^{3+}$ coating on the facet. We determined the launched pump power by measuring the incident power from the input fiber using an integrating sphere photodiode power monitor and accounting for fiber-chip coupling loss. The extinction ratio at the pump wavelength is 0.6 dB, which means that 13% of the power in the bus waveguide is absorbed in the microdisk resonator. The on-chip laser output power is considered to be the power measured in the hybrid silicon bus waveguide, accounting for the output WDM insertion loss and fiber-chip coupling loss at the laser wavelength. Transmission measurements were carried out on the same setup without the L-band EYDFA and the OSA replaced with a photodetector to determine the background microdisk propagation loss. We measured the transmission in the wavelength range of 1520 to 1540 nm where we observe negligible thulium absorption loss and the fitted intrinsic Q factor can be assumed to represent the passive propagation loss of the structure. The error in the measured optical power, which includes uncertainties in the fiber-chip coupling efficiency and power meter or OSA accuracy, is within the size of the plotted data points.

6.7.4 Bus Waveguide Gain Measurements

The contribution of gain in the hybrid bus waveguide during laser measurements was investigated in a device with a 1.4-µm disk-waveguide gap where no resonances were observed. We carried out pump-probe measurements on the laser setup by adding a 2-µm tunable laser source coupled to a polarization controller, to select TE polarization, to the input WDM and an additional WDM at the output to filter the residual pump light. We observed signal enhancement at the laser wavelength of up to 1.8 dB in a 3-mm-long

TeO_2:Tm^{3+} silicon waveguide for a launched pump power of 32.4 mW. An upper limit to the background waveguide loss was determined by measuring the Q factor at 1523.1 nm in a 20-µm-radius microring resonator with same cross-sectional dimensions as the bus waveguide on the same chip. We obtained a Q factor of 5.5 x 10^5 corresponsing to a propagation loss of 1.0 dB/cm. Based on insertion loss measurements, we determined an additional Tm-related absorption of 1.1 dB at 1906 nm, giving a total loss of 1.4 dB in the unpumped waveguide. The internal net gain is given by the signal enhancement minus the background waveguide propagation loss and Tm-related absorption. Therefore, we determine an internal net gain of 0.4 dB. A schematic of the experimental setup used to measure the gain in the hybrid thulium-silicon waveguide is displayed in figure 6.9a. Figure 6.9b shows the internal net gain versus launched pump power at the laser wavelength. The propagation loss from 1870 to 2000 nm with the pump off corresponding to the same waveguide is displayed in the inset of figure 6.9b.

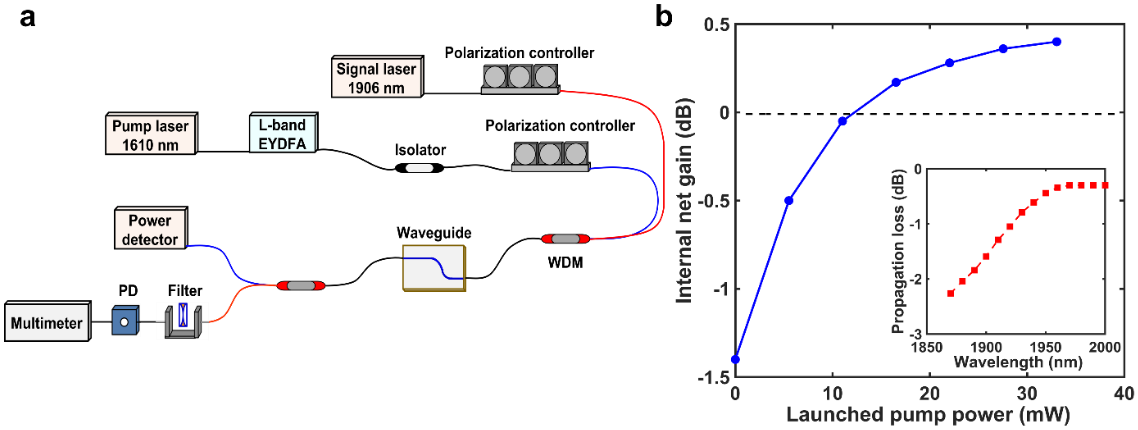

FIGURE 6.9: Gain measurements: a) Experimental setup for measuring the gain in the hybrid thulium-silicon bus waveguide (wavelength division multiplexer (WDM); photodetector (PD)). b) Signal enhancement versus launched pump power measured in a 0.3-cm long Tm-doped waveguide at 1610 nm pump wavelength. The inset shows the propagation loss of the waveguide from 1870 to 2000 nm with the pump off.

Bibliography

[1] A. Rickman, “The Commercialization of silicon photonics,” *Nat. Photonics* **8**, 579–582 (2014).

[2] X. Chen, M. M. Milosevic, S. Stankovic´, S. Reynolds, T. Domínguez Bucio, K. Li, D. J. Thomson, F. Gardes, and G. T. Reed, “The emergence of silicon photonics as a flexible technology platform,” *Proc. IEEE* **106**, 2101–2116 (2018).

[3] A. E. Lim, J. Song, Q. Fang, C. Li, X. Tu, N. Duan, K. K. Chen, R. P. Tern, T. Liow, “Review of silicon photonics foundry efforts,” *IEEE J. Sel. Top. Quantum Electron.* **20**, 8300112 (2014).

[4] V. Stojanović, R. J. Ram, M. Popović, S. Lin, S. Moazeni, M. Wade, C. Sun, L. Alloatti, A. Atabaki, F. Pavanello, N. Mehta, and P. Bhargava, “Monolithic silicon-photonic platforms in state-of-the-art CMOS SOI processes,” [invited]. *Opt. Express* **26**, 13106–13121 (2018).

[5] A. Rahim, J. Goyvaerts, B. Szelag, J.-M. Fedeli, P. Absil, T. Aalto, M. Harjanne, C. Littlejohns, G. Reed, G. Winzer, S. Lischke, L. Zimmermann, D. Knoll, D. Geuzebroek, A. Leinse, M. Geiselmann, M. Zervas, H. Jans, A. Stassen, C. Dominguez, P. Munoz, D. Domenech, A. Lena Giesecke, M. C. Lemme, and R. Baets, “Open-access silicon photonics platforms in Europe,” *IEEE J. Sel. Top. Quantum Electron.* **25**, 8200818 (2019).

[6] D. Liang, and J. E. Bowers, “Recent progress in lasers on silicon,” *Nat. Photonics* **4**, 511–517 (2010).

[7] Z. Fang, Q. Y. Chen, and C. Z. Zhao, “A review of recent progress in lasers on silicon,” *Opt. Laser Technol.* **46**, 103–110 (2013).

[8] Z. Zhou, B. Yin, and J. Michel, “On-chip light sources for silicon photonics,” *Light Sci. Appl.* **4**, e358 (2015).

[9] H. Rong, S. Xu, Y. Kuo, V. Sih, O. Cohen, O. Raday, and M. Paniccia, “Low-threshold continuous-wave Raman silicon laser,” *Nat. Photonics* **1**, 232–237 (2007).

[10] M. J. R. Heck, J. F. Bauters, M. L. Davenport, J. K. Doylend, S. Jain, G. Kurczveil, S. Srinivasan′, Y. Tang, and J. E. Bowers, “Hybrid silicon photonic integrated circuit technology,” *IEEE J. Sel. Top. Quantum Electron.* **19**, 6100117 (2013).

[11] R. E. Camacho-Aguilera, Y. Cai, N. Patel, J. T. Bessette, M. Romagnoli, L. C. Kimerling, and J. Michel, “An electrically pumped germanium laser,” *Opt. Express* **20**, 11316–11320 (2012).

[12] A. Elbaz, D. Buca, N. Driesch, K. Pantzas, G. Patriarche, N. Zerounian, E. Herth, X. Checoury, S. Sauvage, I. Sagnes, A. Foti, R. Ossikovski, J.-M. Hartmann, F. Boeuf, Z. Ikonic, P. Boucaud, D. Grützmacher, and M. El Kurdi, “Ultra-low-threshold continuous-wave and pulsed lasing in tensile-strained GeSn alloys,” *Nat. Photonics* **14**, 375–382 (2020).

[13] A. L. Gaeta, M. Lipson, and T. J. Kippenberg, “Photonic-chip-based frequency combs,” *Nat. Photonics* **13**, 158–169 (2019).

[14] D. Korn, M. Lauermann, S. Koeber, P. Appel, L. Alloatti, R. Palmer, P. Dumon, W. Freude, J. Leuthold, and C. Koos, “Lasing in silicon-organic hybrid waveguides,” *Nat. Commun.* **7,** 10864 (2016).

[15] N. Li, M. Xin, Z. Su, E. Salih Magden, N. Singh, J. Notaros, E. Timurdogan, P. Purnawirman, J. D. B. Bradley, and M. R. Watts, "A silicon photonic data link with a monolithic erbium-doped laser," *Sci. Rep*. **10**, 1114 (2020).

[16] Z. Wang, A. Abbasi, U. Dave, A. De Groote, S. Kumari, B. Kunert, C. Merckling, M. Pantouvaki, Y. Shi, B. Tian, K. Van Gasse, J. Verbist, R. Wang, W. Xie, J. Zhang, Y. Zhu, J. Bauwelinck, X. Yin, Z. Hens, J. Van Campenhout, B. Kuyken, R. Baets, G. Morthier, D. Van Thourhout, G. Roelkens, "Novel light source integration approaches for silicon photonics," *Laser Photonics Rev.* **11**, 1700063 (2017).

[17] M. Tang, J.-S. Park, Z. Wang, S. Chen, P. Jurczak, A. Seeds, H. Liu, "Integration of III-V lasers on Si for Si photonics," *Prog. Quantum Electron.* **66**, 1-18 (2019).

[18] B. Stern, X. Ji, Y. Okawachi, A. L. Gaeta & Michal Lipson, "Battery-operated integrated frequency comb generator," *Nature* **562**, 401–405 (2018).

[19] M. N. Sysak, D. Liang, R. Jones, G. Kurczveil, M. Piels, M. Fiorentino, R. G. Beausoleil, and J. E. Bowers, "Hybrid silicon laser technology: a thermal perspective," *IEEE J. Sel. Top. Quantum Electron.* **17**, 1490–1498 (2011).

[20] J. D. B. Bradley and M. Pollnau, "Erbium-doped integrated waveguide amplifiers and lasers," *Laser Photonics Rev.* **5**, 368 (2011).

[21] C. Grivas, "Optically pumped planar waveguide lasers: Part II: Gain media, laser systems, and applications," *Prog. Quantum Electron.* **45–46**, 3–160 (2016).

[22] W. A. P. M. Hendriks, L. Chang, C. I. van Emmerik, J. Mu, M. de Goede, M. Dijkstra, S. M. Garcia-Blanco, "Rare-earth ion doped Al_2O_3 for active integrated photonics," *Adv. Phys.: X* **6**, 1833753 (2021).

[23] M. Belt, T. Huffman, M. L. Davenport, W. Li, J. S. Barton, and D. J. Blumenthal, "Arrayed narrow linewidth erbium-doped waveguide-distributed feedback lasers on an ultra-low-loss silicon-nitride platform," *Opt. Lett.* **38**, 4825–4828 (2013).

[24] N. Li, E. S. Magden, Z. Su, N. Singh, A. Ruocco, M. Xin, M. Byrd, P. T. Callahan, J. D. B. Bradley, C. Baiocco, D. Vermeulen, M. R. Watts, "Broadband 2-µm emission on silicon chips: monolithically integrated Holmium lasers," *Opt. Express* ***26***, 2220 (2018).

[25] J. Rönn, W. Zhang, A. Autere, X. Leroux, L. Pakarinen, C. Alonso-Ramos, A. Säynätjoki, H. Lipsanen, L. Vivien, E. Cassan, and Z. Sun, "Ultra-high on-chip optical gain in erbium hybrid slot waveguides," *Nat. Commun.* **10**, 432 (2019).

[26] M. Xin, N. Li, N. Singh, A. Ruocco, Z. Su, E. S. Magden, J. Notaros, D. Vermeulen, E. P. Ippen, M. R. Watts, F. X. Kärtner, "Optical frequency synthesizer with an integrated erbium tunable laser," *Light Sci. Appl.* ***8***, 122 (2019).

[27] L. Agazzi, J. D. B. Bradley, M. Dijkstra, F. Ay, G. Roelkens, R. Baets, K. Wörhoff, M. Pollnau, "Monolithic integration of erbium-doped amplifiers with silicon-on-insulator waveguides," *Opt. Express* ***18***, 27703 (2010).

[28] M. Borselli, "High-Q microresonators as lasing elements for silicon photonics," *PhD Thesis,* California Institute of Technology, Pasadena, May (2006).

[29] J. Notaros, N. Li, C. V. Poulton, Z. Su, M. J. Byrd, E. S. Magden, E. Timurdogan, C. Baiocco, N. M. Fahrenkopf, "CMOS-compatible optical phased array powered by a monolithically-integrated erbium laser," *J. Lightwave Technol.* **37**, 5982 (2019).

[30] G. Roelkens, U. D. Dave, A. Gassenq, N. Hattasan, C. Hu, B. Kuyken, F. Leo, A. Malik, M. Muneeb, E. Ryckeboer, D. Sanchez, S. Uvin, R. Wang, Z. Hens, R. Baets, Y.

Shimura, F. Gencarelli, B. Vincent, R. Loo, J. Van Campenhout, L. Cerutti, J.-B. Rodriguez, E. Tourni´e, X. Chen, M. Nedeljkovic, G. Mashanovich, L. Shen, N. Healy, A. C. Peacock, X. Liu, R. Osgood, "Silicon-based photonic integration beyond the telecommunication wavelength range," *IEEE J. Sel. Top. Quantum Electron.* **20**, 8201511 (2014).

[31] R. Soref, "Enabling 2 μm communications," *Nat. Photonics* **9**, 358–359 (2015).

[32] F. C. Garcia Gunning, N. Kavanagh, E. Russell, R. Sheehan, J. O'Callaghan, and B. Corbett, "Key enabling technologies for optical communications at 2000 nm," *Appl. Opt.* **57**, E64–E70 (2018).

[33] D. J. Richardson, "Filling the light pipe," *Science* **330**, 327–328 (2010).

[34] J. J. Ackert, D. J. Thomson, L. Shen, A. C. Peacock, P. E. Jessop, G. T. Reed, G. Z. Mashanovich, and A. P. Knights, "High-speed detection at two micrometres with monolithic silicon photodiodes," *Nat. Photonics* **9**, 393–396 (2015).

[35] W. Cao, D. Hagan, D. J. Thomson, M. Nedeljkovic, C. G. Littlejohns, A. Knights, S.-U. Alam, J. Wang, F. Gardes, W. Zhang, S. Liu, K. Li, M. Said Rouifed, G. Xin, W. Wang, H. Wang, G. T. Reed, and G. Z. Mashanovich, "High-speed silicon modulators for the 2 µm wavelength band," *Optica* **5**, 1055–1062 (2018).

[36] J. Li, Y. Liu, Y. Meng, K. Xu, J. Du, F. Wang, Z. He, and Q. Song, "2-μm wavelength grating coupler, bent waveguide, and tunable microring on silicon photonic MPW," *IEEE Photonics Technol. Lett.* **30**, 471–474 (2018).

[37] M. Lamy, C. Finot, P. Colman, J. Fatome, G. Millot, G. Roelkens, B. Kuyken, K. Hammani, "Silicon waveguides for high-speed optical transmissions and parametric conversion around 2 μm," *IEEE Photonics Technol. Lett.* **31**, 165–168 (2019).

[38] S. D. Jackson, "Towards high-power mid-infrared emission from a fibre laser," *Nat. Photonics* **6**, 423 (2012).

[39] S. J. Madden, and K. T. Vu, "Very low loss reactively ion etched Tellurium Dioxide planar rib waveguides for linear and non-linear optics," *Opt. Express* **17**, 17645–17651 (2009).

[40] K. Van Dalfsen, S. Aravazhi, C. Grivas, S. M. García-Blanco, and M. Pollnau, "Thulium channel waveguide laser with 1.6 W of output power and ~80% slope efficiency," *Opt. Lett.* **39**, 4380–4383 (2014).

[41] Z. Su, N. Li, E. Salih Magden, M. Byrd, Purnawirman, T. N. Adam, G. Leake, D. Coolbaugh, J. D. B. Bradley, and M. R. Watts, "Ultra-compact and low-threshold thulium microcavity laser monolithically integrated on silicon," *Opt. Lett.* **41**, 5708–5711 (2016).

[42] N. Li, P. Purnawirman, Z. Su, E. Salih Magden, P. T Callahan, K. Shtyrkova, M. Xin, A. Ruocco, C. Baiocco, E. P. Ippen, F. X Kärtner, J. D. B. Bradley, D. Vermeulen, M. R. Watts, "High-power thulium lasers on a silicon photonics platform," *Opt. Lett.* **42**, 1181–1184 (2017).

[43] A. S. K. Tong, C. J. Mitchell, A. Aghajani, N. Sessions, G. Senthil Murugan, J. I. Mackenzie, and J. S. Wilkinson, "Spectroscopy of thulium-doped tantalum pentoxide waveguides on silicon," *Opt. Mater. Express* **10**, 2201–2211 (2020).

[44] Q. Lin, J. Zhang, G. Piredda, R. W. Boyd, P. M. Fauchet, G. P. Agrawal, "Dispersion of silicon nonlinearities in the near infrared region," *Appl. Phys. Lett.* **91**, 021111 (2007).

[45] D. E. Hagan, and A. P. Knights, "Mechanisms for optical loss in SOI waveguides for mid-infrared wavelengths around 2 μm," *J. Opt.* **19**, 025801 (2016).

[46] E. S. Hosseini, S. Yegnanarayanan, A. H. Atabaki, M. Soltani, and A. Adibi, "Systematic design and fabrication of high-Q single-mode pulley-coupled planar silicon nitride microdisk resonators at visible wavelengths," *Opt. Express* **18**, 2127–2136 (2010).

[47] Y. Zhang, X. Hu, D. Chen, L. Wang, M. Li, P. Feng, X. Xiao, and S. Yu, "Design and demonstration of ultra-high-Q silicon microring resonator based on a multi-mode ridge waveguide," *Opt. Lett.* **43**, 1586-1589 (2018).

[48] D. Liang, S. Srinivasan, D. Fattal, M. Fiorentino, Z. Huang, D. Spencer, J. Bowers, and R. Beausoleil, "Teardrop reflector-assisted unidirectional hybrid silicon microring lasers,," *IEEE Photonics Technol. Lett.* **24**, 1988-1990 (2012).

[49] P. Mechet, S. Verstuyft, T. de Vries, T. Spuesens, P. Regreny, D. Van Thourhout, G. Roelkens, and G. Morthier, "Unidirectional III-V microdisk lasers heterogeneously integrated on SOI," *Opt. Express* **21**, 19339-19352 (2013).

[50] N. Li, E. Timurdogan, C. V. Poulton, M. Byrd, E. S. Magden, Z. Su, Purnawirman, G. Leake, D. D. Coolbaugh, D. Vermeulen, M. R. Watts, "C-band swept wavelength erbium-doped fiber laser with a high-Q tunable interior-ridge silicon microring cavity," *Opt. Express* ***24***, 22741 (2016).

[51] P. F. Jarschel, M. C. M. M. Souza, R. B. Merlo, and N. C. Frateschi, "Loss compensation in microring-based Si photonics devices via Er^{3+} doped claddings," *IEEE Photonics J.* **10**, 4501112 (2018).

[52] K. Miarabbas Kiani, H. C. Frankis, C. M. Naraine, D. B. Bonneville, A. P. Knights, and J. D. B. Bradley, "Lasing in a hybrid rare-earth silicon microdisk," *Laser Photon. Rev.* **16**, 210034 (2022).

[53] K. Miarabbas Kiani, H. C. Frankis, C. M. Naraine, D. B. Bonneville, A. P. Knights, and J. D. B. Bradley, "A Thulium-silicon hybrid microdisk laser," *OSA Advanced Photonics Congress,* JTh3A.2 (2021).

[54] K. Miarabbas Kiani, D. B. Bonneville, A. P. Knights, and J. D. B. Bradley, "High-*Q* TeO_2–Si hybrid microring resonators," *Appl. Sci.* **12**, 1363 (2022).

[55] K. Miarabbas Kiani, H. C. Frankis, H. M. Mbonde, R. Mateman, A. Leinse, A. P. Knights, and J. D. B. Bradley, "Thulium-doped tellurium oxide waveguide amplifier with 7.6 dB net gain on a silicon nitride chip," *Opt. Lett.* **44**, 5788–5791 (2019).

[56] K. Miarabbas Kiani, H. C. Frankis, R. Mateman, A. Leinse, A. P. Knights, and J. D. B. Bradley, "High gain thulium-doped tellurium oxide waveguide amplifier for optical communication in the 2 µm window," *IEEE Photonics North (PN)*, 1-1 (2021).

[57] K. Preston, B. Schmidt, and M. Lipson, "Polysilicon photonic resonators for large-scale 3D integration of optical networks," *Opt. Express* **15**, 17283–17290 (2007).

[58] S. V. Muravyev, E. A. Anashkina, A. V. Andrianov, V. V. Dorofeev, S. E. Motorin, M. Y. Koptev, and A. V. Kim, "Dual-band Tm^{3+}-doped tellurite fiber amplifier and laser at 1.9 µm and 2.3 µm," *Sci. Rep.* **8**, 16164 (2018).

[59] J. T. Robinson, K. Preston, O. Painter, and M. Lipson, "First-principle derivation of gain in high-index-contrast waveguides," *Opt. Express* **16**, 16659-16669 (2008).

Chapter 7

Conclusion

7.1 Summary

The aim of this thesis was to develop low-loss high-quality thulium-doped tellurium oxide ($TeO_2:Tm^{3+}$) thin films as the active medium for photonic structures including efficient amplifiers and lasers compatible with the current state of the art, foundry level, waveguide processing techniques for silicon (Si), and silicon nitride (Si_3N_4) for use in the thulium-doped fiber amplifier (TDFA) wavelength band centered near 2 µm.

An introduction and motivation of this thesis are given in chapter 1. Chapter 2 describes the theory and background of the devices discussed in this thesis. This chapter also serves as a general background chapter, presenting the majority of the theory and knowledge on which much of the thesis is built. Beginning with the basic building block of silicon photonics, principles of light, its behavior in optical waveguides, and properties are discussed on silicon-on-insulator (SOI) and silicon nitride (Si_3N_4) platform. Afterwards, details on the spectroscopy of rare-earth ions and the science behind thulium (Tm^{3+}) amplifier and laser are presented in this chapter.

Reactively co-sputtered $TeO_2:Tm^{3+}$ thin films on Si_3N_4 chips fabricated at the LioniX foundry, yielding conformally coated hybrid waveguide structures, were investigated for active devices. Thulium-doped waveguide amplifiers integrated on a low-loss silicon nitride platform were demonstrated. In the first demonstration, the total net internal gain was measured to be 7.8 dB at 1870 nm in a 6.7-cm-long s-bend waveguide, corresponding to 1.1 dB/cm. Similar devices with varying thulium concentration were characterized and the optimum Tm^{3+} concentration was determined to be 4.2×10^{20} ions/cm^3. A significantly higher optical gain of 3 dB/cm was measured with a net internal gain of 15.0 dB at 1870 nm in a compact 5-cm spiral waveguide with a minimum bend radius of 200 µm and diameter of 1.6 mm. This work represented the first integrated $TeO_2:Tm^{3+}$ amplifier on Si_3N_4 waveguides using a simple, monolithic, reactive co-sputtering deposition processing step which is compatible with wafer-scale silicon nitride photonic circuits.

Thulium-doped tellurium oxide ($TeO_2:Tm^{3+}$) lasers were fabricated on Si_3N_4 waveguides in a similar manner. $TeO_2:Tm^{3+}$ coated Si_3N_4 ring resonators with a thulium-dopant concentration of 4.1×10^{20} ions/cm^3 showed lasing at wavelengths in the range of 1815–1895 nm under 1610 nm resonant pumping at varying waveguide-microring gap sizes with on-chip double-sided output powers up to almost 16 mW. The microlasers exhibit thresholds as low as 18 mW (11 mW) and a single-sided slope efficiency as high as 11%

(17%) with respect to the pump power coupled into the $TeO_2:Tm^{3+}$-coated Si_3N_4 bus waveguide (absorbed pump power).

A tellurium-oxide-clad silicon microring resonator with an internal Q factor of 1.5×10^6, corresponding to a propagation loss of 0.42 dB/cm at wavelengths around 1550 nm was demonstrated on a silicon-on-insulator (SOI) chip which was fabricated through the AMF foundry. TeO_2 coatings on devices were shown to improve the device Q factor and propagation losses in comparison with the propagation loss of 3.4 dB/cm for unclad waveguides and 0.97 dB/cm for waveguides clad with SiO_2 deposited at the foundry, maintaining negligible radiation losses at a bending radius of 30 μm. Then the experimental results were compared with the Payne-Lacey model which verified that the lower propagation loss in the TeO_2-clad devices can be attributed to the reduced core-cladding refractive index contrast.

Optical gain and lasing in an ultra-compact hybrid rare-earth silicon microdisk resonator was demonstrated. The laser is fabricated in a manner that is compatible with the fabrication steps and device dimensions available in standard silicon photonics foundries and the thulium-doped tellurite gain medium is added in a low-temperature single-step sputter deposition, enabling their integration in state-of-the-art silicon PICs. The hybrid laser is pumped at standard telecom wavelengths around 1.6 μm and exhibits stable single-mode emission at 1.9 μm, with an internal slope efficiency of 8.4% and > 1 mW on-chip output power. The laser design, fabrication, and characterization were improved to achieve low threshold hybrid-integrated thulium-doped tellurium oxide silicon microdisk lasers, with >

2 mW double-sided output power, sub-milliwatt thresholds, a bidirectional slope efficiency of up to 13.4% with respect to power launched into the bus waveguide and lasing at wavelengths over a range of > 100 nm. These lasers are compact, robust, and use a straightforward fabrication method directly with silicon, enabling a low-cost, scalable fabrication approach for realizing lasers in silicon photonic PICs.

In combination with the promising optical properties of TeO_2, these results provide significant steps towards the development of compact, monolithic, and high performance passive and active photonic devices on silicon and silicon nitride platforms with an motivation for expanding applications in 2-µm wavelength. Furthermore, the work presented in this thesis suggests that $TeO_2:Tm^{3+}$ integrated lasers and amplifiers designed and fabricated for TDFA-band wavelengths are viable for emerging telecommunications architectures and can be considered to aid in alleviating anticipated future bandwidth limitations. The approaches used in the thesis allow for low-cost and high-volume wafer-scale manufacturing and co-integration of rare-earth amplifiers and light sources with silicon and silicon nitride passive and active devices in standard process flows.

7.2 Suggested Future Work

Several interesting avenues for future work are possible based on the results reported in this thesis, which allow $TeO_2:Tm^{3+}$ as a competitive and useful active medium for integrated optics. To push the device higher in terms of performance, optimized waveguide design including shadow masking and optimized nanotaper designs can be used to increase the coupling efficiency and decreasing fiber-chip coupling loss based on mode profiles and increase the confinement in the active area. The optimized structure design and reliable deposition can allow for the development of many new active and passive devices and applications which build on this work.

Internally, device performance can be improved through careful simulation. 0.2-µm-thick Si_3N_4 strip waveguides were used in laser and amplifier experimental demonstrations, while thinner Si_3N_4 layers can improve waveguide losses due to less sidewall scattering and greater TeO_2 optical confinement. The experimental demonstration of gains >15 dB and laser output power >16 mW across the TDFA wavelength band will be readily achievable by optimizing the thickness of the active area, cross-section, and length. Additionally, there are many details about the properties of TeO_2:Tm^{3+} films including their spectroscopic properties to be explored. Deeper investigations into quenching mechanisms and spectroscopic parameters of TeO_2:Tm^{3+} films will be effective to model and optimize the amplifier and laser performances.

The higher Q factor microring and microdisk resonators in combination with TeO_2:Tm^{3+} films are a promising pathway towards a highly efficient gain and lasing structure in both silicon nitride and silicon platforms. To achieve large pump powers in the resonator with low outcoupling losses, modified microring and microdisk designs with optimized pulley couplers will be effective. Implementation of heaters in TeO_2:Tm^{3+} lasers on both silicon and silicon nitride platforms will allow for demonstrating tunable lasers and integration of light sources with high performance tunable passive, active and nonlinear PICs.

Integration of $TeO_2:Tm^{3+}$ amplifiers and lasers sources on silicon and silicon nitride platforms with other silicon photonic waveguides and active devices provide a high level of active and passive functionality in a monolithically integrated way that is highly promising in the silicon photonics world. The design considerations and results measured throughout this thesis can be more broadly applied to a wide variety of TeO_2 coatings doped and co-doped with other rare earth materials such as Er^{3+}, Yb^{3+}, and Ho^{3+} for a wide variety of passive, active, and nonlinear optical properties and new devices and functionalities in Si and Si_3N_4 PICs.

Appendix

A Kurt J. Lesker PVD Pro 200 deposition system was used to grow tellurium oxide (TeO_2) and thulium doped tellurium oxide (TeO_2:Tm^{3+}) thin films, in the cleanroom of McMaster University's Centre for Emerging Device Technologies (CEDT). The system includes a deposition chamber with a cryogenic-pump, a load-lock with transfer arm, and an instrument control tower. Samples are loaded into the chamber through the load-lock in an upside-down orientation. All depositions discussed in this thesis used radio frequency (RF) power supplies with a 600 W maximum output. Figure A.1a and A.1b show the PVD deposition system in the CEDT and its diagram, respectively.

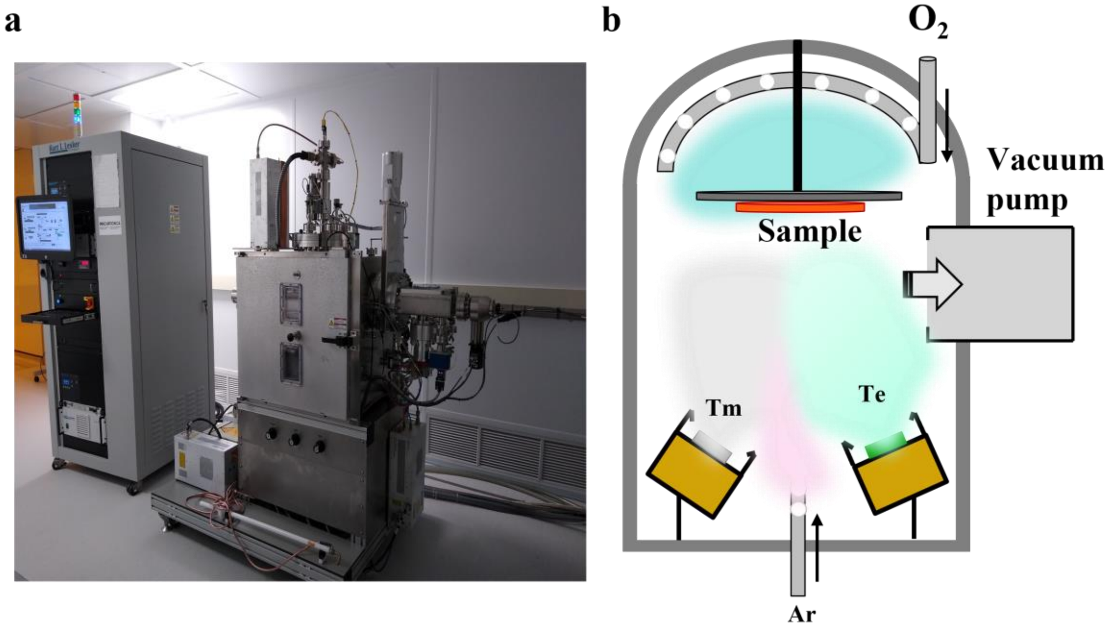

FIGURE A.1: a) Kurt J. Lesker PVD Pro 200 thin film deposition system. b) Diagram of the interior of the sputtering chamber.

The samples were mounted onto a 150-mm diameter substrate holder with a bare silicon test piece, an unpatterned thermally oxidized silicon wafer piece and a blank glass side. After achieving a chamber pressure of 10 mTorr with argon gas, the sputtering guns were turned on at forward powers of 50 W for the tellurium target and 30 W for the thulium target, igniting the plasmas. The oxygen supply valve is opened and inlet at a flow rate of typically 6.6 to 8.0 sccm. The forward powers ramp to the processing setpoint of 145 W for the tellurium target and between 30 to 90 W for the thulium target. After the deposition time is reached the butterfly shield is closed, the RF forward power applied to the sputtering targets is ramped down to the initial value, and the powers are turned off. Then the argon and oxygen gas flow rates decrease to 0 to close the valves. In this work, the depositions for the purpose of TeO_2 and TeO_2:Tm^{3+} thin films characterization were run for 15 to 20 minutes to obtain the desired film thickness of ~0.3 µm.

The fabricated films were characterized to achieve high-quality films with high-deposition rates, high-refractive index, and low optical attenuation. Ellipsometry, prism coupling, and Rutherford backscattering spectrometry (RBS), are the three main characterization techniques that have been used to optimize the TeO_2 and TeO_2:Tm^{3+} thin film deposition recipes. The film's refractive index and thickness was measured by variable angle spectroscopic ellipsometry based on measuring the differences between the complex refraction of transverse electric (TE) and transverse magnetic (TM)- polarized light from a surface. The optical attenuation of the deposited thin film was measured by prism coupling using evanescent beam coupling into the planar waveguide modes. The compositional ratio of thin films fabricated by reactive sputtering was measured by Rutherford backscattering spectrometry (RBS) at the Tandetron Accelerator Laboratory at the University of Western Ontario on bare silicon test pieces.

Co-sputtering of $TeO_2:Tm^{3+}$ thin films was performed by running an optimized low-loss TeO_2 deposition recipe and tuning the thulium ion concentration in the films based on the RF forward power applied to the thulium sputtering target. A set of $TeO_2:Tm^{3+}$ films was deposited by varying the sputtering power applied to a thulium target mounted to a copper backing plate and with a purity of 99.9% in the deposition system as shown in figure A.2a. For this set of films, the tellurium target was sputtered with an RF sputtering power of 145 W with 6.8 sccm of oxygen flow at a passive TeO_2 deposition rate of 20.0 nm/min. The trend follows the expected exponential increase in thulium ion concentration versus RF forward power applied to the thulium target. Based on these results, it becomes apparent that the doping concentration is highly dependent on the power applied to the thulium target thulium if the other conditions are the same. The optimal low loss deposition parameters, including O_2 flow and pressure, were found to vary depending on the target and chamber conditions and typical values are summarized in figure A.2b.

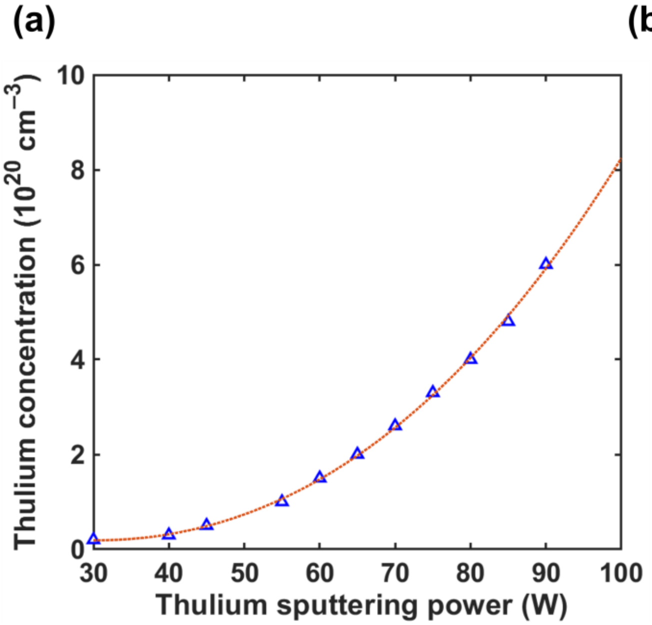

(b)

Deposition Parameters	Value
Temperature (°C)	20
Tellurium RF forward power (W)	145
Thulium RF forward power (W)	30 – 90
Ar flow (sccm)	12
O_2 flow (sccm)	6.6 – 8.0
Chamber pressure (mTorr)	2.6 – 2.8

FIGURE A.2: a) Measured thulium ion concentration of $TeO_2:Tm^{3+}$ thin films versus RF sputtering power applied to the thulium target with the sputtering power of the tellurium target of 145 W and 6.8 sccm of O_2 flow and 12.0 sccm of Ar flow. b) Optimized deposition parameters for RF reactive co-sputtered $TeO_2:Tm^{3+}$ thin films.